Analysis of flow around an RS: X Racing 66 windsurfing fin.

Report for staff in the Department of Applied Physics,
Curtin University of Technology

Written by:
Ketesse Hansen
(Student identification: 13937832)

Supervisors:
Dr Tim Gourlay
Dr Andrew King

Submitted 17th October, 2011
Curtin University of Technology
Perth, Western Australia

Abstract

The behaviour of fluid flowing past a RS:X Racing 66 windsurfing fin at different angles of attack was studied both computationally and experimentally.

This was achieved by creating a three dimensional computational model of the fin, which was both used to produce a physical model for experimental testing, and as the basis for analysis using the fluid analysis program, OpenFOAM.

The experimental analysis of the flow was performed in the Curtin wind tunnel, and the results from these experiments were then compared against the results of the computational fluid analysis.

The effects compared were flow separation, cross flow and tip vortices.

Contents

Abstract 2
Contents 3
List of Figures 5
List of Tables 10
1. Introduction 11
2. Background 12
2.1. Foils 12
2.2.1. NACA foils 12
2.2.2. NACA 6 series 13
2.2.3. RS: X Racing 66 Sailboard Fin 16
2.2.4 Consequences of similarity to NACA 65-009 18
2.3 Computational Fluid Dynamics (CFD) 18
3. Computer generated model 19
3.1. Measuring the Fin 19
3.1.1. Coordinate System 24
3.2. Comparison to NACA foil sections 25
3.3. Leading Edge Radius 28
3.4. Trailing Edge 34
3.5. AutoCAD 35
3.6. STL Files 38
4. Experimental Analysis 39
4.1. Wind Tunnel 40
4.1.1 Dynamic Similarity 40
4.1.2 Required test speed range 41
4.1.3 Boundary layer thickness: wind tunnel flow 42
4.1.4 Boundary layer thickness 43
4.1.5 The expected lift force acting on model inside the wind tunnel 44
4.2. Rapid Prototyper 50
4.3. Tell Tales 51
4.4. Experimental procedure 52
4.4.1 Experimental set up 52
4.4.2 Experimental results 57
4.4.3 Application of experimental results to full-scale model 65
5. Computational Analysis 66
5.1. XFOIL 66
5.1.1 Boundary layer analysis using XFOIL 66
5.1.2 Reynolds and Mach numbers of the wind tunnel flow 67
5.1.3 Boundary layer and pressure distribution 68
5.2. OpenFOAM 72
5.3. Computational procedure 73
5.2.1 Pre-processing 73
5.2.2 Processing 73
5.2.3 Post-processing 74
5.4. Computational results 74
5.3.1 Comparison to experimental results 74
5.3.2 Computational results for racing speed applications 80

5.3.3 Conclusions based on computational results 88
6. Comparison of results to results expected for a NACA 65-009 88
7. Conclusion 89
8. Future Work 90
9. Acknowledgements 90
10. Nomenclature 90
11. References 91
12. Bibliography 94
13. Appendix 95
13.1. Matlab Code 95
13.1.1 mysolvemissing.m 95
13.1.2 interpPoints.m 95

List of Figures

Figure 1: Cambered foil……..12

Figure 2: Typical method of writing NACA 6-series foil……13

Figure 3: NACA 6-series designation for foils with thickness/chord ratios of less than 12%, and the low-drag range omitted……15

Figure 4: RS: X Men's Sailboard……16

Figure 5: Men's RS: X Racing 66 fin (side A)……17

Figure 6: The wind acting on the sail causes the board to move at an angle to the heading, and this is the angle of attack of the flow with respect to the fin. (Not to scale)……17

Figure 7: 5mm intervals along y-displacements alpha, bravo and charlie, fin side A……20

Figure 8: XZ cross section (y-displacement alpha), shown here on axes of unequal scale……21

Figure 9: XZ cross sections of y-displacements alpha and bravo……22

Figure 10: Leading edge of the fin shown using the excel model of the fin viewed in the XY plane, shown here on axes of unequal scale……24

Figure 11: Profile of the fin for each cross section in terms of the percentage of total chord length, shown here on axes of unequal scale……26

Figure 12: Profile of the RS: X Racing 66 windsurfing fin compared against several NACA sections……27

Figure 13: NACA 65-009 foil section profile compared with the profile of the RS: X 66 windsurfing fin (y-displacement: charlie)……28

Figure 14: Leading edge showing measured points a, b and c, which were used to determine the leading edge radius. Also shown are the associated (calculated) points describing the surface of the leading edge radius. The above diagram was produced from the data measured for y-displacement delta……29

Figure 15: Calculation of the leading edge radius……30

Figure 16: Trigonometry used to describe the leading edge radius……30

Figure 17: The adapted and calculated radii and leading edges shown with measured points a, b and c, for cross section foxtrot……33

Figure 18: Trailing edge of the fin……35

Figure 19: Top view of the half teardrop produced from the data points of y-displacement delta modelled in AutoCAD……36

Figure 20: Y-displacements alpha to golf interpolated to have the same number of data points……..36

Figure 21: Top view of y-displacement delta modelled in AutoCAD……37

Figure 22: All cross sections shown in the XY plane, as modelled in AutoCAD……..37

Figure 23: Finished three-dimensional model of the RS: X Racing 66 windsurfing fin, as modelled in AutoCAD, with data points showing……..38

Figure 24: Attached tell tale behaviour. (Cropped from photo #8361)……39

Figure 25: Separated tell tale behaviour. (Cropped from photo #8369)……39

Figure 26: Leading edge of the fin with trapezoid using y-displacements bravo and charlie, and shown here using the excel model of the fin viewed in the XY plane, shown here on axes of unequal scale……46

Figure 27: Lift coefficient for the fin, due to the finite span, shown for angles from 0-20^{o}. It should be noted that the values for the lift coefficient shown above assume the flow has not yet separated……46

Figure 28: 3D printer: ZPrinter 450……50

Figure 29: Proposed tuft attachment locations as a percentage of the total chord for each cross section……..51

Figure 30: Model fin with tell tales attached at 10%, 50%, and 90% of the chord of model y-displacements bravo, charlie, echo and golf. (IMAG0146)……52

Figure 31: Model mounted between two blocks. (Photo #0083)……53

Figure 32: Model mounted with steel plate to prevent recirculation. (Photo #8378)……54

Figure 33: Diagram of a Pitot tube……..54

Figure 34: Manometer used to show the pressure difference measured by the Pitot tube……..55

Figure 35: Fin model oriented at 10^{o} to the flow, with wind speed of 14.6 ms^{-1}. (Photo #8313)……58

Figure 36: Fin model oriented at 12^{o} to the flow, with wind speed of 14.6 ms^{-1}. (Photo #8318)……58

Figure 37: Fin model oriented at 14^{o} to the flow, with wind speed of 14.6 ms^{-1}. (Photo #8321)……59

Figure 38: Fin model oriented at 16^{o} to the flow, with wind speed of 14.6 ms^{-1}. (Photo #8338)……60

Figure 39: Fin model oriented at 8^{o} to the flow, with wind speed of 20.9 ms^{-1}. (Photo #8361)……61

Figure 40: Fin model oriented at 10^{o} to the flow, with wind speed of 20.9 ms^{-1}. (Photo #8352)……61

Figure 41: Fin model oriented at 12^{o} to the flow, with wind speed of 20.9 ms^{-1}. (Photo #8369)……62

Figure 42: Fin model oriented at 14^{o} to the flow, with wind speed of 20.9 ms^{-1}. (Photo #8378)……63

Figure 43: Fin model oriented at 16^{o} to the flow, with wind speed of 20.9 ms^{-1}. (Photo #8387)……63

Figure 44 : The boundary layer and distribution of pressure for foil cross-section charlie, determined from a Reynolds number of $1.5x10^{6}$ and a Mach number of 0.076, when the foil is oriented parallel to the flow……69

Figure 45: The location of boundary layer transition (side 1) for the RSX and NACA 65-009 foils……71

Figure 46: The location of boundary layer transition (side 2) for the RSX and NACA 65-009 foils……71

Figure 47: Streamlines showing attached flow about cross section charlie for a fin modelled at 8^{o} in water flowing at 1.42 ms^{-1}……75

Figure 48: Streamlines showing leading edge separation at cross section hotel for a fin modelled at 8^{o} in water flowing at 1.42 ms^{-1}……75

Figure 49: Streamlines showing attached flow around cross section echo, with slight separation towards the trailing edge for at 10^{o} in water flowing at 1.42 ms^{-1}……76

Figure 50: Streamlines showing leading edge separation at cross section hotel for a fin modelled at 10^{o} in water flowing at 1.42 ms^{-1}……76

Figure 51: Streamlines showing attached flow around cross section bravo, at a 12^{o} angle of attack in water flowing at 1.42 ms^{-1}……..77

Figure 52: Streamlines showing attached flow around cross section charlie, at a 12^{o} angle of attack in water flowing at 1.42 ms^{-1}……..77

Figure 53: Streamlines showing attached flow around cross section echo, with slight separation towards the trailing edge at 12^{o} in water flowing at 1.42 ms^{-1}……..77

Figure 54: Streamlines showing flow around cross section bravo, at a 14^{o} angle of attack in water flowing at 1.42 ms^{-1}……..78

Figure 55: Streamlines showing flow around cross section charlie, at a 14^{o} angle of attack in water flowing at 1.42 ms^{-1}……..78

Figure 56: Streamlines showing flow around cross section echo, with slight separation towards the trailing edge at 14^{o} in water flowing at 1.42 ms^{-1}……78

Figure 57: Streamlines showing separated flow around cross section hotel, at 14^{o} in water flowing at 1.42ms^{-1}……79

Figure 58: Streamlines showing the behaviour of the incoming flow at 5ms^{-1} and 10^{o} to the fin, across cross-section bravo……80

Figure 59: Streamlines showing the behaviour of the incoming flow at 5ms^{-1} and 10^{o} to the fin, across cross-section charlie……80

Figure 60: Streamlines showing the behaviour of the incoming flow at 5ms^{-1} and 10^{o} to the fin, across cross-section echo……81

Figure 61: Streamlines showing the behaviour of the incoming flow at 5ms^{-1} and 10^{o} to the fin, across cross-section hotel……81

Figure 62: Streamlines showing the behaviour of the incoming flow at 5ms^{-1} and 5^{o} to the fin, across cross-section hotel……81

Figure 63: Streamlines showing the behaviour of the incoming flow at 5ms^{-1} and 16^{o} to the fin, across cross-section echo, with glyphs (arrows) showing pressure……82

Figure 64: Streamlines showing the behaviour of the incoming flow at 5ms^{-1} and 20^{o} to the fin, across cross-section bravo……82

Figure 65: Streamlines showing the behaviour of the incoming flow at 10ms^{-1} and 10^{o} to the fin, across cross-section bravo……..83

Figure 66: Streamlines showing the behaviour of the incoming flow at 10ms^{-1} and 10^{o} to the fin, across cross-section charlie……83

Figure 67: Streamlines showing the behaviour of the incoming flow at 10ms^{-1} and 10^{o} to the fin, across cross-section echo……83

Figure 68: Streamlines showing the behaviour of the incoming flow at 10ms^{-1} and 10^{o} to the fin, across cross-section hotel……84

Figure 69: Streamlines showing a region of separation at the leading edge of cross section bravo for the incoming flow at 10ms^{-1} and 20^{o} with respect to the fin…….84

Figure 70: Streamlines showing the behaviour of the incoming flow at 15ms^{-1} and 10^{o} to the fin, across cross-section bravo……..84

Figure 71: Streamlines showing the behaviour of the incoming flow at 15ms^{-1} and 10^{o} to the fin, across cross-section charlie……85

Figure 72: Streamlines showing the behaviour of the incoming flow at 15ms^{-1} and 10^{o} to the fin, across cross-section echo……85

Figure 73: Streamlines showing the behaviour of the incoming flow at 15ms^{-1} and 10^{o} to the fin, across cross-section hotel……85

Figure 74: The flow streamlines are affected by the finite length of foil, causing cross flow……87

Figure 75: Tip vortices forming off of the tip of the fin, shown for flow at 10ms^{-1} and 20^{o}……87

List of Tables

Table 1: Displacement (in the y-direction) of each cross section from the top of the fin……25

Table 2: Maximum thickness as a percentage of the chord length of RS: X Racing 66 sailboard fin……25

Table 3: Distance of points a, b and c from the leading edge……29

Table 4: Points at and near the leading edge, used to determine the radius for each cross section……32

Table 5: Calculation of the leading edge radius for each cross section……33

Table 6: Measurement of trailing edge thickness……34

Table 7: Fluid properties for air and water……41

Table 8: Type of flow for various Reynolds numbers……42

Table 9: Boundary layer thickness for turbulent flow……43

Table 10: Lift coefficient for each angle of attack……45

Table 11: Lift coefficient for infinite and finite foil spans……48

Table 12: Manometer readings wind tunnel experiment 1……57

Table 13: Manometer readings wind tunnel experiment 2……57

Table 14: Equivalent speeds to air speeds tested……65

Table 15: Location of boundary layer transition on the RSX characteristic cross-section as calculated by XFOIL for various angles of attack……70

Table 16: Location of boundary layer transition on the NACA 65-009 as calculated by XFOIL for various angles of attack……70

Table 17: Equivalent velocities for computational, experimental and physical flows……74

1. Introduction

The purpose of this report is to examine and discuss the flow of water around the RS: X Racing 66 sailboard fin (similar in form to a NACA 65-009 foil) at different angles of attack and for differing fluid velocities and pressures, as well as for both laminar and turbulent flow.

These conditions shall be compared for both a computational analysis of the flow, and an experimental analysis. The computational analysis will be conducted using OpenFOAM, and the experiment shall be performed using a wind tunnel.

The dimensions of the fin were used to create a model of the fin in the CAD (computer aided design) program 'AutoCAD' (see chapter 7.5), and this model of the fin surface was output as an STL file. This file will be used to produce both a scale model of the fin for experimental (wind tunnel testing), and to describe the fin surface conditions for the computational analysis.

The wind tunnel test will be conducted using 'tell-tales' attached to the fin to visualise the fluid behaviour. The results of the wind tunnel experiment will compared with the results of the computational analysis, which will be conducted using OpenFOAM.

2. Background

2.1. Foils

The purpose of this report is to examine the behaviour of the fluids about a sailboard fin, a type of foil. To do so we must first examine the usual method of discussing and describing foils.

2.2.1. NACA foils

The National Advisory Committee for Aeronautics conducted research into the behaviour and aerodynamic characteristics of foils in the first half of the 20th Century (Abbott and von Doenhoff 1959). They developed a method to characterise the physical shape of the foils based on only a few parameters, namely:

- maximum thickness
- maximum camber
- position of the maximum camber relative to the chord length
- nose radius

(Kroo 2007; Abbott and von Doenhoff 1959; White 2011)

These parameters are shown in the diagram included below:

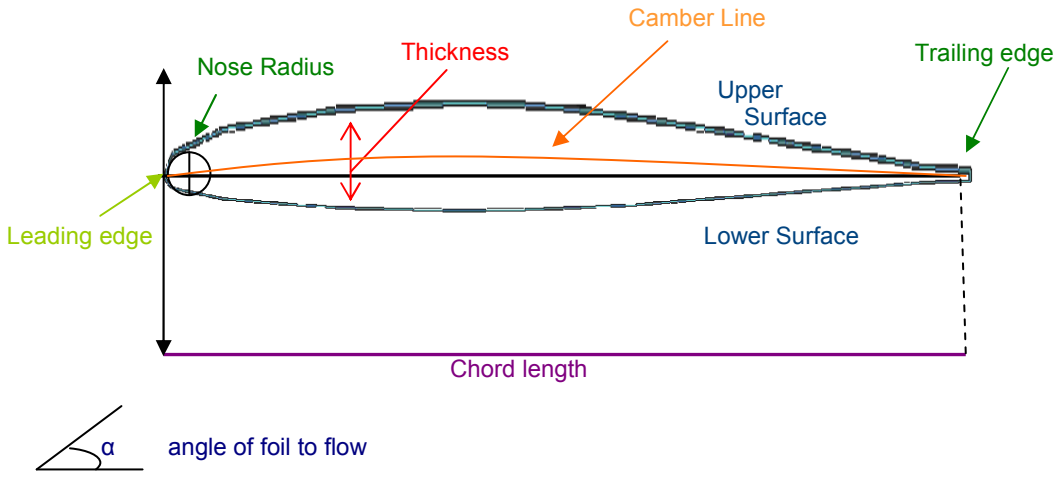

Figure 1: Cambered foil

Explanation of terms:

Camber

Mean line, half way between the upper and lower surfaces of the foil

Chord Length

Length of foil from the leading to trailing edge

Leading edge

Front or nose of the foil

Thickness
: Width of the foil at any given point

Trailing edge
: Back edge (tail) of the foil

In addition to implementing a new method of describing foil shape, the properties of the NACA airfoils, including lift, drag and moment were all examined, both theoretically and experimentally. (Kroo 2007; White 2011; Abbott and von Doenhoff 1959)

The three dimensional experimental data was obtained from tests carried out in a pressure tunnel. A two dimensional low turbulence pressure tunnel was used for predictions. (Abbott and von Doenhoff 1959)

2.2.2. NACA 6 series

There are multiple NACA series, all of which can be used to describe a foil in terms of its geometry and theoretical aerodynamic characteristics. For example, the NACA 5-digit series has a camber-line with more curvature towards the nose of the foil than the NACA 4-digit series (Kroo 2007). The series of interest to this report is the NACA 6 series, for reasons which shall be discussed in chapter 3.2.

The NACA 6-series has a greater accuracy than the previous series with respect to the leading edge of the foil profiles. Foils belonging to the NACA 6-series have been deliberately shaped to ensure favourable pressure gradients over significant portions of the upper surface (Abbott and von Doenhoff 1959; White 2011).

The NACA 6-series is typically denoted by the following format, where the #'s refer to a numerical component.

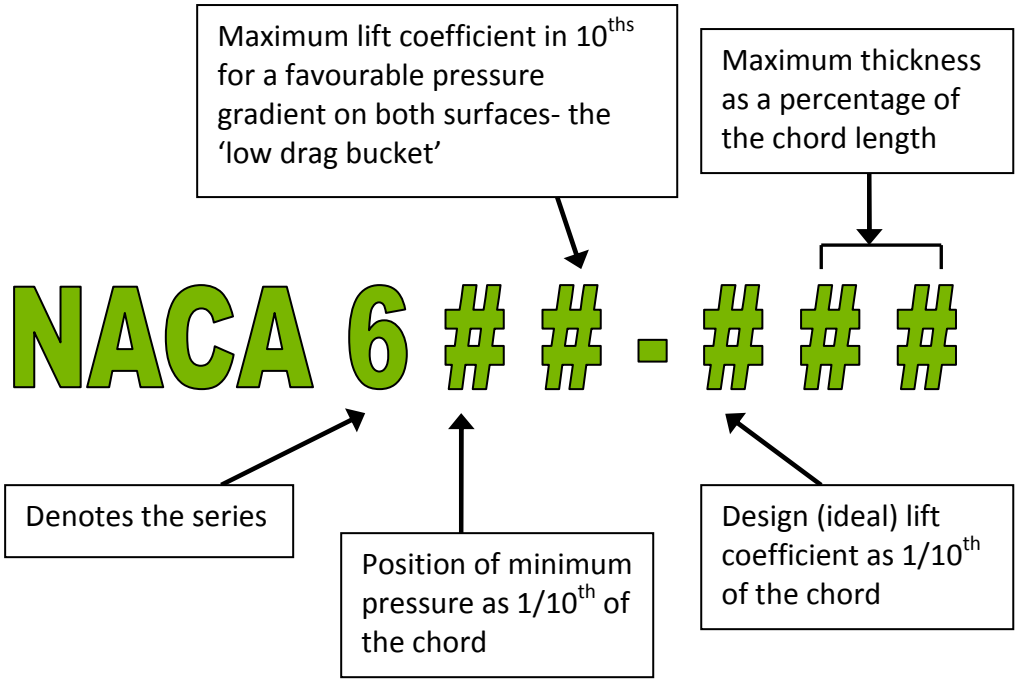

Figure 2: Typical method of writing NACA 6-series foil

The first digit signifies that the foil belongs to the NACA 6-series. The second digit represents the position of minimum pressure as $1/10^{th}$ of the chord. The third digit represents the size of the 'low-drag bucket'; the range of lift coefficient in 10^{ths} above and below the design lift coefficient in which favourable pressure gradients exist on both surfaces. The fourth digit supplies the ideal or designed lift coefficient as $1/10^{th}$ of the cord, and the fourth and fifth digits represent the maximum thickness as a percentage of the chord length (Kroo 2007; Abbott and von Doenhoff 1959; Fox, McDonald, and Pritchard 2004a).

Where a 6-series foil or wing section has a thickness-to-chord ratio of less than 0.12, the resultant low drag range on the foil is less than 0.1, and can therefore be omitted from the designation, as shown below. (Abbott and von Doenhoff 1959)

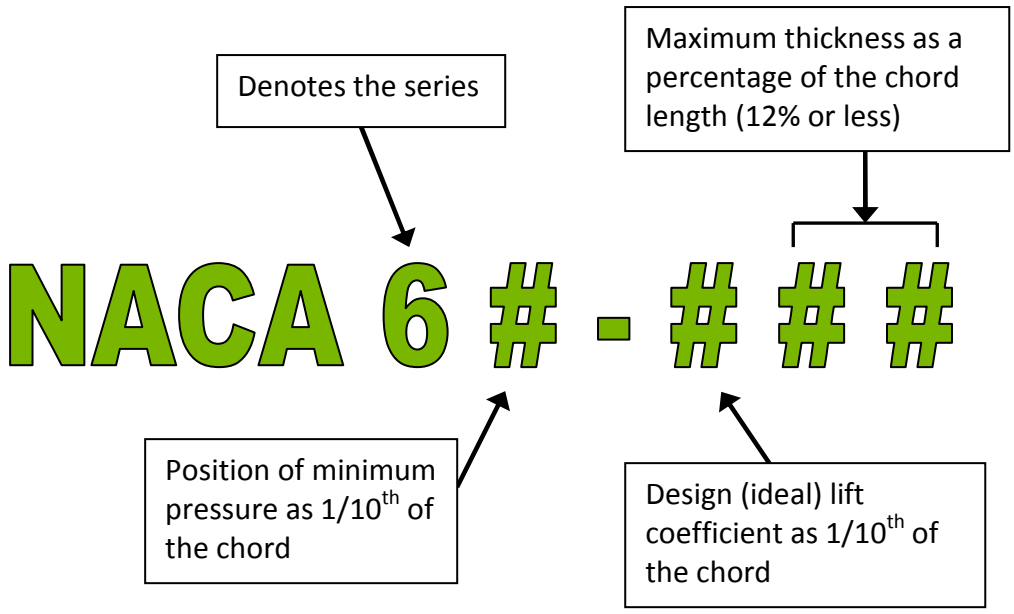

Figure 3: NACA 6-series designation for foils with thickness/chord ratios of less than 12%, and the low-drag range omitted.

It is determined in chapter 3.2 that the RS: X Racing 66 sailboard fin is very similar in shape to a NACA 65-009 foil.

2.2.3. RS: X Racing 66 Sailboard Fin

The RS: X is a one design sailboard class which has been in production since 2005, and is suitable for racing in wind speeds varying from 3 to 30 knots. The board itself is capable of 11-14knots upwind, with the centreboard retracted, and is likewise capable of up to 24knots, downwind. (Gourlay and Martellotta 2011) The board comes in two sail sizes: the men's 9.5m^2 sail and the women's and youth's 8.5m^2 sail. The sail board has both a retractable centreboard and a fixed fin. It is the fixed fin which is the focus of this report. (Gourlay and Martellotta 2011; Ramsden 2009; NeilPryde Racing 2011b)

Figure 4: RS: X Men's Sailboard.

The centreboard is typically retracted for upwind planing in winds greater than 10 knots, and all downwind conditions. This means that the flow is moving solely around the fin in these conditions, which are those to be analysed (with particular interest to the upwind conditions) in this report.

The fin itself, like the sail, comes in two sizes: the men's board has a 66cm fin (RS: X Racing 66), and the women's (and youth's) board has a 60cm fin (RS: X Racing 60). (NeilPryde Racing 2011a)

Figure 5: Men's RS: X Racing 66 fin (side A)

The force provided by the wind acting on the sail produces a force acting perpendicular to the sail.

The purpose of the fin is to constrain the motion of the board so that the sailboard can only move forwards (or backwards) with respect to the fin. (Hewitt 1998; Burgess 1974) Where the force of the wind acting on the sail is aligned with the fin, this is true. However, where the force of the wind is *not* parallel to the fin, the fin is able to constrain most of this force into a forwards motion of the board, but the board itself will experience a small component of velocity sideways. (Li 2008; Creagh-Osborne and Milne 1973; Garrett 1987)

Since board is being blown slightly sideways, in addition to sailing forwards, the direction of motion of the board is not the same as the heading (the direction in which the board is pointed). (Garrett 1987) The angle between the direction of motion and the heading is known as the leeway angle. This means that the leeward side of the board is the upstream side of the fin. (Li 2008; Burgess 1974; Garrett 1987)

Thus the motion of the sailboard has a directional component which causes the water to flow at a slight angle to the fin. This angle is referred to as the leeway angle.

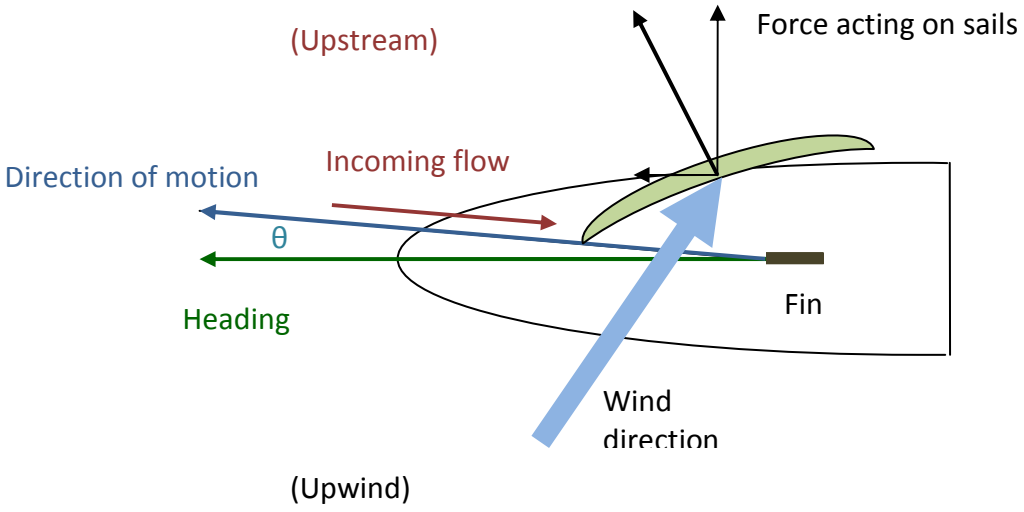

Figure 6: The wind acting on the sail causes the board to move at an angle to the heading, and this is the angle of attack of the flow with respect to the fin. (Not to scale).

2.2.4 Consequences of similarity to NACA 65-009

If the closest NACA cross section to the RSX fin is a 65-009, then the RSX 66cm windsurfing fin can be expected to mimic some of the properties characterising the NACA 6 series class.

The advantages of the NACA 6-series include:
-high maximum lift coefficient
-attached flow and low drag over a small range of operating conditions
-optimised for high speed use
-fairly consistent pressure distribution across the fin surface
(Marzocca 2004; Abbott and von Doenhoff 1959)

The disadvantages include:
-limited range of operating conditions
(Marzocca 2004; Abbott and von Doenhoff 1959)

Thus, it can be expected that the flow will be primarily attached across the foil's surface for a limited range of angles of attack with respect to the flow. (Marzocca 2004; Abbott and von Doenhoff 1959; Public Domain Aeronautical Software 2010)

2.3 Computational Fluid Dynamics (CFD)

The behaviour of fluid can be described by the basic conservation laws of energy, mass, and momentum, in three dimensions and with respect to time. These equations are called the Navier-Stokes equations, and can be used to describe the flow of incompressible fluids. (White 1999; Glenn Research Centre 2008)

Put simply, computational fluid dynamics (CFD) is "the process of modelling fluid flows by the numerical solution of the governing partial differential equations or other mathematical equations of motion." (CSIRO 2009)

Fluid behaviour can be modelled computationally to determine solutions to problems which would otherwise be too complex to solve analytically, including turbulent or separated flows. (White 1999)

3. Computer generated model

The RS:X windsurfing fin was measured and modelled using AutoCAD, to create an accurate three-dimensional model of the surface so that the fluid behaviour can be suitably analysed in both OpenFOAM and the wind tunnel.

The leading edge radius which is too small to be accurately measured by hand was calculated using Microsoft Excel, and data points along the surface generated to fill the leading edge of each of the y-displacements measured.

The data points collected were then entered into AutoCAD, and used to form cross sections of the fin at each y-displacement. Using the 'loft' command, the three dimensional fin was formed by extruding across these cross sections, and the surface was then saved and exported as an STL file. This file format enabled the data to be used by both OpenFOAM to produce a computational model of the fin, and by the rapid prototyper to produce physical model of the fin. This, in turn, allowed fluid behaviour around the fin to be analysed at different angles of attack, and a comparison between the expected (computational) behaviour and the actual (wind tunnel) behaviour to be made.

3.1. Measuring the Fin

Since manufacturers often prefer not to release specifications for their foils, the actual dimensions of the RS: X Racing 66 sailboard fin needed to be measured. This task was undertaken by using a set-square and a metal ruler accurate to 1 mm (uncertainty of ± 0.5 mm). With these, both sides of the fin were divided into 6 equal sections, each 110mm high. Due to the curvature of the fin base, the bottom y-displacement used was 5mm above the bottom of the fin, and another set of points were measured half way between the bottom of the fin and the set above it.

The curvature of the fin surface causes an additional uncertainty in the transverse (x) and longitudinal (y) measurements across the fin surface.

Ruler uncertainty	0.5mm
Surface curvature	+ 0.5mm
Total uncertainty in x and y	± 1.0 mm

From this, after checking that both sides matched, each y-displacement line was divided into 5 mm intervals, measured back from the leading edge.

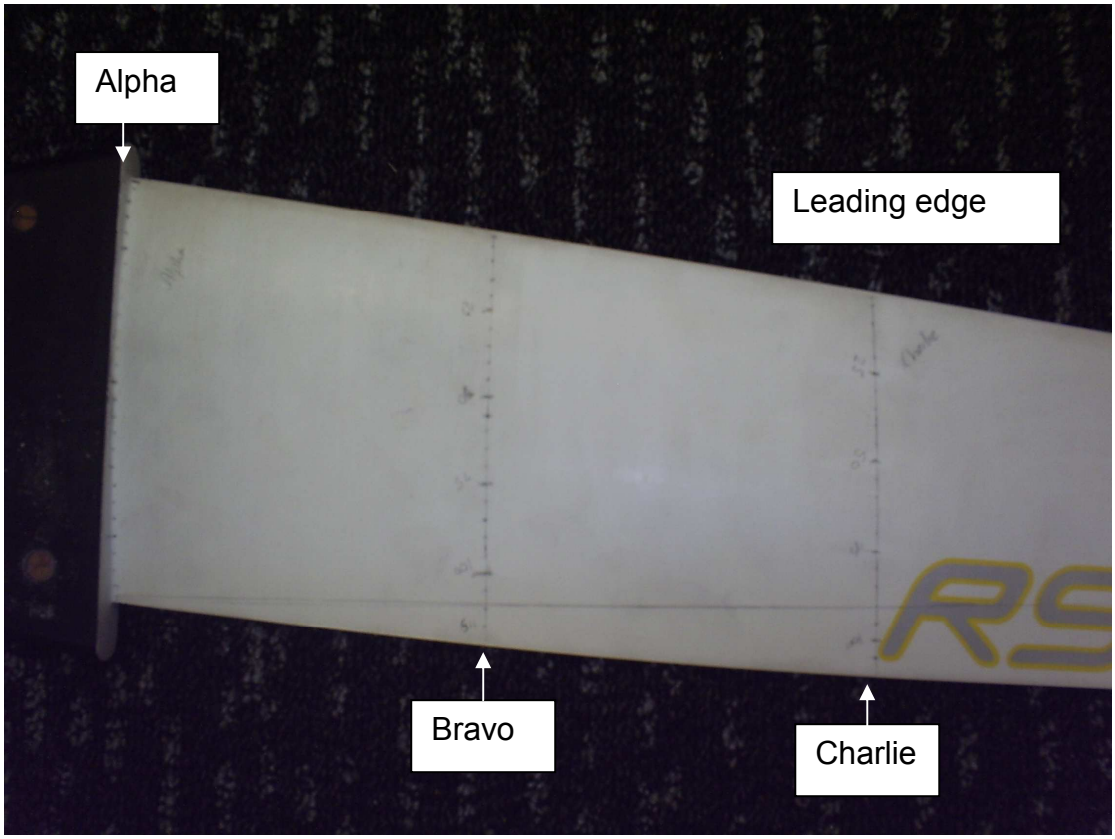

Figure 7: 5mm intervals along y-displacements alpha, bravo and charlie, fin side A.

The fin was then clamped, and the thickness measured using a vernier (uncertainty of ±0.005mm), with each side of the jaw aligned on both sides of the fin for each interval.

The uncertainty in the foil thickness was determined by considering the effect of the longitudinal and transverse uncertainties, in addition to the uncertainty in the verniers. The effect of the measurement of the surface position was achieved by estimating the maximum slope of the fin in both the XZ and YZ planes.

In the XZ plane, it was assumed the maximum slope would occur on the thickest cross-section: y-displacement alpha, shown below.

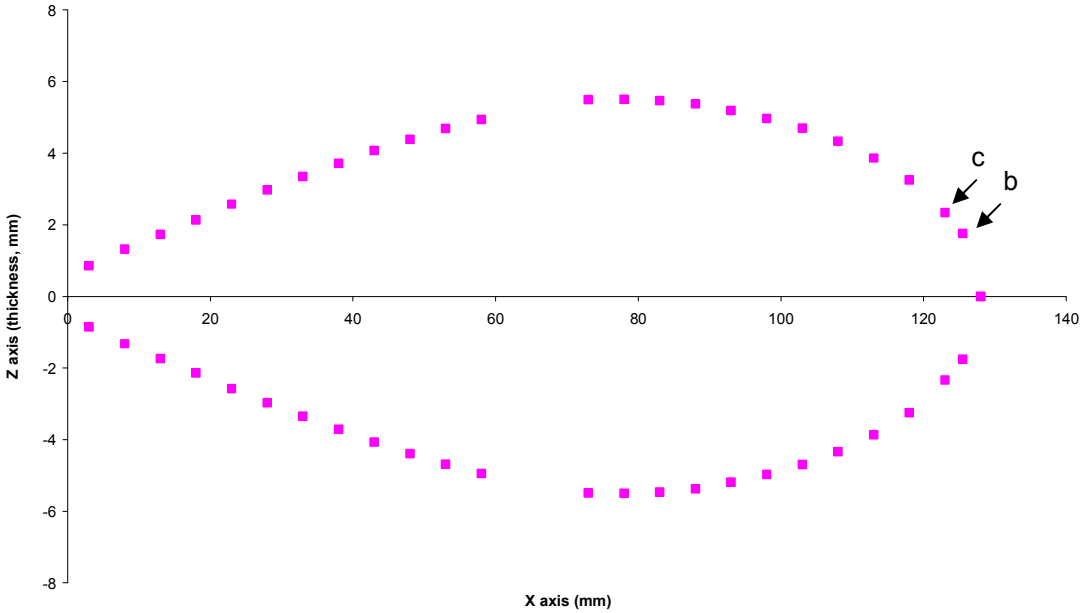

Figure 8: XZ cross section (y-displacement alpha), shown here on axes of unequal scale.

Visually, it can be determined that the position of the maximum gradient (not including the leading edge radius, not shown) occurs between point's b and c.

The gradient between point's b and c was determined as follows:

$$gradient = \frac{rise}{run}$$

$$xz\_gradient = \frac{\Delta z}{\Delta x} = \frac{c_z - b_z}{c_x - b_x}$$

$$\left|xz\_gradient\right| = \left|\frac{2.335 - 1.755}{123 - 125.5}\right| = 0.232 \qquad \text{(3 significant figures)}$$

The maximum gradient in the YZ plane was determined using the slope between alpha and the leading edge of bravo. (See figure below).

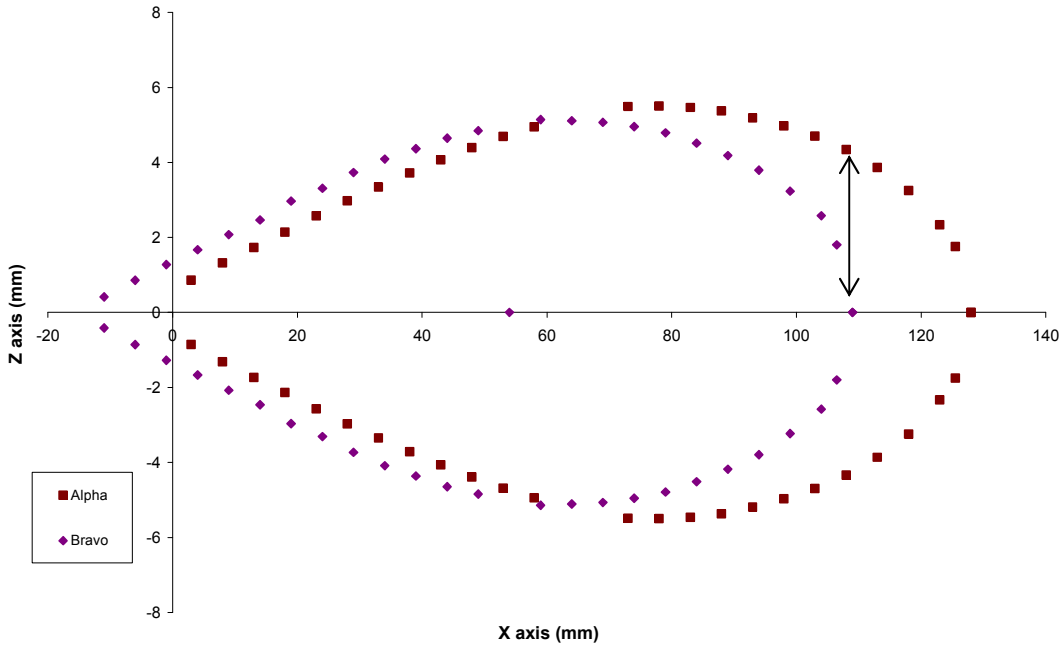

Figure 9: XZ cross sections of y-displacements alpha and bravo.

The gradient between y-displacements alpha and bravo was determined as follows:

$$gradient = \frac{rise}{run}$$

$$yz\_gradient = \frac{\Delta y}{\Delta x} = \frac{c_y - b_y}{c_x - b_x}$$

$$\left|yz\_gradient\right| = \left|\frac{4.335 - 0}{0 - -110}\right| = 0.039 \qquad \text{(3 significant figures)}$$

The total uncertainty in the foil thickness was therefore determined by taking the RMS (root mean square) of the uncertainties acting in each of the three different directions.

$$uncert = \sqrt{\frac{(\Delta XZ)^2 + (\Delta YZ)^2 + Z^2}{3}}$$

$$uncert = \sqrt{\frac{(0.232)^2 + (0.039)^2 + 0.005^2}{3}} = 0.136 \qquad \text{(3 significant figures)}$$

The total uncertainty in the total thickness at any point is therefore ±0.1mm.

The verniers were unable to measure the central points on the longer y-displacements of alpha and bravo. The data points at these values were calculated by interpolating using MatLab, with a program written for the purpose called mysolvemissing.m. The code has been attached in appendix 13.1.1.

The foil thickness was interpolated for the following position vectors on the fin surface, where the position vectors have been included in the form (x, y):

- (68, 0)
- (63, 0)
- (54, -110)

3.1.1. Coordinate System

The coordinate system used to describe the position on the surface of the fin at any given point was defined as shown in the figure below:

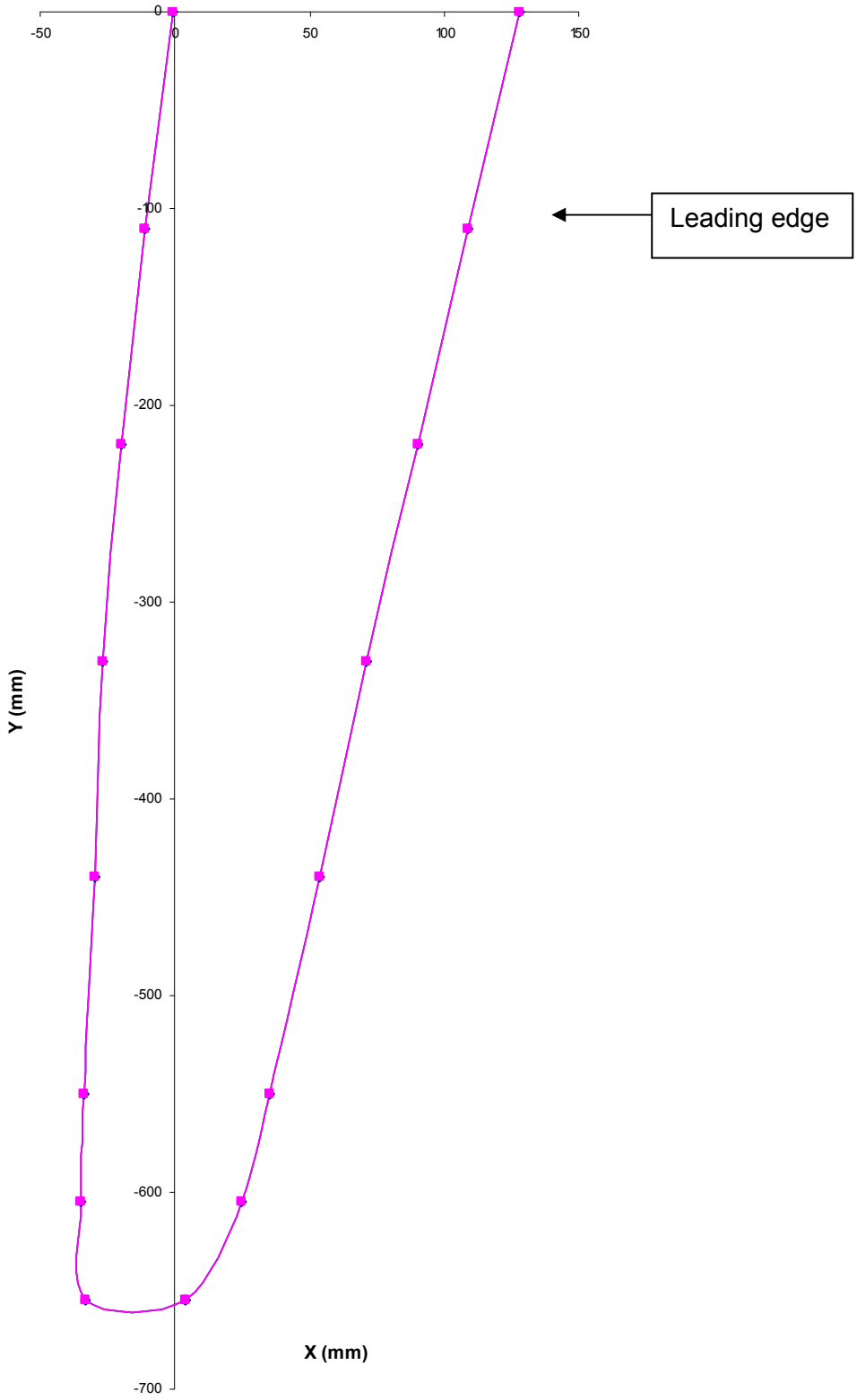

Figure 10: Leading edge of the fin shown using the excel model of the fin viewed in the XY plane, shown here on axes of unequal scale.

As shown in the above diagram:

- The x coordinate refers to the distance parallel to the top of the fin/fluid surface forward from the surface trailing edge.

- The y coordinate refers to distance perpendicularly above or below the top of the fin/fluid surface, with height above as the positive direction.

- The z coordinate refers to the thickness from the centre of the fin.

The fin was measured at the following positions along the y axis:

Table 1: Displacement (in the y-direction) of each cross section from the top of the fin.

Y-displacements	*Distance from y axis (mm)*
Alpha	0
Bravo	-110
Charlie	-220
Delta	-330
Echo	-440
Foxtrot	-550
Golf	-605
Hotel	-660

The thickness of the fin (double the z-value) was measured every 5mm along the x axis from the leading edge to the trailing edge at each of these y-displacements.

3.2. Comparison to NACA foil sections

The RS: X Racing 66 has, as was discussed in chapter 2.2.3, 0 camber as the foil is symmetric, and hence has a 0 lift coefficient. The maximum thickness is 8.8% (9%) of the chord length, as calculated as shown in the table below.

Table 2: Maximum thickness as a percentage of the chord length of RS: X Racing 66 sailboard fin.

Y-displacement	**Chord (mm)**	**Maximum thickness (mm)**	**Maximum thickness as a percentage of the chord length**
alpha	129	11.00	8.53
bravo	120	10.28	8.57
charlie	110	9.51	8.65
delta	98	8.53	8.70
echo	84	7.38	8.79
foxtrot	69	6.06	8.78
golf	60	5.22	8.70
hotel	37	3.62	9.78
Average:			**8.81 %**

The point of minimum pressure was located using boundary layer analysis in XFOIL. (See section 5.1). However, from the information discussed thus far, it can be concluded that the fin has the form of a NACA 6#009 foil. To determine which particular NACA section the fin most closely resembles, the x-z coordinates of each cross section were compared to coordinates for sections obtained from Public Domain Aeronautical Software (PDAS) (2010).

It was first determined that all of the cross sections (excepting hotel) follow the same relationship with regard to foil thickness as a percentage of the chord length. It is thought that hotel does not follow this pattern since it was measured at the very tip of the foil.

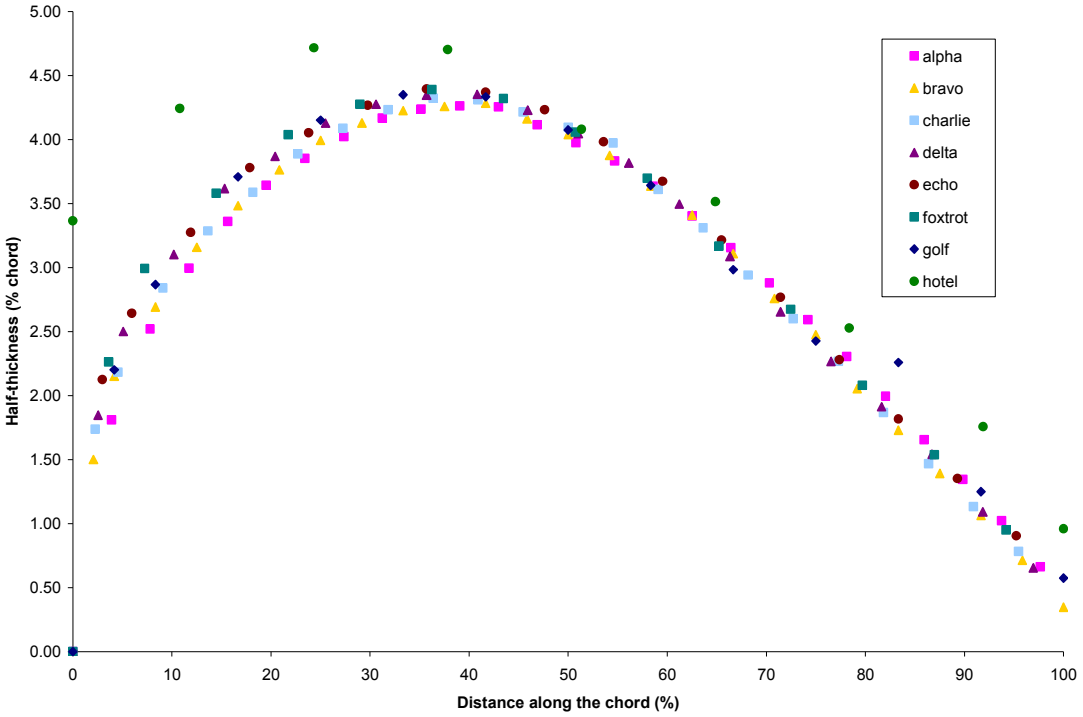

Figure 11: Profile of the fin for each cross section in terms of the percentage of total chord length, shown here on axes of unequal scale.

The profile measured across y-displacement charlie was used as the representative displacement for each of the following graphs.

The foil thickness as a function of chord length was compared against the profiles of several NACA sections, including the 65-008, 65-009, 65-010 and 66-009, as shown below.

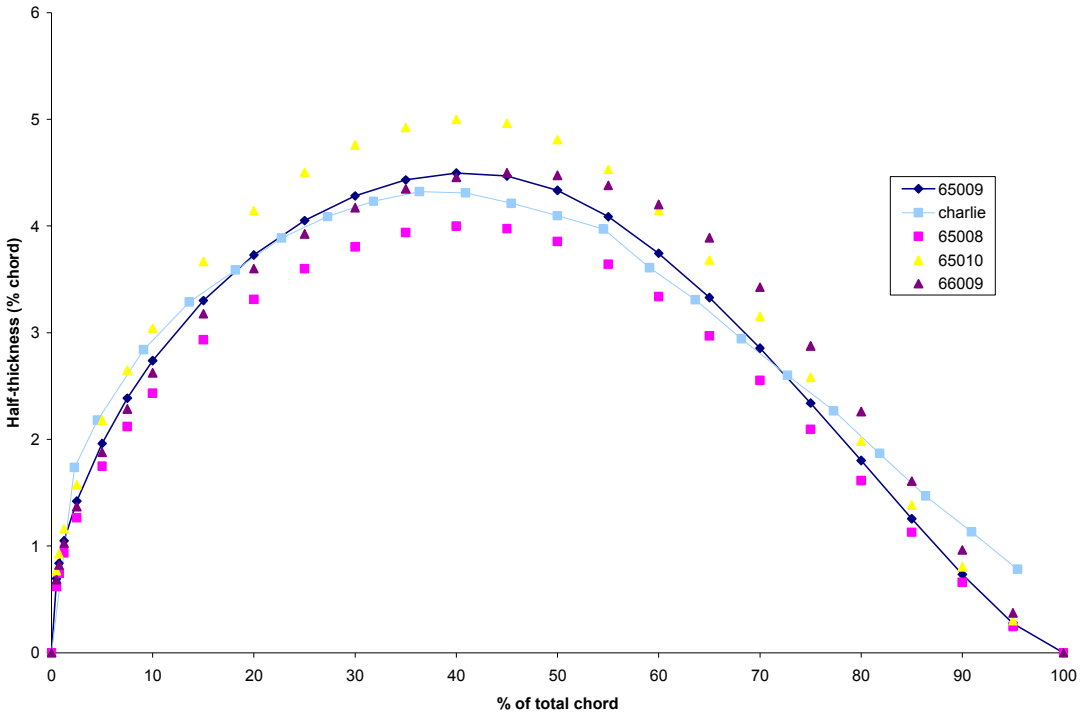

Figure 12: Profile of the RS: X Racing 66 windsurfing fin compared against several NACA sections.

Of these, the 65-009 (dark blue) appears to bear the closest resemblance to the profile of the RS: X Racing 66 windsurfing fin (shown here in light blue). The RS: X and NACA 65-009 have been shown separately in the following graph.

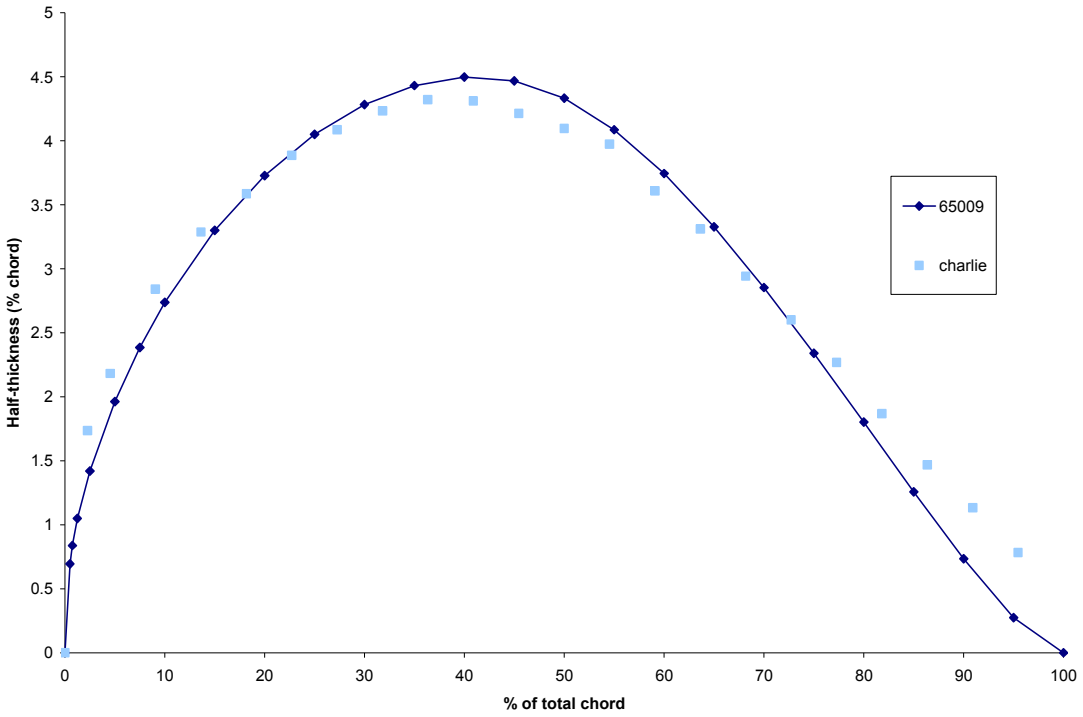

Figure 13: NACA 65-009 foil section profile compared with the profile of the RS: X 66 windsurfing fin (y-displacement: charlie).

From the above figures, it was concluded that the RS: X Racing 66 sailboard fin has a similar profile to a NACA 65-009 foil.

3.3. Leading Edge Radius

The shape of the leading edge impacts the drag and the likelihood of separation or stall occurring at the leading edge. (Martellotta 2010.)

Reducing the leading edge radius (sharpening the nose) will reduce the drag, but will increase the flow velocity about the leading edge, increasing the likelihood of the flow separating (or stalling) from the foil surface (Marchaj 1979). In addition to this, reducing the leading edge radius can reduce the overall maximum lift coefficient (Marchaj 1979).

The relative smoothness or sharpness of the curve of the leading edge changes the interaction of the fluid with the surface of the foil. Where the surface of the leading edge is smoothly curved, the flow will stick, rather than instantly separate from the foil. It is therefore crucial to the success of both the physical (wind tunnel) experiment, and the computational (OpenFOAM) exercise that the shape of the foil at the leading edge be modelled correctly.

As the radius of the fin's leading edge is too small to be accurately and precisely measured by hand, the leading edge radius was calculated using the first three points measured with respect to the leading edge: a, b, and c, see figure 23, below.

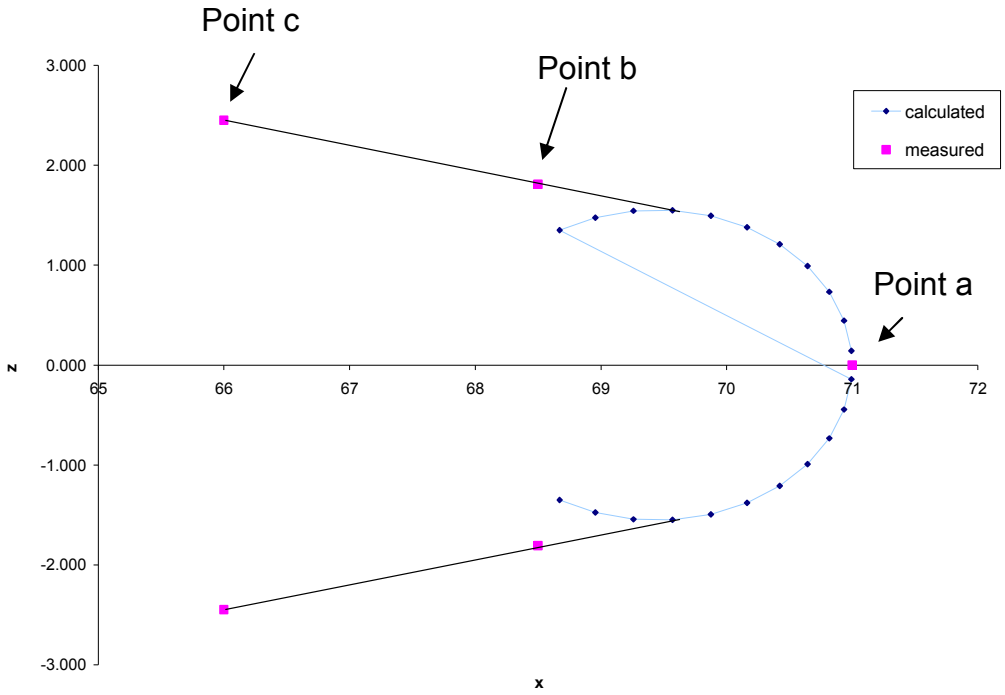

Figure 14: Leading edge showing measured points a, b and c, which were used to determine the leading edge radius. Also shown are the associated (calculated) points describing the surface of the leading edge radius. The above diagram was produced from the data measured for y-displacement delta.

Table 3: Distance of points a, b and c from the leading edge.

Point	X-distance from the leading edge (mm)
A	0
B	2.5
C	5

As shown in the figure below, the direct distance, f, between point a (the tip of the fin at the leading edge) and point b can be easily determined. The assumption is made that point b is located along the leading edge. Therefore a radius is required such that points a and b are equidistant from the 'centre', and such that the slope at b is increasing towards point c.

The slope at point b is determined by considering it to be equal to the slope of the fin between point's b and c. This allows for a smooth transition between the leading edge radius and the remainder of the fin, as shown in the figure below.

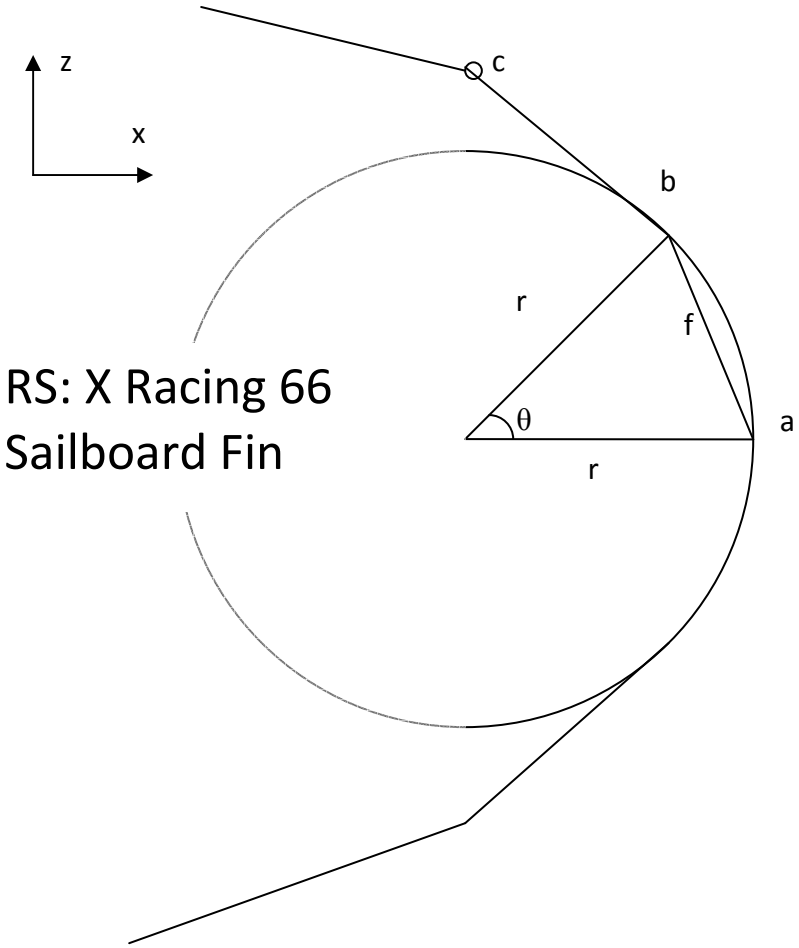

Figure 15: Calculation of the leading edge radius.

Taking the slope at point b into account will enable the value of the radius, r, and central angle, θ, to be calculated for each set of y-displacements. The trigonometry is shown in the figure below.

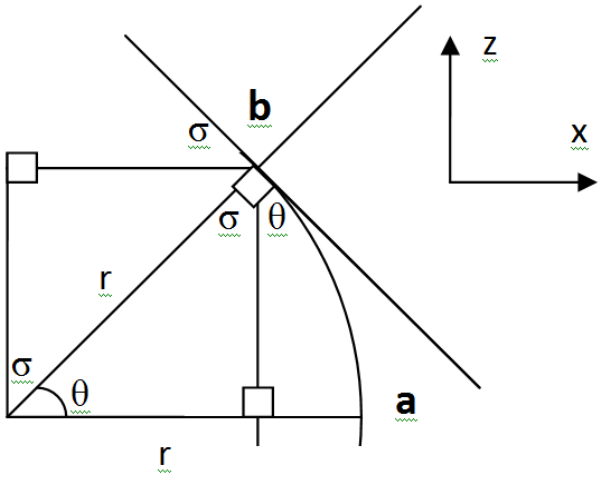

Figure 16: Trigonometry used to describe the leading edge radius.

The direct distance between points a and b, here called f, can be calculated from the x and z coordinates of points a and b:

$$f = \sqrt{(x_b - x_a)^2 + (z_b - z_a)^2}$$

Since the radius ray from the centre to point b is perpendicular to the slope at point b, angles σ, θ and χ can be calculated:

$$\sigma = \tan^{-1}(m)$$

$$\sigma = \tan^{-1}(\frac{\Delta z}{\Delta x})$$

From this, angle θ can be calculated:

$$\theta = \pi - \sigma$$

Setting χ such that:

$$\chi = \frac{\pi - \theta}{2}$$

As all angles of interest are now known, the sine rule can be applied to determine the radius, r:

$$\frac{r}{\sin(\frac{\pi}{2})} = \frac{f * \sin\chi}{\sin\theta}$$

Since $\sin(\frac{\pi}{2}) = 1$, this becomes:

$$r = \frac{f * \sin(\chi)}{\sin(\theta)}$$

$$r = \frac{f * \sin(\frac{\pi - \theta}{2})}{\sin(\theta)}$$

Using the coordinates measured for points a and b, the leading edge radius and maximum angle, θ, was determined for each set of y-displacements.

These were used to generate a series of position points to describe the surface between points a and b, both above and below the x axis (in the z plane). The number of points generated is dependent on the change in angle θ from 0 to θmax.

$$-\theta_{\max} \le \theta \le \theta_{\max}$$

The relative change in angle θ used was:

$\Delta\theta = 0.2$ radians.

This change in angle was chosen because it produced enough data points to give a smooth leading edge, without being unnecessarily precise, since the z uncertainty is 0.07mm, where z is half the thickness at any given point. Therefore, the angle used was sufficient for the purposes of OpenFOAM and the wind tunnel testing.

This produced 8 points each above and below the x axis, in addition to point a, and the points at ± b.

The radius for displacements alpha: golf were determined using the following measured points at the leading edge.

Table 4: Points at and near the leading edge, used to determine the radius for each cross section

		a		**b**		**c**	
Y-level	y	x	z	x	z	X	Z
Alpha	0	128	0	125.5	1.755	123	2.335
Bravo	-110	109	0	106.5	1.800	104	2.580
Charlie	-220	90	0	87.5	1.910	85	2.400
Delta	-330	71	0	68.5	1.810	66	2.450
Echo	-440	54	0	51.5	1.785	49	2.220
Foxtrot	-550	35	0	32.5	1.560	30	2.065
Golf	-605	25	0	22.5	1.320	20	1.720

The radii were determined as discussed above, and where the calculated radii appeared too large for the data points, they were adjusted as required to fit with the measured data points, as shown below.

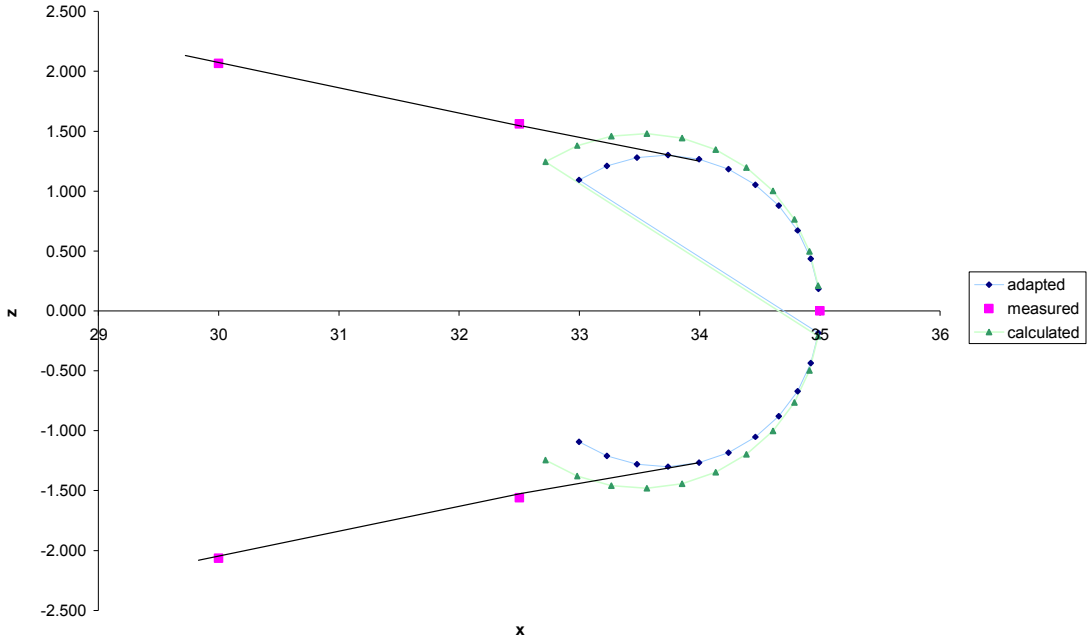

Figure 17: The adapted and calculated radii and leading edges shown with measured points a, b and c, for cross section foxtrot.

As shown by the above figure, not all of the calculated radii fit correctly with the measured data points. In these cases (foxtrot and golf), the radii was adapted to fit such that the slope connecting the leading edge points to the measured data points appeared smooth, to prevent a sharp join which would increase the likelihood of flow separation.

Table 5: Calculation of the leading edge radius for each cross section

	Calculated radius (mm)	Adapted radius (mm)	Used radius (mm)	Centre position relative to 0 in the x-axis (mm)
Alpha	1.54		1.54	126.5
Bravo	1.56		1.56	107.4
Charlie	1.58		1.58	88.4
Delta	1.56		1.56	69.4
Echo	1.54		1.54	52.5
Foxtrot	1.48	1.3	1.30	33.7
Golf	1.42	1.1	1.10	23.9
Hotel	2.15	1.57	1.57	2.4

The radius used for hotel was determined by averaging the calculated radii of the other y-displacement data sets.

The radii used are very similar, especially given the uncertainty in the z direction is ±0.07mm. The radii determined for cross sections alpha-echo and hotel all fall within uncertainties of each other. The radii determined for cross sections foxtrot and golf do not. Since the aim of this report is to analyse the behaviour about the

RS:X Racing 66 windsurfing fin, the adapted radii were used for these cross sections as they were adapted to fit smoothly with the measured data points.

3.4. Trailing Edge

The trailing edge of the RS: X sailboard fin has a finite thickness along the edge. This prevents the molecules comprising the boundary layer from accumulating at the trailing edge, by causing them to be sucked into the fin's wake. (Marchaj 1979) Since we are attempting to model a real fin, it is not unreasonable for the thickness to vary along this edge. The thickness was measured at the trailing edge for each cross-section, and was used as the thickness of the trailing edge in the modelled fin.

Table 6: Measurement of trailing edge thickness

	Thickness (mm ± 0.1mm)	Half-thickness (mm ± 0.07mm)
Alpha	1.72	0.86
Bravo	0.84	0.42
Charlie	1.72	0.86
Delta	1.28	0.64
Echo	1.52	0.76
Foxtrot	1.32	0.66
Golf	0.70	0.35
Hotel	0.72	0.36

The uncertainty in the measurement of the thickness at the trailing edge is fairly significant, ranging from 5.8% - 14.3% of the total thickness. Despite this, there is still a considerable variation in the width of the trailing edge of the fin, as shown below.

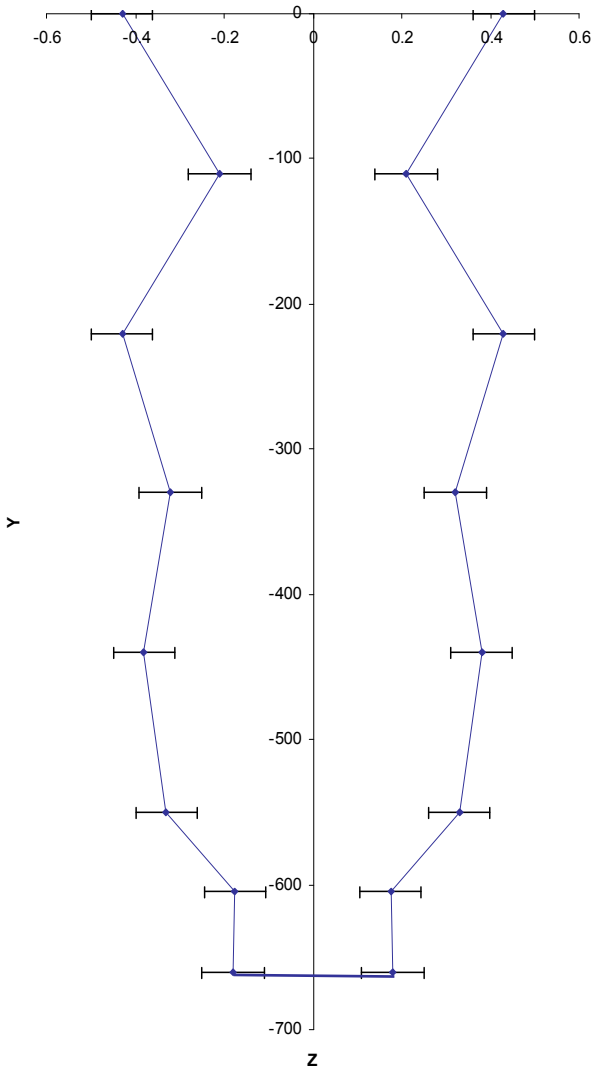

Figure 18: Trailing edge of the fin.

3.5. AutoCAD

AutoCAD is a type of computer aided design software, capable of both two-dimensional and three-dimensional modelling. It has workspaces which can be used to separate different levels of data, and is capable of outputting surfaces as STL files, which were all requirements of the computer modelling software used to model the fin. (Whitton 2011; Engineers Edge 2011; AutoCAD 2009)

The AutoCAD software was used to create a three-dimensional model of the RSX sailboard fin, based on the measurements of thickness as were measured based on the coordinate system described above.

The calculated leading edge radius values were added to the measured values across the fin surface. These were then entered into the AutoCAD software, such that each set of y values (alpha, bravo, charlie etc.) formed a half of a two dimensional 'teardrop', as shown below.

Figure 19: Top view of the half teardrop produced from the data points of y-displacement delta modelled in AutoCAD.

Each y-displacement was composed of a different number of data points, as a consequence of taking measurements every 5mm. To ensure that the three dimensional extrusion behaved appropriately around the leading and trailing edges, each cross section was interpolated using MATLAB so that each level had the same number of data points (35, the number originally measured for cross-section alpha). This then allows the loft function to extrapolate between the points evenly, rather than 'wrapping' the function about the corners.

The coordinates in each half teardrop were interpolated so that each cross section would be produced from the same number of data points. The program used for this purpose, interpPoints.m has been included as appendix 13.1.2.

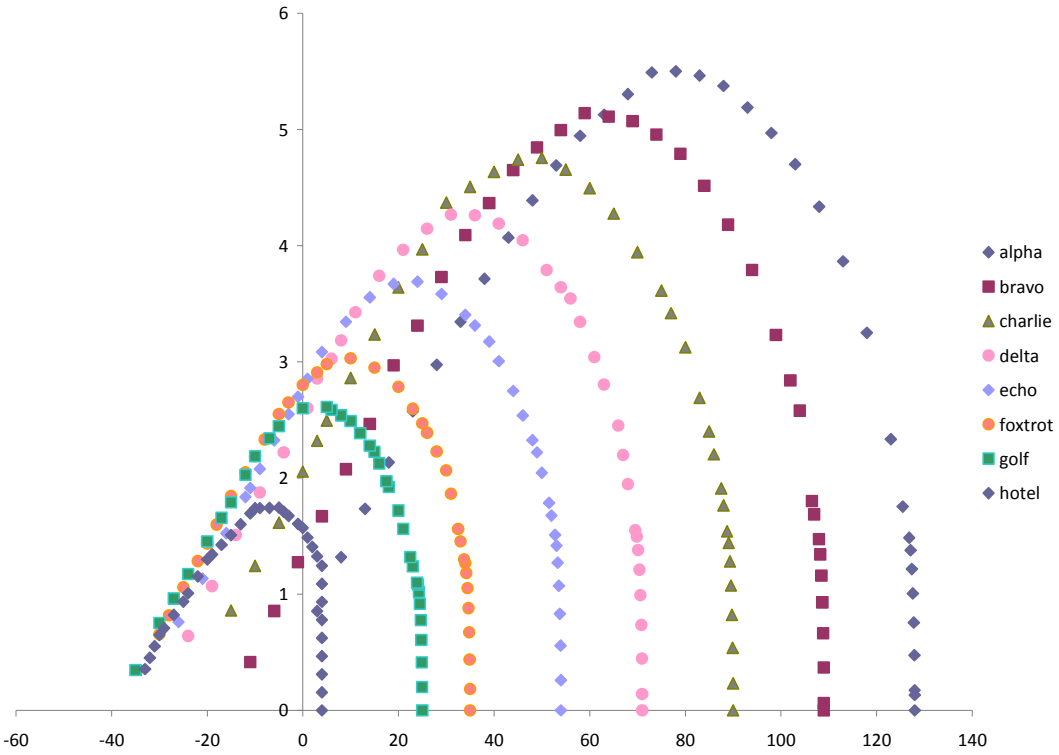

Figure 20: Y-displacements alpha to golf interpolated to have the same number of data points.

Each data point was entered in terms of its three dimensional coordinates, so that the data points modelled the fin correctly in terms of three dimensional space.

Figure 21: Top view of y-displacement delta modelled in AutoCAD.

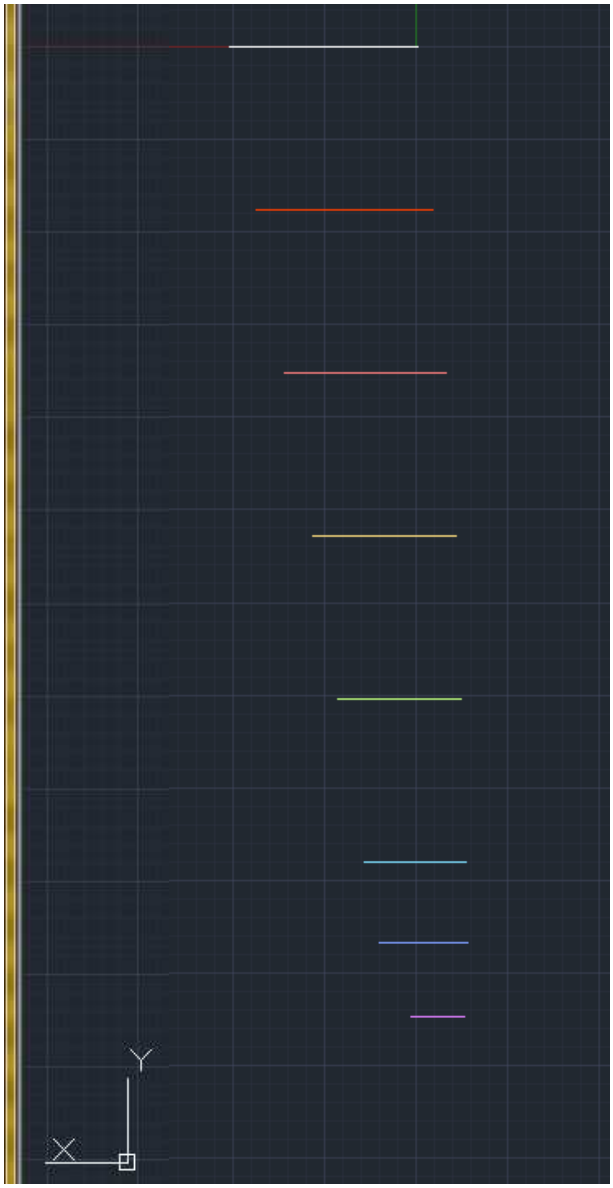

Figure 22: All cross sections shown in the XY plane, as modelled in AutoCAD.

The three dimensional fin shape was created by 'lofting' (extruding) across these two dimensional representations of the foil. The end result has been included below. The finished surface was output as a STL file for use in the OpenFOAM and by the Rapid Prototyper.

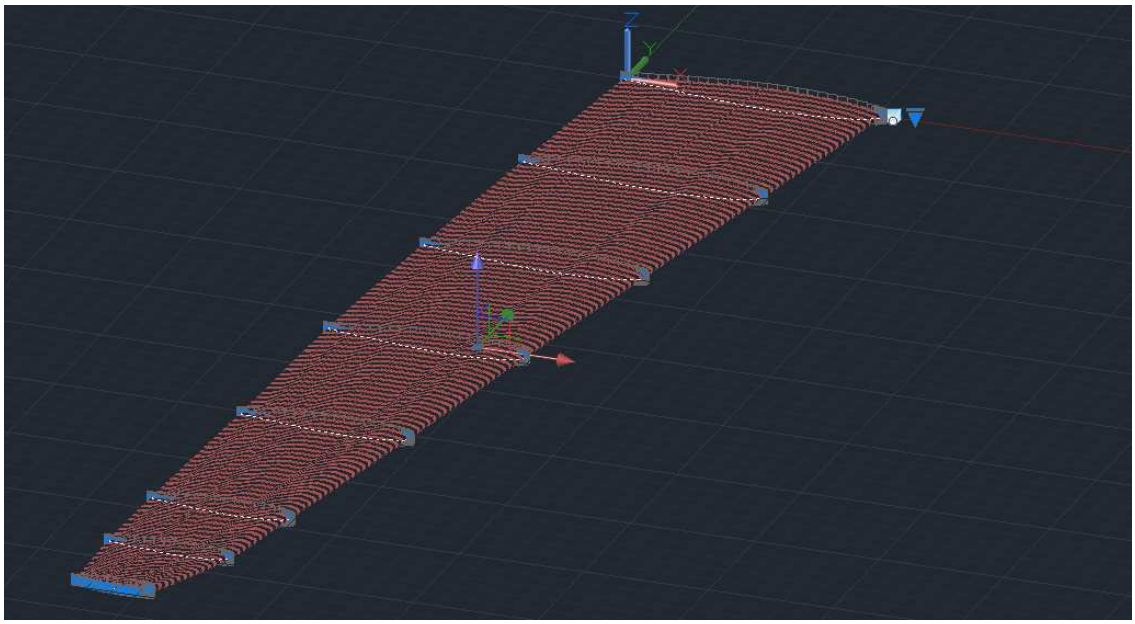

Figure 23: Finished three-dimensional model of the RS: X Racing 66 windsurfing fin, as modelled in AutoCAD, with data points showing.

3.6. STL Files

After producing the three dimensional fin surface, the data points were saved as an STL file, the standard file format used by Rapid Prototypers, which approximates a surface as a series of triangles. (Engineers Edge 2011; Fox, McDonald, and Pritchard 2004a).

The STL file was then sent to the 3D Printer (Rapid Prototyper) to produce a scale model of the RS: X sail board fin to be used in the wind tunnel tests.

As the STL file format is also used by OpenFOAM, the output STL file was used to create the surface, using the snappy hex mesh function.

4. Experimental Analysis

A simple method of mapping stall is to attach pieces of string (referred to as tell-tales) to the fin to give a visual guide to the air flow around the fin. The air flow can be mapped depending on the behaviour of the tell-tales. Smooth (attached) air flow can be shown by string that moves with the fluid, i.e. is parallel to the direction of flow, whilst regions of stall, such as a leading edge separation bubble or full stall are shown by chaotic string behaviour that does not mimic fluid propagation. Full stall can be identified where all strings after an initial chaotically behaved string also display random, chaotic motion. Meanwhile, leading edge separation bubbles can be identified by a region of chaotically behaved strings followed by a region of well behaved, flow conforming strings.

Figure 24: Attached tell tale behaviour. (Cropped from photo #8361)

Figure 25: Separated tell tale behaviour. (Cropped from photo #8369)

The flow was analysed by using the rapid prototyper to produce a scale model of the fin, to which tell-tales were then attached. The fin was then placed into a wind tunnel at various angles to the flow, and the behaviour of the tell-tales recorded.

4.1. Wind Tunnel

To make it possible to test the behaviour of fluid about the RS: X sailboard fin when is inclined at various angles to the flow, a wind tunnel was used. The experiments were conducted in the Curtin University wind tunnel.

The wind tunnel can be used to conduct these tests provided the model is "geometrically similar" to the fin and the Reynolds number is maintained between the 'scale model' fluid (air) and the 'full scale' fluid (water). (Abbott and von Doenhoff 1959, 81)

Due to the dimensions of the wind tunnel, a scale model of the fin was required. This was produced using AutoCAD, as mentioned in chapter 3.5, in conjunction with Curtin University's rapid prototyper, as mentioned below.

The flow around the foil can be examined by observing and recording the behaviour of tell-tales (tufts) attached across the surface of the foil. (Marchaj 1979)

4.1.1 Dynamic Similarity

Similarity is required when producing a model of a system. Maintaining similarity ensures that the model system has equivalent flow conditions to the full scale system. This is achieved by ensuring that the dimensionless parameters hold the same values for both the model and prototype. (White 1999)

Reynolds number is a dimensionless parameter relevant to almost all fluid mechanics problems. The Reynolds number is only relevant for viscous flows. Thus, the Reynolds number must be maintained for the flow across a model and prototype of an object to be considered comparable. (White 2008; Munson, Young, and Okiiski 2006)

The Reynolds number is dependent on the density ρ, viscosity μ, relative scale of the dimensions of the immersed model and full-size object, D, and the fluid velocity, V, as shown below.

$$\mathrm{Re} = \frac{\rho V D}{\mu}$$

(White 2008, 27)

The coefficient, D, refers to the characteristic length of the important linear dimension. It can refer to the length of a pipe, the diameter of a duct, the diameter of a cylinder, or the ratio of object dimensions, depending on the flow situation. (Munson, Young, and Okiiski 2006; White 2008)

Therefore, in order to ensure dynamic similarity between the model and the full-size prototype, the Reynolds number needs to be maintained across both. This means the relative size of the model (compared to the prototype) will dictate the required test velocities of the air flow in the wind tunnel.

The wind tunnel is 3m long, with cross section that 0.457m x 0.457m. Since the full size RSX fin is 0.660m long, a half scale model will both be numerically simple, and fit inside the tunnel. In this case, 'fitting' includes space for the fin to be mounted and 0.1m of free space, to allow for the boundary layers surrounding the fin and the against the wind tunnel wall, the thicknesses of which will be calculated in sections 4.1.3 and 4.1.4. Dynamic similarity means that the boundary layers will be the same size relative to the model and fin.

4.1.2 Required test speed range

The range of airspeeds required to maintain the dynamic similarity for the half scale model and the full scale RSX fin in an aquatic environment can be determined. As previously discussed in chapter 4.1.1, this can be done by maintaining the dimensionless parameter, the Reynolds number.

The values for the fluid properties were sourced from White (2008, 26), and have been included in the table below.

Table 7: Fluid properties for air and water

	M	P
Air	1.8 x 10^{-5} $kgm^{-1}s^{-1}$	1.20 kgm^{-3}
Water	1.0 x 10^{-6} $kgm^{-1}s^{-1}$	998 kgm^{-3}

$$\mathrm{Re}_{air} = \mathrm{Re}_{water}$$

$$\frac{\rho_{air} V_{air} D_{\mathrm{mod}el}}{\mu_{air}} = \frac{\rho_{water} V_{water} D_{prototype}}{\mu_{water}}$$

$$\frac{\left(1.20 kgm^{-3}\right)\left(\frac{1}{2} D_{prototype}\right)}{1.8x10^{-5} kgm^{-1}s^{-1}} V_{air} = \frac{\left(998 kgm^{-3}\right)\left(D_{prototype}\right)}{1.0x10^{-3} kgm^{-1}s^{-1}} V_{water}$$

$$V_{air} = 14.85 V_{water}$$

Since the RS:X is suitable for conditions ranging from 8 to 24 knots (4.12 to 12.3ms^{-1}), equivalent to 61.2 to 183 ms^{-1} for the model. (Gourlay and Martellotta 2011) An example calculation for the minimum value has been included below.

$$V_{\min\_air} = 14.85 V_{\min\_water}$$

$$V_{\min\_air} = 14.85 * (4.12 ms^{-1})$$

$$V_{\min\_air} = 61.2 ms^{-1}$$ (3 significant figures)

From the range of speeds suitable for testing, the lower limit is confined by the lowest realistic (equivalent) operating speed for the model, 61ms^{-1}, and the upper limit by the maximum speed possible in the wind tunnel, 30ms^{-1}. Since the minimum equivalent speed is greater than the wind tunnel maximum speed, the range of velocities over which the model was tested experimentally was from 22 to 30 ms^{-1}.

4.1.3 Boundary layer thickness: wind tunnel flow

The thickness of the boundary layer across the fin and wall surfaces can be estimated based on whether the flow is attached or turbulent.

The Reynolds number can provide an estimate of the flow behaviour. A table of typical flow behaviour for various Reynolds numbers has been included below. The values in this table were sourced from White (2008).

Table 8: Type of flow for various Reynolds numbers

Range of Reynolds numbers	Type of flow
$0 < Re < 1$	highly viscous, attached flow
$1 < Re < 100$	attached, strong Reynolds number dependence
$100 < Re < 10^3$	attached, boundary layer effect becomes significant
$10^3 < Re < 10^4$	transition to turbulence
$10^4 < Re < 10^6$	turbulent flow, with a moderate Reynolds number dependence
$10^6 < Re$	turbulent flow, with a slight Reynolds number dependence

The flow in the wind tunnel can be classed as either attached of turbulent by examining the Reynolds number of the flow within the tunnel.

$$\mathrm{Re} = \frac{\rho V D}{\mu}$$

(White 2008)

Where V is the velocity of the wind tunnel flow, D is the length of the tunnel to the cross-section of interest, the dynamic viscosity, μ, and the density, ρ, of the fluid.

The model will be fixed into position and tested 1m from the 'honeycomb' inside of the wind tunnel.

Therefore, the maximum and minimum Reynolds numbers of the wind tunnel at this location can be calculated as follows:

$$\mathrm{Re}_{\min} = \frac{22 * 1}{1.51 * 10^{-5}} = 1.5x10^6$$

$$\mathrm{Re}_{\max} = \frac{30*1}{1.51*10^{-5}} = 2.0x10^{6}$$

As shown in table 8, any flow with a Reynolds number of the order of 10^6 can be considered turbulent. The boundary layer on the wall surface can be compared to the boundary layer on a flat plate.

Since the flow inside the wind tunnel is known to be turbulent, the boundary layer thickness can be calculated.

4.1.4 Boundary layer thickness

There are multiple equations which exist to determine the width of a boundary layer, for both turbulent and attached flows.

Since it is known that the air flowing inside the wind tunnel is turbulent at the time it interacts with the model, the following equation, sourced from White (1999) was used.

$$\delta_{turb} = \frac{0.16x}{\mathrm{Re}^{1/7}}$$

(White 1999, 428)

Solving this gives:

$$\delta_{W\_turb\_\max} = \frac{0.16x}{\mathrm{Re}_{\min}^{1/7}}$$

$$\delta_{W\_turb\_\max} = \frac{0.16*1}{(1.5*10^{6})^{1/7}}$$

$$\delta_{W\_turb\_\max} = 0.0210m$$

Alternate calculations of the boundary layer thickness for turbulent flow give similar results.

Table 9: Boundary layer thickness for turbulent flow

	Boundary Layer Thickness (m, 3sf)	
	Turbulent Flow	
	Min Re	Max Re
Janna	0.0215	0.0203
White	0.0210	0.0201
Average	0.0213	0.0202

Hence, the maximum expected boundary layer thickness is 0.02m.

The suitability of a half scale model can now be confirmed. As the wind tunnel has a cross-section that 0.457m x 0.457m. The fin will be mounted horizontally inside the tunnel, therefore the maximum size the model can be is:

0.457m – 2(0.021m) = 0.415m

Since this is larger than the proposed model length of 0.330m, this size is suitable for the experiment.

4.1.5 The expected lift force acting on model inside the wind tunnel

The lift coefficient, C_L, is the dimensionless parameter relating the lift and dynamic forces as shown:

$$C_L = \frac{lift\_force}{dynamic\_force}$$

$$C_L = \frac{L}{\frac{1}{2}\rho U^2 A}$$

(White 2008, 493)

In the above equation, the lift force is denoted L, ρ represents the density of the fluid surrounding the foil, U represents the velocity of the fluid flowing across the surface of the foil, and A denotes the planform area of the fin. (Glenn Research Centre 2010c; White 2008)

For non-cambered foils, the lift coefficient has an approximate relation with the angle of attack, α, as shown below:

$$C_L = 2\pi * \sin\alpha$$

(White 2008, 557)

The above equation has been derived using the Kutta-Joukowski theorem, which relates the lift and circulation on a body. (Peter n.d.; White 2008) This implies that, where lift exists, the flow has a negative circulation. (Peter n.d.)

Thus, the lift coefficient can calculated for each angle of attack to be trialled.

Table 10: Lift coefficient for each angle of attack

Angle (degrees)	**Angle (radians)**	**lift coefficient (-)**
0	0	0
5	0.087266	0.547616
10	0.174533	1.091064
15	0.261799	1.626208
20	0.349066	2.148976
30	0.523599	3.141593

However, the overall lift coefficient is affected by the fin's finite span. This can be measured by using the ratio of the span of the fin to the average chord length, referred to as the dimensionless value known as the aspect ratio, AR. This is shown below:

$$AR = \frac{span}{average\_chord}$$

(White 2008, 496)

However, since the span is assumed to be wing span (of a plane), then the aspect ratio for the span of the fin becomes:

$$AR = \frac{2 * span}{average\_chord}$$

(Glenn Research Centre 2010d)

The planform area (area of a single side) of the fin model needs to be determined before either the aspect ratio or the maximum lift force on the fin model can be calculated.

The planform area was calculated by dividing the surface into a series of trapezoids using the coordinates of the extreme edges in the XY plane, as shown in the figure below.

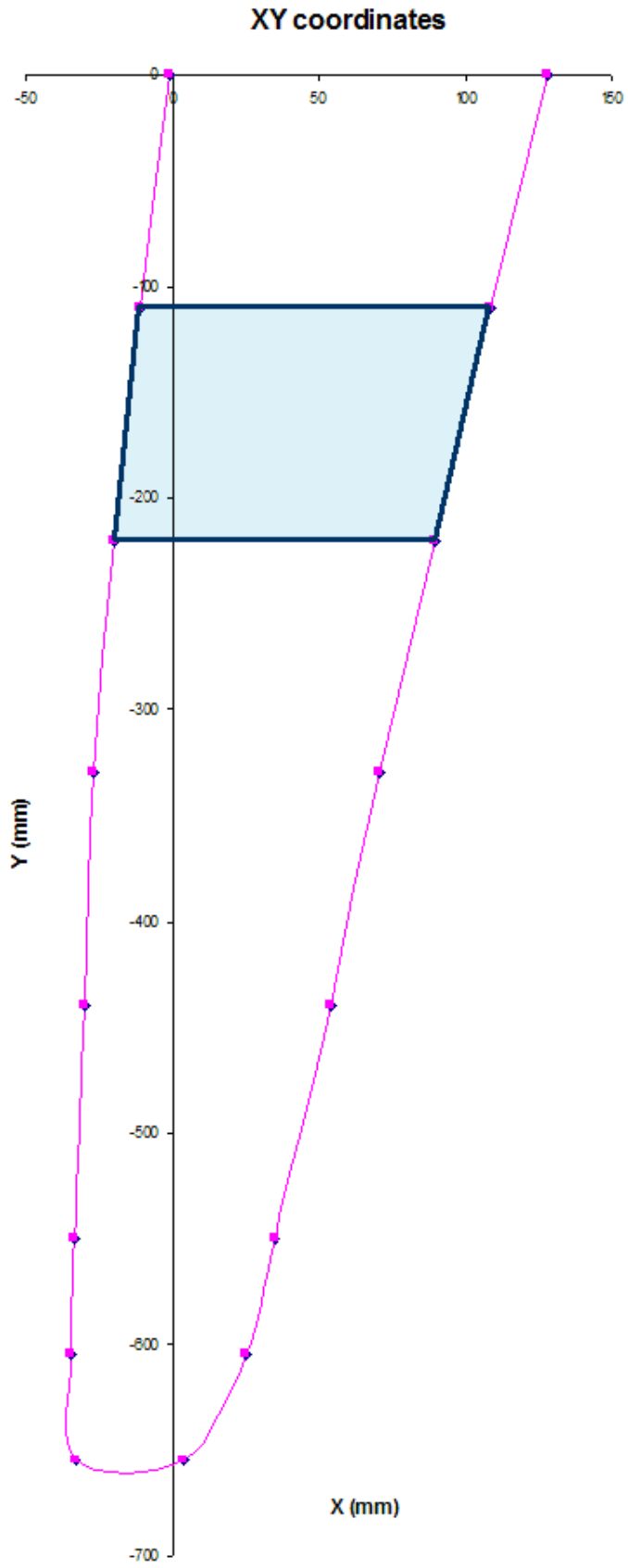

Figure 26: Leading edge of the fin with trapezoid using y-displacements bravo and charlie, and shown here using the excel model of the fin viewed in the XY plane, shown here on axes of unequal scale.

$$A_{trapezoid} = \frac{1}{2}(b_1 + b_2) * h$$

Summing the trapezoid made by each pair of y-displacements gives the planform area of the fin.

$$A_{total} = \sum A_{trapezoid}$$

$$A_{total} = 0.0622m^2$$

(3 significant figures)

Since the model is half the size of the prototype, the total area of the model is:

$$A_{model} = \frac{1}{4} A_{prototype}$$

$$A_{model} = \frac{1}{4} * 0.0622m^2$$

$$A_{model} = 0.0155m^2$$

(3 significant figures)

The trapezoidal method for determining the area of the fin can be considered equal to the average chord length multiplied by the span of the fin. Thus, dividing the total area of the model by the span of the fin gives the average chord of the fin, as shown below:

$$AV\_chord_{model} = \frac{area_{model}}{span_{model}}$$

$$AV\_chord = \frac{0.0155m^2}{0.3275m}$$

$$AV\_chord = 0.0268m$$

(3 significant figures)

Thus, the aspect ratio can be determined, as the span of the fin model is known to be 327.5mm. As this value is dimensionless, it should be constant for both the full sized fin, and the model.

$$AR = \frac{2 * 0.3275m}{0.0268m}$$

$$AR = 13.8$$

(3 significant figures)

This variable can then be used to determine the influence of the foil span on the overall lift coefficient, C_L, as shown below:

$$C_L = \frac{2\pi * \sin\left(\alpha + \frac{2h}{c}\right)}{1 + \frac{2}{AR}}$$

Where α is the angle of attack, h is the maximum camber and c is the chord length.

Since the foil is symmetric, and therefore non-cambered, this becomes:

$$C_L = \frac{2\pi * \sin(\alpha)}{1 + \frac{2}{AR}}$$

(White 2008, 497)

Thus, the lift coefficient can be determined for each angle of attack.

Table 11: Lift coefficient for infinite and finite foil spans

Angle (degrees)	**Angle (radians)**	**lift coefficient (-)**	**lift coefficient- finite span (-)**
0	0	0	0
5	0.09	0.548	0.478
10	0.17	1.091	0.953
15	0.26	1.626	1.420
20	0.35	2.149	1.877
30	0.52	3.142	2.744

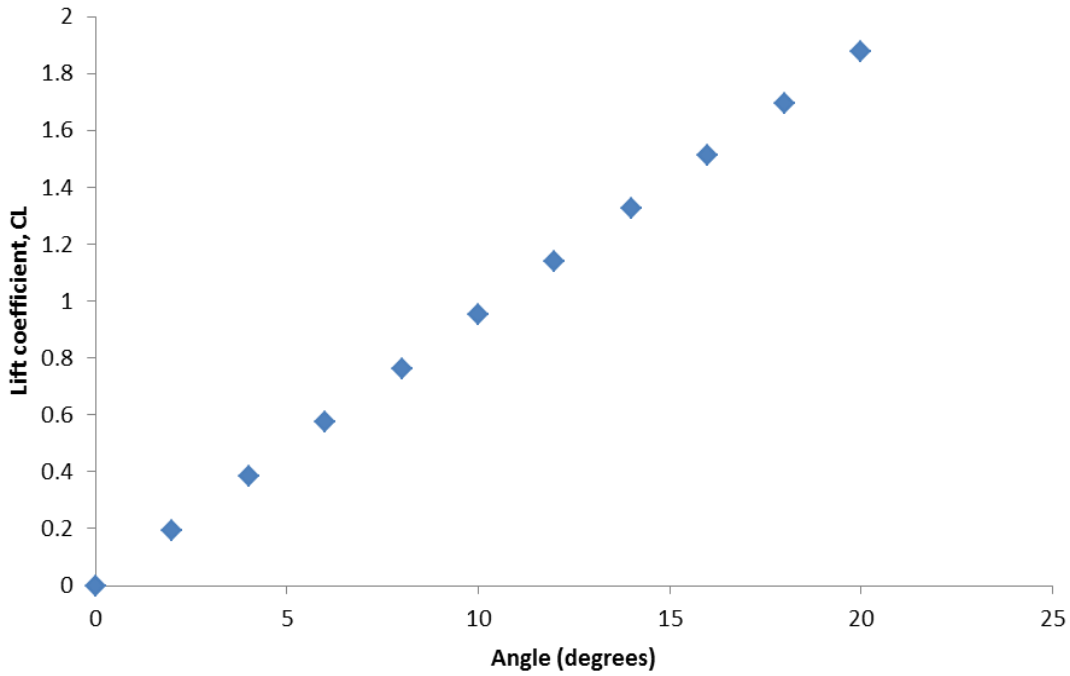

Figure 27: Lift coefficient for the fin, due to the finite span, shown for angles from 0-20°. It should be noted that the values for the lift coefficient shown above assume the flow has not yet separated.

Using the total planform area of the fin model, a maximum coefficient of lift for 20°, and assuming the maximum flow velocity encountered by the model is 30ms^{-1}, the maximum lift force on the model can be determined.

$$C_L = \frac{L}{\frac{1}{2}\rho U^2 A}$$

(White 2008, 493)

$$L = \tfrac{1}{2} C_L \rho U^2 A$$

$$L = \tfrac{1}{2}(1.88)(1.20 kgm^{-3})(30 ms^{-1})^2 (0.0155 m^2)$$

$$L = 15.8 N$$

(3 significant figures)

Hence, the maximum lift force on the fin will be 15.8N. However, this value neglects gravitational and drag forces.

It can be expected that this could cause the model to bend upwards from the root.

4.2. Rapid Prototyper

The rapid prototyper enables complex three dimensional models to be printed with great accuracy. The printer converts an AutoCAD STL file (other accepted formats include ZRML, PLY, 3DS and ZPR) into a physical model suitable for experimental validation and testing. There are several methods which can be used to produce the models, including:

- 3D Zcorp printing
- Polyjet printing
- Fused deposition modelling
- Stereolithography
- Selective laser sintering
- Computer numerical control

(Formero 2010; Rapid Pro 2011b; Z Corporation 2010)

The 3D Zcorp printing was the method chosen to produce the fin model for use in the wind tunnel (due to printer availability and intended purpose). Using this method, the three dimensional model was produced by 'printing' alternating thin layers (0.09-0.1mm) of plaster and a bonding agent. The finished model was then cleaned and impregnated with resin for strength. (Formero 2010; Rapid Pro 2011a; Z Corporation 2011)

Figure 28: 3D printer: ZPrinter 450.

4.3. Tell Tales

Tell tales are used to determine both the location and characteristics of any separation across the fin surface. They show whether the flow is attached (and attached) or separated, and the location of any reattachment.

As succinctly stated by Marchaj (1979), “The optimum position of the tell tales in relation to the leading edge should be such that they are capable of detecting reattachment somewhere between 5-15% of the sail chord.”

In light of this, tell tales were attached to the fin prior to performing the wind tunnel experiments. They were attached using sticky tape, to reduce the impact on the flow as much as possible.

The tell tales were attached along each y-displacement on the upstream side. The tell-tales only needed to be attached to one side of the foil, since it is non-cambered, and therefore lift is only produced when the foil is angled with respect to the flow. Along each XZ cross section, tuft was attached at 10%, 50% and 90% of the chord length.

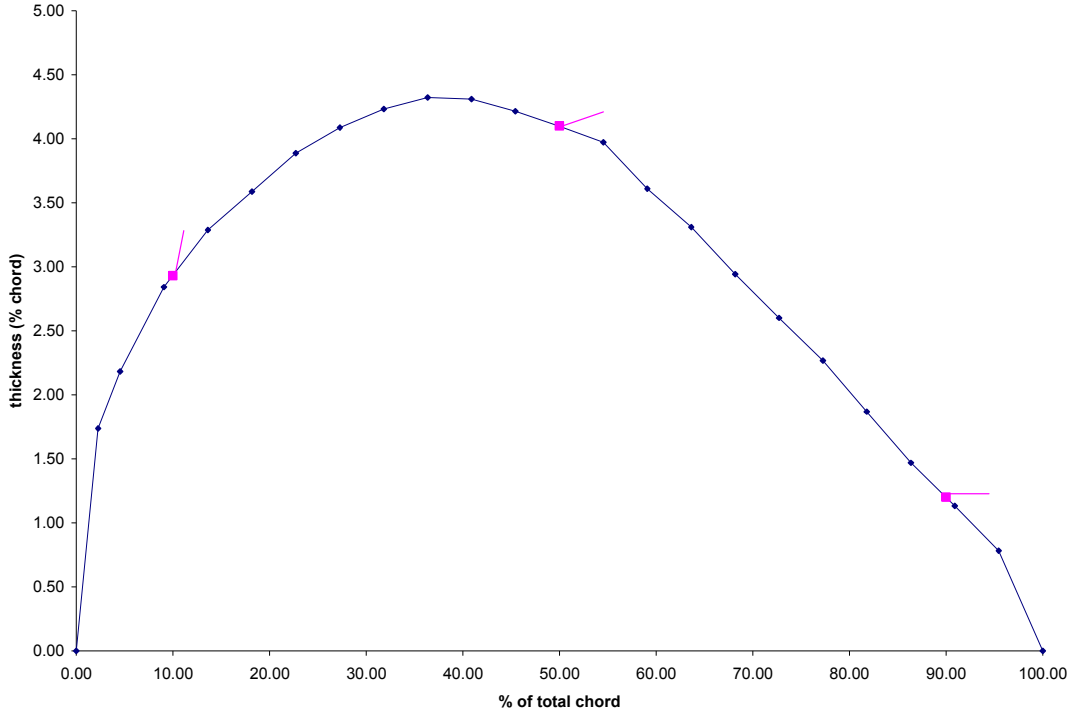

Figure 29: Proposed tuft attachment locations as a percentage of the total chord for each cross section.

4.4. Experimental procedure

4.4.1 Experimental set up

The fin with attached tell-tales was mounted horizontally into the wind tunnel, with an angle of 0^o towards the flow. The flow was allowed to develop, and the tell tale behaviour recorded. This will be repeated from 8^o to 16^o, increasing by 2^o each time.

The tell tales were attached at model y-displacements bravo, charlie, echo, and golf, at approximately 10%, 50% and 90% of the local chord. The tell tales were attached on one side of the fin only.

Figure 30: Model fin with tell tales attached at 10%, 50%, and 90% of the chord of model y-displacements bravo, charlie, echo and golf. (IMAG0146)

The wind tunnel was used on two separate occasions to record experimental data. The first occasion had the fin mounted using only a pair of metal blocks, as shown below:

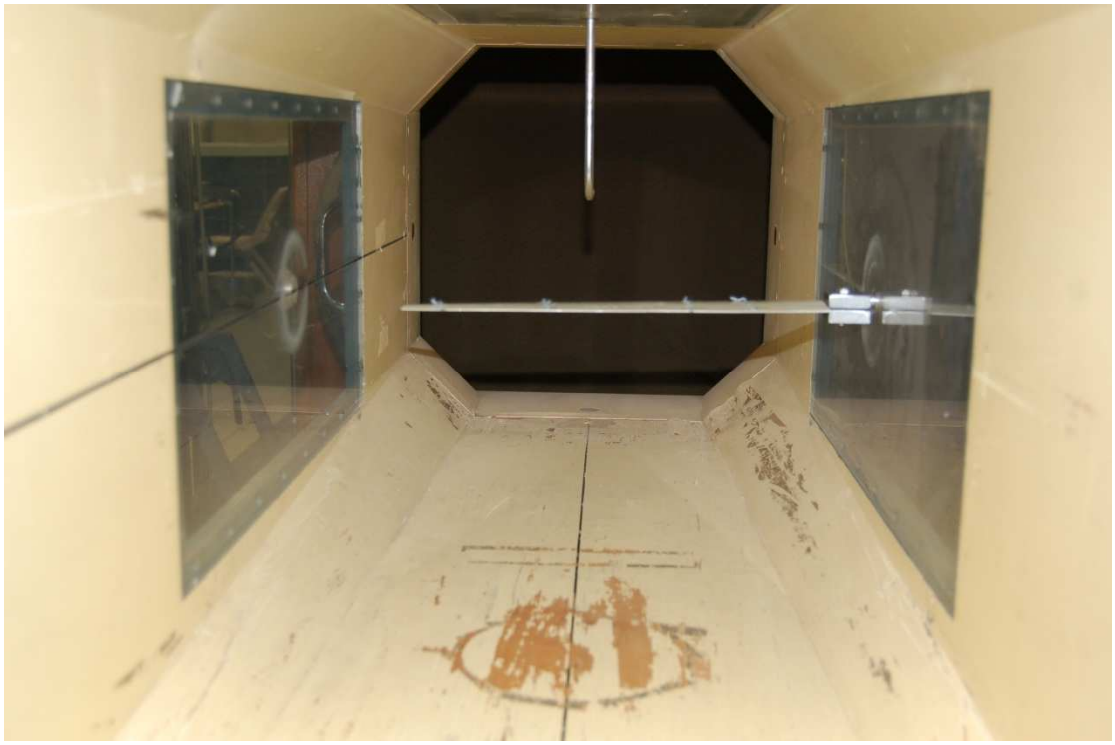

Figure 31: Model mounted between two blocks. (Photo #0083)

The second occasion had a steel plate, approximately 200mm x 200mm square, with a thickness of 1mm, to prevent flow recirculation behind the blocks from impacting on the flow at y-displacement alpha, as was noted during the first set of experiments. For this reason the report will have a focus on the results recorded from the second set of experiments.

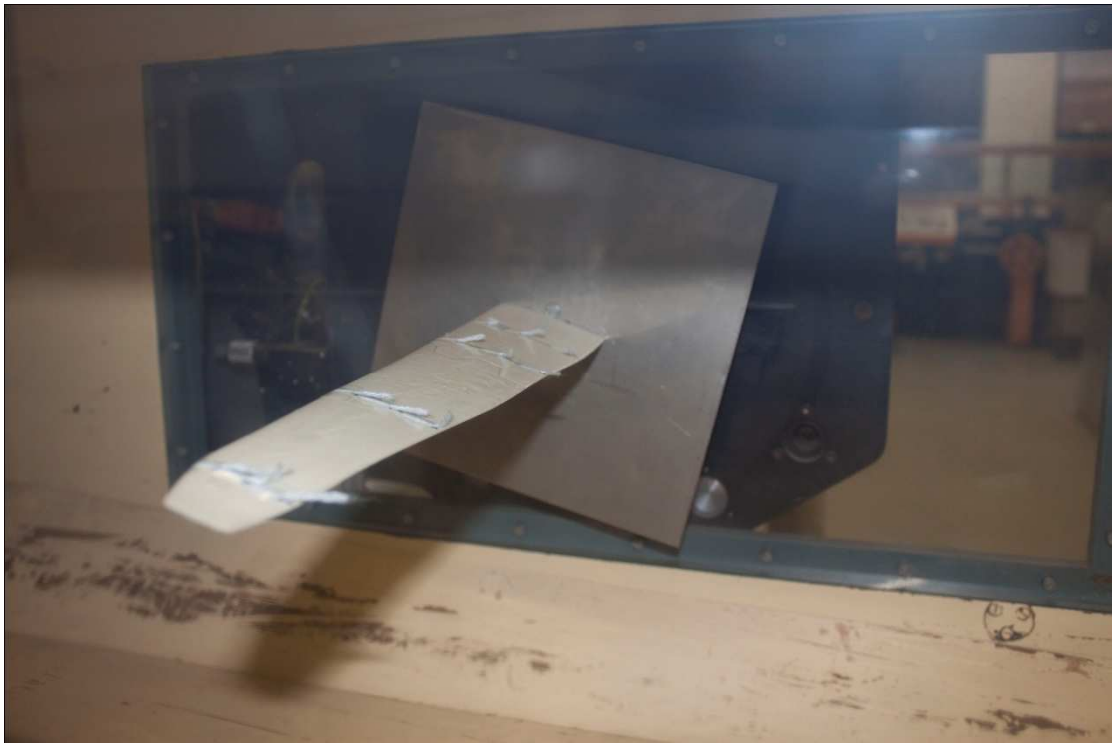

Figure 32: Model mounted with steel plate to prevent recirculation. (Photo #8378)

The fin was mounted into the wind tunnel with an initial angle of attack of 0^o to the flow. The Pitot tube ahead of the model was attached to a manometer to determine the air speed inside the wind tunnel.

The Pitot tube measures the air pressure of the free flow upstream of the fin model (the static pressure), and compares it to the stagnation pressure, the pressure of the fluid after it has been slowed to zero velocity.

The Pitot tube, as shown in the diagram below, is created from a pair of concentric tubes, one inside the other.

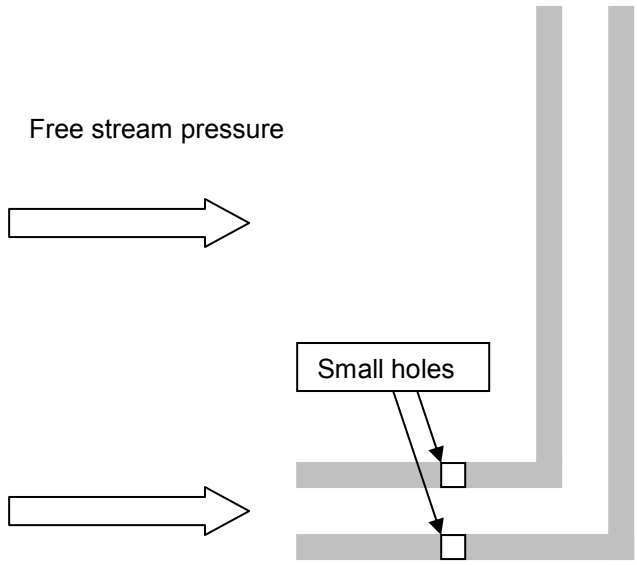

Figure 33: Diagram of a Pitot tube.

The hole in the front of the central tube- aligned such that it is facing into the flow, measures the stagnation pressure of the flow, p_0, as it is forced to zero velocity. The small holes in the sides of the outer tube allow measurement of the static pressure, p_s, the pressure of the moving flow relative to itself. This pressure difference is measured by a device known as a manometer. (Munson, Young, and Okiiski 2006; White 2008)

An initial manometer reading was recorded, prior to turning on the wind tunnel, as a measurement of 0 velocity.

The wind tunnel was then turned on and the intake opened until approximately half open.

The pressure difference in the tunnel was recorded using the manometer. For this single pressure difference, and hence a consistent air speed, the model was turned

through a range of angles with respect to the flow. For each angle, several photographs were taken of the tell tale behaviour, from various angles through the wind tunnel Perspex windows.

The original wind tunnel trials recorded the flow behaviour for the following angles of attack: 0^{o}, 5^{o}, 10^{o}, 12^{o}, 14^{o}, 16^{o}, 18^{o}, 20^{o}. These angles were chosen since a narrow range of angles was expected, based on NACA 6-series behaviour. Preliminary tests confirmed this, and suggested that the flow was likely to stall at approximately 10^{o}.

It was originally planned that the flow about the fin model would be tested for the speeds ranging from $22ms^{-1}$ - $30ms^{-1}$, and increasing by $2ms^{-1}$, but since an analogue manometer was used, as shown below, approximate velocities were used.

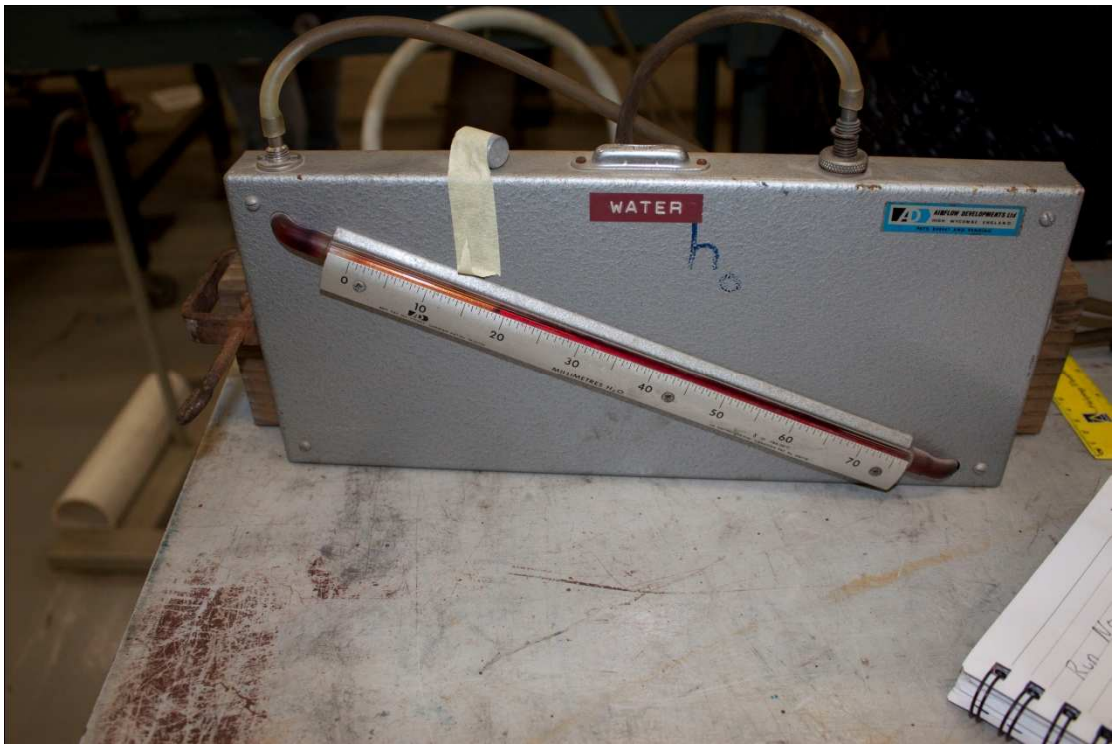

Figure 34: Manometer used to show the pressure difference measured by the Pitot tube.

Since the manometer readings were variable, the measurements were based on the average reading, and the uncertainty on the standard deviation.

$$z = \frac{z_{\max} - z_{\min}}{2}$$

After the experiment was performed, the height shown by the manometer was converted to a measurement of velocity using Bernoulli's equation, as shown below:

$$P_f + \frac{1}{2}\rho_{air} v_f^2 + \gamma h_f = P_0 + \frac{1}{2}\rho_{air} v_0^2 + \gamma h_0$$

(Munson, Young, and Okiiski 2006; White 2008; *Bernoulli's Equation* 1997; Engineering ToolBox 2011)

Where the left hand side refers to the free flow upstream of the fin, and the right hand side refers to the stagnation point of the flow. Since the h_f is equal to h_0, and the stagnation point has a velocity of 0ms^{-1} this simplifies to:

$$P_f + \frac{1}{2}\rho_{air} v_f^2 = P_0$$

Rearranging this equation allows the velocity of the free stream, v_f, to be determined:

$$v_f = \sqrt{\frac{2(P_f - P_0)}{\rho_{air}}}$$

Since the pressure was measured as the change in height of water inside the manometer, the hydrostatic formula can be substituted for the pressure difference.

$$P_2 - P_1 = -\rho_{water} g(z_2 - z_1)$$

(White 2008)

Thus,

$$v_f = \sqrt{\frac{-2\rho_{water} g(z_0 - z_f)}{\rho_{air}}}$$

Rearranging gives:

$$v_f = \sqrt{\frac{2\rho_{water} g(z_f - z_0)}{\rho_{air}}}$$

The pressure difference measured by the Pitot tube is measured as the change in height between the flow speed, z_f, and the height at atmospheric pressure, z_0.

$$\Delta z = z_f - z_0$$

This height difference must be then converted such that it is measured in metres. Following this, the height difference can be substituted into the equation for the free stream velocity:

$$v_f = \sqrt{\frac{2\rho_{water} g * \Delta z}{\rho_{air}}}$$

The uncertainty of the free stream velocity was calculated as follows:

$$v_{f\_uncertain.ty} = v_f * \frac{z\_uncertai.nty}{\Delta z}$$

Table 12: Manometer readings wind tunnel experiment 1

Set No	Manometer Reading (mm)	Change in elevation, Δz (m)	Air speed (ms^{-1})
0ms^{-1}	2.5 ± 0.5	-	-
Set 1	17 ± 1	0.015 ± 0.001	15.4 ± 1.06
Set 2	30 ± 1.4	0.028 ± 0.001	21.2 ± 1.09
Set 3	48 ± 1.4	0.046 ± 0.001	27.3 ± 0.84

Table 13: Manometer readings wind tunnel experiment 2

Set No	Manometer Reading (mm)	Change in elevation, Δz (m)	Air speed (ms^{-1})
0ms^{-1}	5.5 ± 0.5	-	-
Set 1	18.5 ± 1	0.013 ± 0.001	14.6 ± 1.12
Set 2	32.25 ± 3	0.027 ± 0.003	20.9 ± 2.49

For each pressure reading made in the first set of wind tunnel experiments, the following angles of attack were tested: 0^o, 5^o, 10^o, 12^o, 14^o, 16^o, 18^o and 20^o. For each pressure reading made in the second set of wind tunnel experiments, the following angles of attack were tested: 0^o, 8^o, 10^o, 12^o, 14^o, and 16^o.

4.4.2 Experimental results

The behaviour of the tell tales will be discussed in terms of the y-displacement (bravo, charlie, echo and golf) and then the position relative to the leading edge of the fin model (1, 2 and 3 as 10%, 50% and 90% respectively).

The second set of wind tunnel experiments using the steel plate have been included below.

The first velocity tested with the steel plate was 14.6 ms^{-1}.

Figure 35: Fin model oriented at 10^{o} to the flow, with wind speed of 14.6 ms^{-1}. (Photo #8313)

When the model had an angle of attack of 10^{o} to the air flowing at 14.6 ms^{-1}, the tell tales showed mostly attached flow over the fin, with separation beginning to occur at towards the trailing edge, at tell tales b2, b3, c2, c3 and e3. This suggests that the region of separation moves down along the fin from the 'root', towards the free tip.

Figure 36: Fin model oriented at 12^{o} to the flow, with wind speed of 14.6 ms^{-1}. (Photo #8318)

When the model had an angle of attack of 12^{o} to the incoming air stream of 14.6 ms^{-1}, the tell tales showed separation towards the rear of the model, at tell-tales b3,c3, e3 and g3, as shown in the above figure.

Figure 37: Fin model oriented at 14^{o} to the flow, with wind speed of 14.6 ms^{-1}. (Photo #8321)

When the angle of attack is increased to 14^{o}, the flow separation occurs at/just after the leading edge of the fin for cross-sections bravo, charlie and golf. Cross section echo is only showing separation at the trailing edge.

Figure 38: Fin model oriented at 16^{o} to the flow, with wind speed of 14.6 ms^{-1}. (Photo #8338)

When the angle of attack is increased again, the flow is fully separated.

The fin model was then 'reset' to a 0^{o} angle of attack, and the air speed inside the tunnel increased to 20.9 ms^{-1}.

Figure 39: Fin model oriented at 8^{o} to the flow, with wind speed of 20.9 ms^{-1}. (Photo #8361)

When the model of the RSX fin is at an angle of attack of 8^{o} to 20.9 ms^{-1} wind, the flow across the foil surface is completely attached, as shown by the above figure.

Figure 40: Fin model oriented at 10^{o} to the flow, with wind speed of 20.9 ms^{-1}. (Photo #8352)

For the fin oriented at 10^{o}, then the flow separation occurs somewhere between 10-50% of the chord length, for cross sections bravo and charlie, and towards the trailing edge of cross section echo.

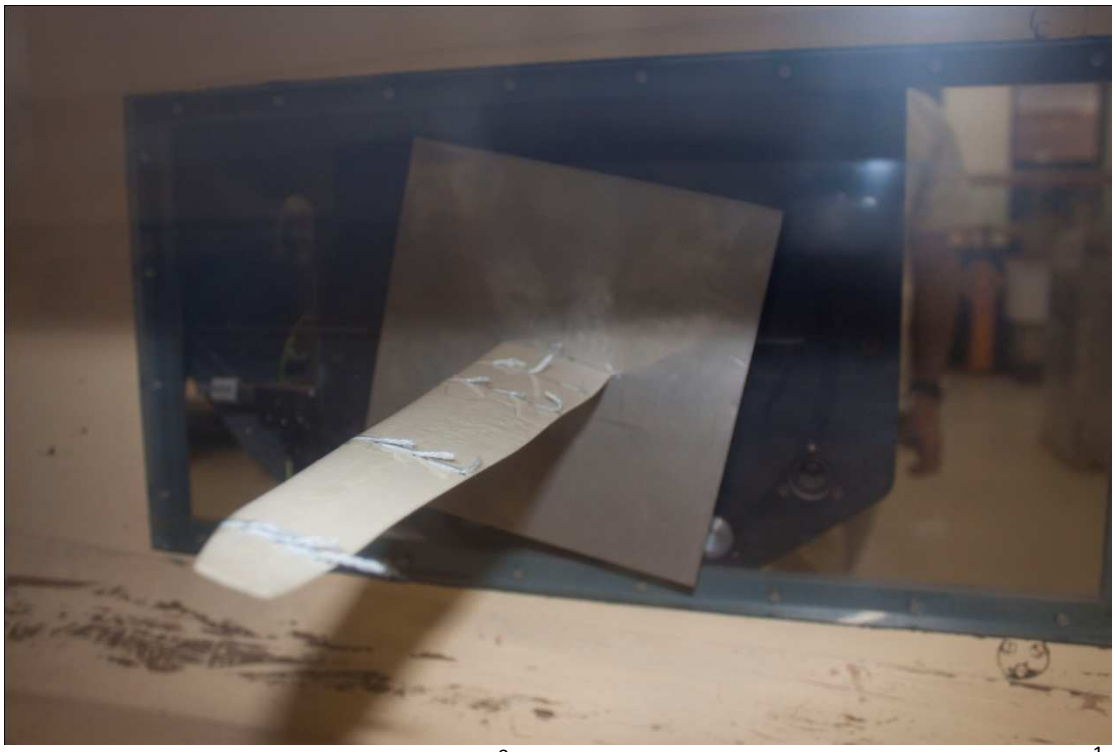

Figure 41: Fin model oriented at 12^{o} to the flow, with wind speed of 20.9 ms^{-1}. (Photo #8369)

When the foil model is oriented at 12^{o} towards the incoming 20.9 ms^{-1} fluid, separation occurs at the leading edge of cross sections bravo and charlie, and towards the trailing edges of echo and golf.

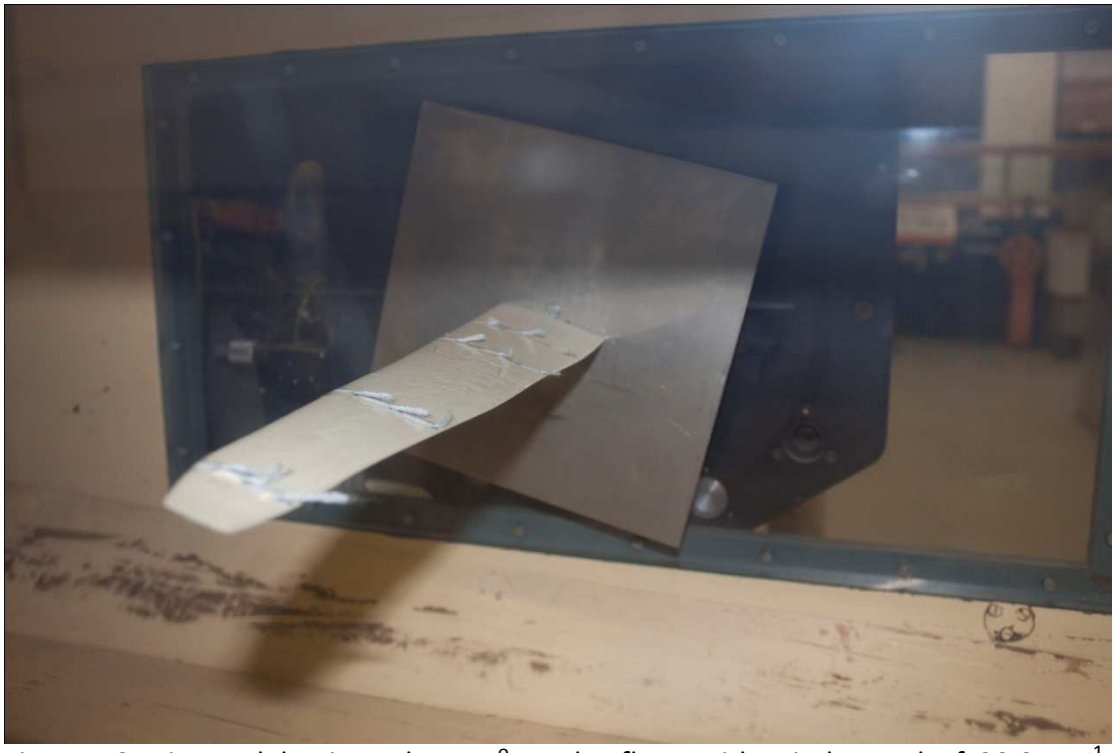

Figure 42: Fin model oriented at 14^{o} to the flow, with wind speed of 20.9 ms^{-1}. (Photo #8378)

At an angle of attack of 14^{o}, the flow is separating at the leading edge of cross sections bravo and charlie, and at 10-50% of chord of cross sections golf and echo.

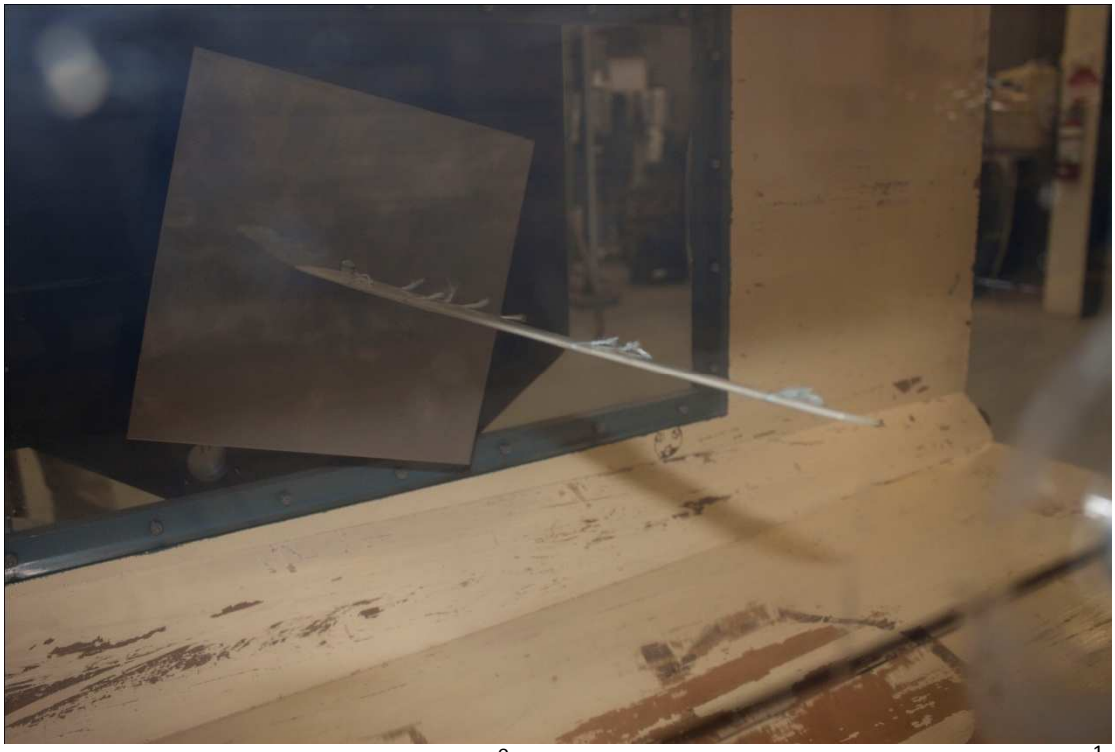

Figure 43: Fin model oriented at 16^{o} to the flow, with wind speed of 20.9 ms^{-1}. (Photo #8387)

At 16^{o}, the flow separates at the leading edge of all cross sections, and is hence fully stalled.

It should be noted that a cross flow is clearly present flowing across the upper surface of the fin directed away from the tip. It can be seen in the consistent angling of the tell tales away from the fin tip. It is strongest at the tip, as the tell tales along cross section golf are consistently directed towards the root of the fin.

This makes sense from a theoretical perspective, since the upper edge of the fin, also referred to as the root, is 'closed' to circular flow around the edge of the fin, due to the steel plate, the flow is swept up only about the tip of the fin. This means that trailing edge vortices are only produced from the tip of the fin, and there exists a planar component to the motion of the fluid across the upper and lower surfaces of the fin. The upper surface of the fin will experience a cross-flow in the direction from the tip towards the root, and the lower surface will experience a cross flow in the opposite direction, towards the tip.

The key conclusions to be drawn from the experimental data are as follows:

- Flow separation starts at the 'root' of the foil, and progresses along the length of the fin as the angle of attack is increased.
- Alternatively, flow separation can occur at the root and tip of the foil, and then progress towards the centre of the fin.
- Moves forward from the trailing edge towards the leading edge.
- Separation along the foil initiates at approximately 10^{o}, and is the foil is fully stalled by 16^{o}.
- Close to the model tip, there is a significant level of cross flow on the upper surface directed towards the root.

It should be noted that, due to practical considerations, the pressure and lift on the surface of the model was unable to be measured, and therefore were unable to be compared with the computational analysis.

4.4.3 Application of experimental results to full-scale model

The air speeds interacting with the model inside the wind tunnel can be compared to speed of water flowing past the full sized fin using the Reynolds number relationship, as discussed in section 4.1.1.

Thus, the air speeds tested are dynamically similar to the following water speeds with respect to the fin. They can be related using the following equation, as determined in chapter 4.1.2.

$$V_{air} = 14.64 V_{water}$$

Thus,

$$V_{water} = 0.0683 V_{air}$$

From this, the air speeds tested in the wind tunnel can be compared to the water speeds likely to be encountered by a full size fin, as shown in the table below.

Table 14: Equivalent speeds to air speeds tested

Experiment	Set No	Air speed, model (ms^{-1})	Water speed, fin (ms^{-1})
1	Set 1	15.4 ± 1.06	1.05 ± 0.07
1	Set 2	21.2 ± 1.09	1.45 ± 0.07
1	Set 3	27.3 ± 0.84	1.86 ± 0.06
2	Set 1	14.6 ± 1.12	0.99 ± 0.08
2	Set 2	20.9 ± 2.49	1.43 ± 0.17

Since the operating speeds for the fin range from 61.2 ms^{-1} to 183 ms^{-1}, as discussed in section 4.1.2, the wind speeds tested for all experiments excepting Experiment 1, Set 3, are actually outside (below) this range. Despite this, the Reynolds numbers of the wind tunnel flow have the same order of magnitude as the practical situation, and can therefore be considered equivalent.

This means that the model and full sized fin are dynamically similar, as the Reynolds numbers of the flow situations tested are equivalent to the minimum Reynolds number of the flow situations in which an RSX foil is typically used.

Despite this, the maximum flow speed which the wind tunnel is capable of is still only in the lower use range of the RSX fin. Where the board is planing upwind at less than 8 knots (4.12ms^{1}), the fin is used in conjunction with the centreboard, and thus neither the computational nor the experimental analysis is suitable for this situation.

Additionally, since this report is focussed on the flow about the fin in racing conditions, it should be noted that the wind tunnel was not capable of the extremely high speeds required to simulate racing speeds. Despite this, the Reynolds numbers

of the flows tested experimentally are still of the same order of magnitude as a flow likely to be encountered at racing speeds. Thus, these experiments have provided clear insight into the way in which the fluid moves around the foil, and this can be applied to both low and high speed usage of the RS:X board.

5. Computational Analysis

The computational analysis of the flow around the RS: X Racing 66 windsurfing fin was conducted using OpenFOAM, an open source (and therefore readily attainable) fluid dynamics software. The purpose of the computational analysis was to examine the expected flow around the fin at various angles of attack, and for comparison with the experimental results from the wind tunnel, and the expected results for a NACA 65-009 section. The change in flow with time can also be analysed (i.e. start up, and separation), as can three dimensional effects such as tip vortices.

5.1. XFOIL

XFOIL is a program created by Drela and Youngren with the intent of assisting a user with the design and analysis of subsonic aerofoils for different types of flows and different angles of attack. (Drela and Youngren 2001a, 2001b; Matyushev 2009)

The program was written in Fortran, and is available in 32-bit versions only for Windows, Mac and Linux operating systems. (Matyushev 2009)

The software is capable of flow analysis for both viscous and inviscid flow, and in the case of the former, is capable of not only identifying the existence of a boundary layer, but also the location of laminar-turbulent transition. (Drela and Youngren 2001b)

XFOIL was used to determine the location of the boundary layer transition from laminar to turbulent boundary layer flow, with respect to the chord length. If the boundary layer is primarily laminar, the computational analysis should be conducted using laminar flow, and if it is turbulent, it should be conducted with a suitable turbulence model.

5.1.1 Boundary layer analysis using XFOIL

As in section 3.1.1, the profile measured across y-displacement charlie was used as the 'characteristic' profile for the RS: X 66cm windsurfing fin.

As noted by Martellotta (2010), and mentioned in chapter 3.3, the accuracy and precision with which a leading edge radius of a foil is specified is crucial for the program to be able to model the fluid flow appropriately, without the program modelling an unrealistic leading edge separation. Thus, to this end, the profile loaded into XFOIL had the leading edge specified every 0.1 radians ($\approx 5^{o}$).

XFOIL determines the pressure distribution and boundary layer about a foil based on the foil profile, the angle of attack, and the dimensionless flow characteristics of the Reynolds number and the Mach number.

5.1.2 Reynolds and Mach numbers of the wind tunnel flow

The Reynolds number used the analysis in XFOIL was the minimum calculated Reynolds number at the foil position, 1.5 x 10^6, for the minimum flow speed of 22ms^{-1}, as calculated in chapter 4.1.2.

The Reynolds number is without doubt the most well-known dimensionless parameter in fluid mechanics, due to its relevance to almost all fluid dynamics problems. (Munson, Young, and Okiiski 2006; White 2008)

Several other dimensionless parameters also exist, with each characterising the relationship between a different pair of forces, and hence have uses in varying applications of fluid mechanics. The Mach number, Ma, is another dimensionless variable used to describe flow behaviour. It is used when characterising flows "in which the compressibility of the fluid is important." (Munson, Young, and Okiiski 2006, 362)

The Mach number is the ratio of the inertia force to the compressibility force, and is thus dependent on the velocity of the fluid, V, relative to the speed of the sound within the medium, c, as shown below.

$$Ma = \frac{inertia\_force}{compressibility\_force}$$

$$Ma = \frac{V}{c}$$

(Munson, Young, and Okiiski 2006)

Since the model will be tested inside the Curtin wind tunnel, the Mach number for flow inside the wind tunnel is required to accurately simulate this flow using XFOIL.

The speed of sound in air (at 20^o C and standard atmospheric pressure) is 343ms^{-1}, according to Serway and Jewett (2004, 514). This value was used to determine the Mach number for the maximum and minimum wind tunnel test speeds. The model was tested under speeds ranging from 22-30ms^{-1}.

Thus, the maximum Mach number was calculated as follows:

$$M_{air\_\min} = \frac{V_{air\_\min}}{c_{air}}$$

$$M_{air\_\min} = \frac{22ms^{-1}}{343ms^{-1}}$$

$$M_{air\_\min} = 0.0641$$

(3 significant figures)

Likewise, the maximum Mach number was calculated as follows:

$$M_{air\_\max} = \frac{V_{air\_\max}}{c_{air}}$$

$$M_{air\_\max} = \frac{30ms^{-1}}{343ms^{-1}}$$

$$M_{air\_\max} = 0.0875$$

(3 significant figures)

Thus, the average Mach number is:

$$M_{airav} = \frac{M_{air\_\max} + M_{air\_\min}}{2}$$

$$M_{airav} = \frac{0.0875 + 0.0641}{2}$$

$$M_{airav} = 0.0758$$

(3 significant figures)

This value was used for the analysis of the boundary layer in XFOIL.

5.1.3 Boundary layer and pressure distribution

The flow around the cross-section denoted ‘charlie’ was analysed for various angles, for the following values of the Reynolds and Mach numbers, as determined in the previous section:

Reynolds number = 1.5e6
Mach number = 0.076

In addition to this, 100 iterations were used per set of the boundary layer analysis.

The pressure distribution about the foil when it is oriented parallel to the flow is quite flat, excepting a peak just past the leading edge, which is similar to the pressure distribution expected for a NACA 65-009, as discussed in section 2.2.4.

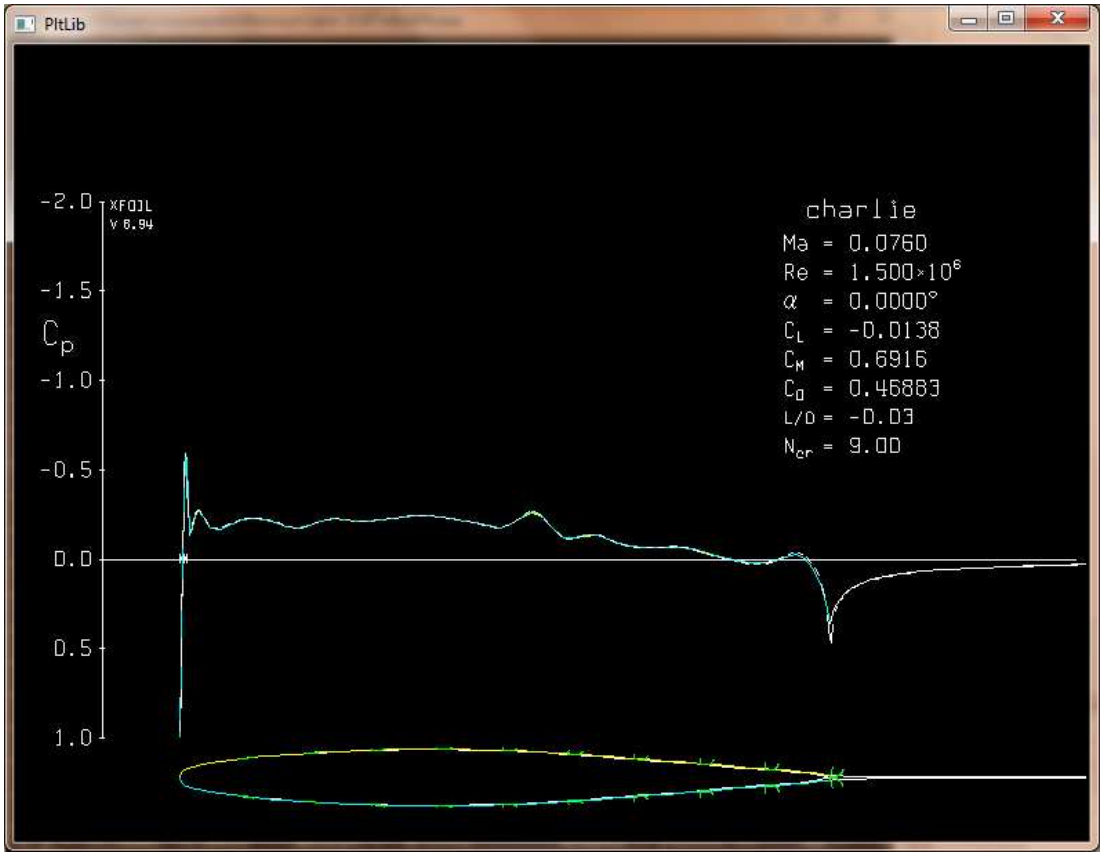

Figure 44: The boundary layer and distribution of pressure for foil cross-section charlie, determined from a Reynolds number of 1.5×10^6 and a Mach number of 0.076, when the foil is oriented parallel to the flow.

As discussed in section 2.1.1, the boundary layer transition can be seen to have occurred where the boundary layer becomes thicker. XFOIL determines the location of transition in the boundary layer with each calculation of the pressure coefficient, Cp.

The table below includes the location of boundary layer transition on each side of the foil for each angle of attack tested.

Table 15: Location of boundary layer transition on the RSX characteristic cross-section as calculated by XFOIL for various angles of attack

Angle	Number of iterations/set	Number of sets	Convergence reached	Transition (% chord)	
(degrees)			(y/n)	side 1	side 2
0	100	1	y	1.29	1.29
5	100	2	y	0.99	23.44
10	100	3	y	0.78	55.53
12	100	1	y	0.73	57.71
14	100	2	y	0.72	58.59
16	100	1	y	0.72	58.84
18	100	1	y	0.72	59.13
20	100	1	y	0.71	60.42

The boundary layer transition occurred earlier on the fin surface than expected for all angles of attack tested.

The locations of boundary layer transition for the RSX can be compared to the locations of boundary layer transition for the NACA 65-009. The values and corresponding graph have been included below.

Table 16: Location of boundary layer transition on the NACA 65-009 as calculated by XFOIL for various angles of attack

Angle	Number of iterations/set	Number of sets	Convergence reached	Transition (% chord)	
(degrees)			(y/n)	side 1	side 2
0	100	1	y	4.28	4.31
5	100	2	y	0.65	33.23
10	100	2	y	0.06	56.66
12	100	1	y	0.06	63.48
14	100	1	y	0.06	68.45
16	100	1	y	0.06	71.82
18	100	1	y	0.06	76.55
20	100	3	n	-	-

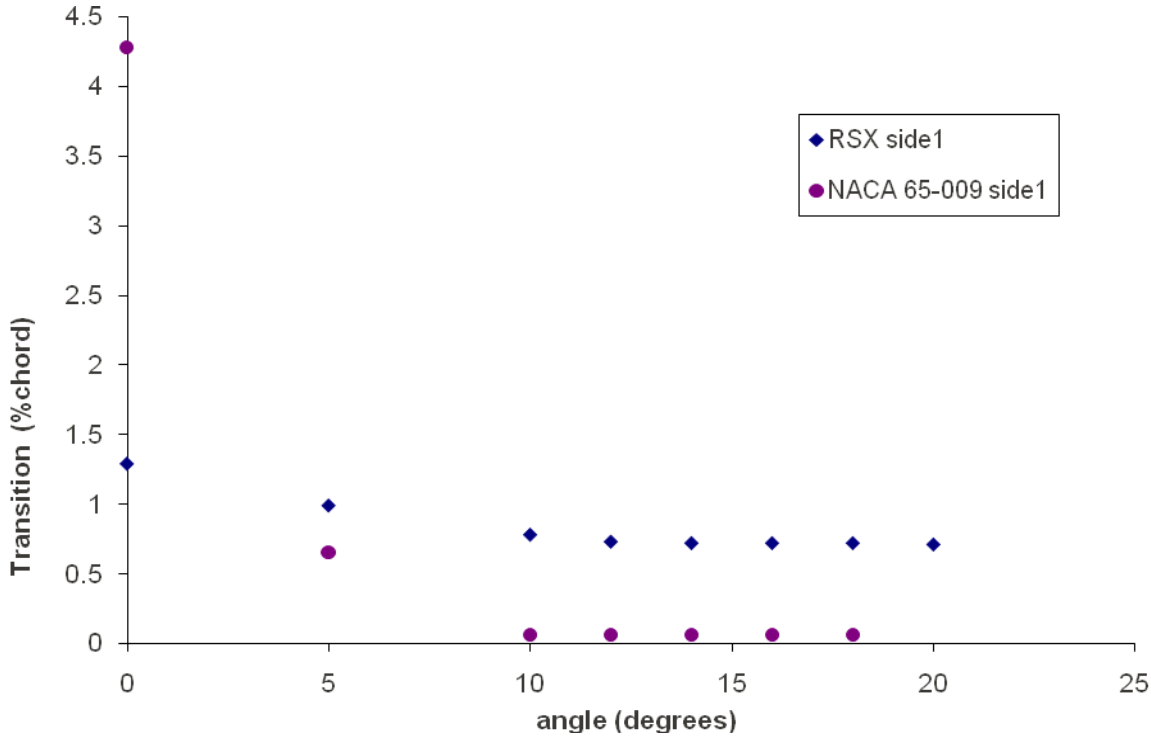

Figure 45: The location of boundary layer transition (side 1) for the RSX and NACA 65-009 foils.

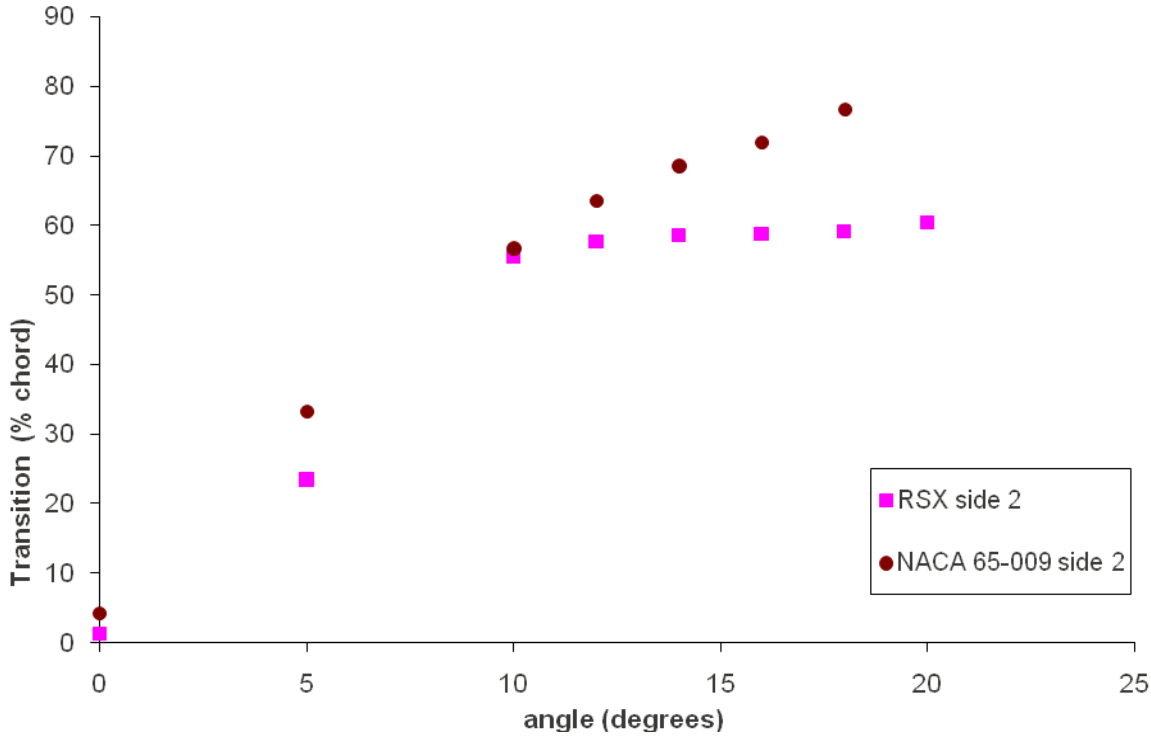

Figure 46: The location of boundary layer transition (side 2) for the RSX and NACA 65-009 foils.

The location of boundary layer transition is consistently earlier for the leeward side, side 2, on the RSX than on the 65-009 foil, but consistently later on the windward side, side 1. Despite this, the boundary layer transition plots are relatively similar in shape, which was expected due to the similarity of the RSX and NACA 65-009 foils.

For low angles of attack, the RSX shows an early transition to turbulent boundary layer flow, although this decreases as the angle of attack increases. For angles between 10^{o} and 20^{o}, the transition point on the leeward side shifts back to 50-60%, and can therefore be considered approximately equally dominated by laminar and turbulent flow. However, the experimental testing in discussed chapter 4 suggests that the RSX fin will be stalled by approximately 14^{o}, suggesting that for this range of angles, the flow is dominated by turbulence.

Thus, the boundary layer of the RSX fin typically has a an early transition to turbulent flow, suggesting that the computational analysis will be more realistic if conducted using a turbulent flow model.

5.2. OpenFOAM

The name OpenFOAM stands for 'Open Field Operation And Manipulation' and the program is a free, open source computational fluid dynamics software, suitable for solving problems in fluid dynamics involving turbulence, heat transfer or chemical reactions, solid dynamics and electrodynamics.

As stated by the OpenFOAM website, "OpenFOAM uses finite volume numerics to solve systems of partial differential equations ascribed on any 3D unstructured mesh of polyhedral cells. The fluid flow solvers are developed within a robust, implicit, pressure-velocity, iterative solution framework, although alternative techniques are applied to other continuum mechanics solvers." (OpenFOAM 2011a)

The use of OpenFOAM can be characterised into three distinct components:
-pre-processing
-processing
-post-processing (OpenFOAM 2011a)

Pre-processing involves setting up the system to be modelled, which in this case refers to creating the mesh representing the fin, and mesh of the fluid surrounding it, and setting up the initial constraints on the system. These initial constraints refer to the fluid pressure, velocity, angle of attack etc. (OpenFOAM 2011a, 2011c)

ParaView is the associated software for viewing the fluid flow problems (post-processing). It includes a graphic user interface which allows for interactive manipulation of the fluid. It enables the effect of time on a problem to be examined. (OpenFOAM 2011a, 2011b)

In the context of this report, post-processing involves examining the streamlines showing the pressure and velocity distribution of the fluid as it flows past the foil.

5.3. Computational procedure

5.2.1 Pre-processing

The fin was modelled using the snappy hex mesh function, using the surface STL file generated from AutoCAD. The fluid surrounding the fin was modelled using the block mesh function, dividing the region surrounding the foil into several areas to ensure the behaviour towards the leading edge was correctly, and clearly, modelled. The block mesh of the fluid surrounding the foil was then graded such that it will be finer in the region near the foil, and less fine towards the mesh boundaries. This improves the computational efficiency. Grading the mesh also ensures that the fluid behaviour is modelled clearly in the region of interest: close to the fin, but at the expense of being less accurate towards the outer limits of the modelled area.

The mesh was produced such that it would be the same size (relative to the fin) as the wind tunnel is to the model. That is, double the dimensions of the actual tunnel, and the full size fin is twice the size of the model. Thus the dimensions used for the computational tunnel were 3m x 0.914m x 0.914m.

The flow conditions had to be specified including the fluid pressure, velocity, and whether the fluid is attached or turbulent, etc.

The fluid was assumed to be water, allowing the velocities tested to be directly equivalent to the velocities encountered by the full scale model.

The no slip condition was conserved at the foil surface, thus invoking the boundary layer requirement. Since the foil boundary layer, and hence the flow across the foil surface is primarily turbulent (see chapter 5.1.3), the flow was modelled as turbulent. To this end, the flow was modelled using the SpalartAllmaras turbulence model.

Spalart Allmaras is a classical turbulence model. It is a time averaged Reynolds Averaged Navier Stokes (RANS) single equation model. Turbulence models allow the calculation of mean flow, without first needing the complete time dependent flow field. The Spalart Allmaras model is primarily used for aerodynamics problems, given that is reasonably efficient and accurate for flows with mild separation. (Bakker 2005; Javaherchi 2010)

5.2.2 Processing

After flow conditions were specified, the program was run by first defining the meshes, then using the 'preparation' turbulence model: potentialFoam, followed by the turbulent model: simpleFoam. (OpenFOAMWiki 2009)

The models were run for 500 seconds, after which time it was expected that the flow was likely to have converged.

5.2.3 Post-processing

After the flow models have been processed, the model can be opened using the visualisation software, ParaView, as mentioned above.

Running the models with time shows that they typically converged at 3seconds, meaning that results produced at time 500 should be steady-state.

For each of these models, streamlines were produced that flowed past various y-displacements along the foils corresponding with the measured cross-sections. This will be discussed in the following section.

5.4. Computational results

Velocity and pressure streamlines were produced about cross sections charlie, echo and hotel for each velocity tested, at 10^{o}, 12^{o} and 14^{o} with respect to the flow.

5.3.1 Comparison to experimental results

The behaviour of the flow about the RSX has been modelled computationally using the AutoCAD file produced to print the three dimensional model for the experimental analysis. Thus, it can be assumed that the physical and computational models are identical, barring any discrepancies in the resin coating of the physical model.

As previously mentioned, the pressure and lift were unable to be determined experimentally, and therefore were unable to be compared with values determined computationally.

The first speed tested was selected to be equivalent to the experimental flow speed tested of 20.9 ms^{-1}. The equivalent speed in OpenFOAM was calculated so as to be dynamically similar to the experimental flow speed. From chapter 4.1.2, it is known that:

$$V_{air} = 14.85 V_{water}$$

Table 17: Equivalent velocities for computational, experimental and physical flows.

OpenFOAM- computational speed (ms^{-1})	**RSX- equivalent speed (ms^{-1})**	**Experimental flow speed (ms^{-1})**
1.43	1.43	20.9

Thus, the results determined in the wind tunnel at 20.9 ms^{-1} must be equivalent to a computational analysis conducted at 1.43 ms^{-1}. These results have been included below.

The angles of attack which were analysed computationally mimicked those tested experimentally. It should be noted that, for the sake of efficiency, the angle of

attack was changed by changing the direction of the incoming fluid, rather than the angle of the foil itself. An effect of this is that the water appears to travel through the tunnel walls, although there is no other impact on flow behaviour.

The earliest angle tested computationally was 8^{o}, and for this angle of attack, the flow was *not* attached across the entirety of the fin surface. It was attached across y-displacements bravo, charlie and echo, but not hotel. This early separation at cross section hotel suggests a fault in the leading edge radius used to model this cross section, in accordance with the results from Martellotta (2010). An example of the attached flow has been included below, for cross section charlie.

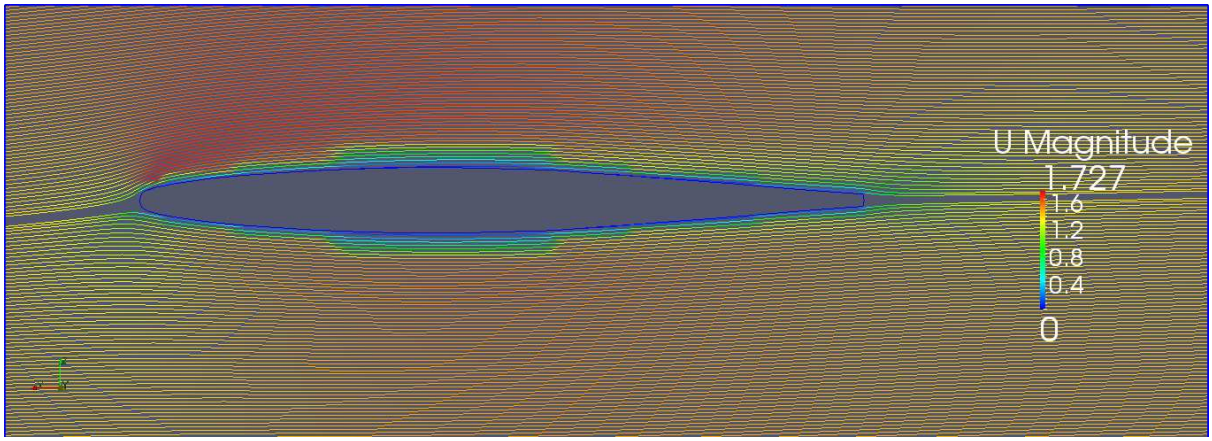

Figure 47: Streamlines showing attached flow about cross section charlie for a fin modelled at 8^{o} in water flowing at 1.42 ms^{-1}.

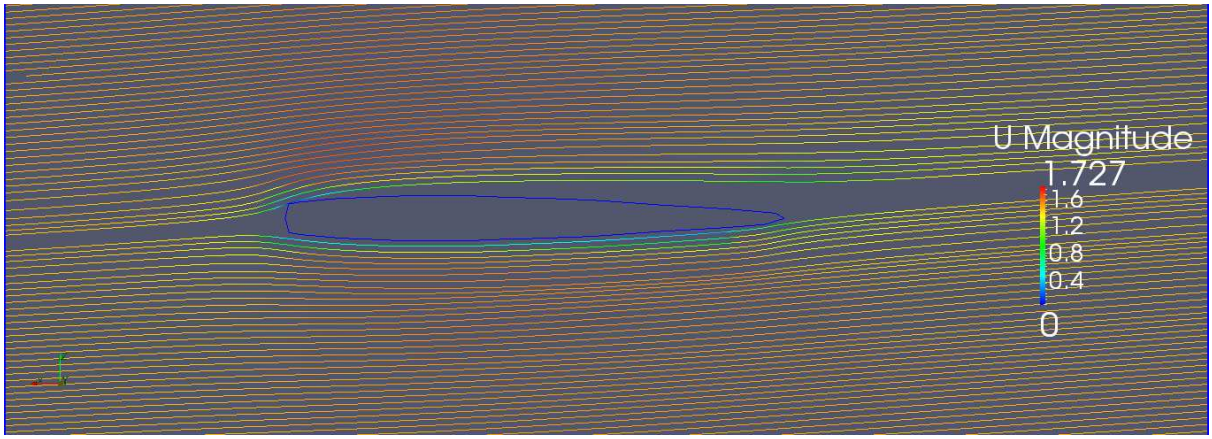

Figure 48: Streamlines showing leading edge separation at cross section hotel for a fin modelled at 8^{o} in water flowing at 1.42 ms^{-1}.

From the experimental analysis, the flow was completely attached at 8^{o}, which reinforces the idea that there might be an error in the leading edge of hotel in the computational model. Excepting y-displacement hotel, the experimental and computational results are in agreement for the angle of attack of 8^{o}.

When the angle of attack is increased to 10^{o}, separation just prior to the trailing edge is visible on cross section echo.

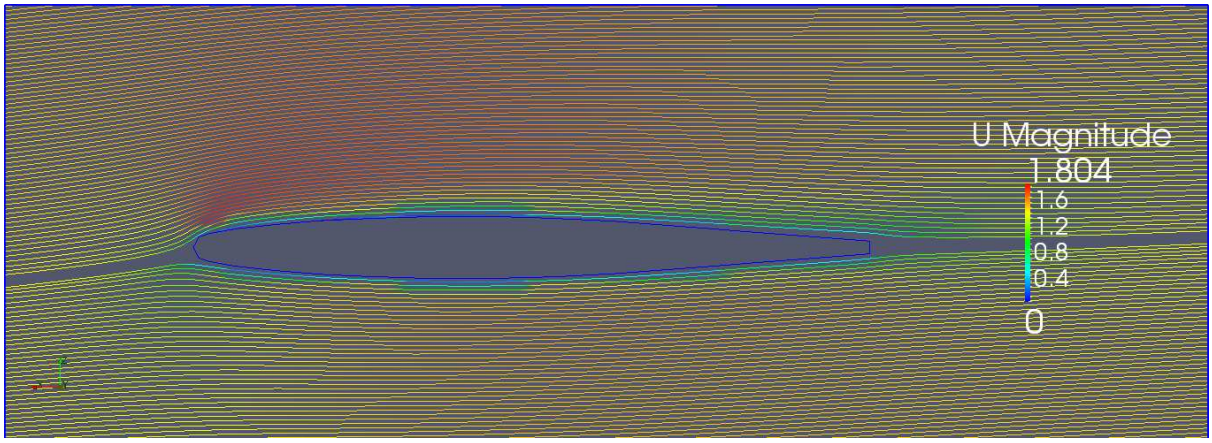

Figure 49: Streamlines showing attached flow around cross section echo, with slight separation towards the trailing edge for at 10^{o} in water flowing at 1.42 ms^{-1}.

The flow across cross sections bravo, charlie and echo remains attached, but the amount of leading edge separation at y-displacement hotel has increased, as shown in the figure below.

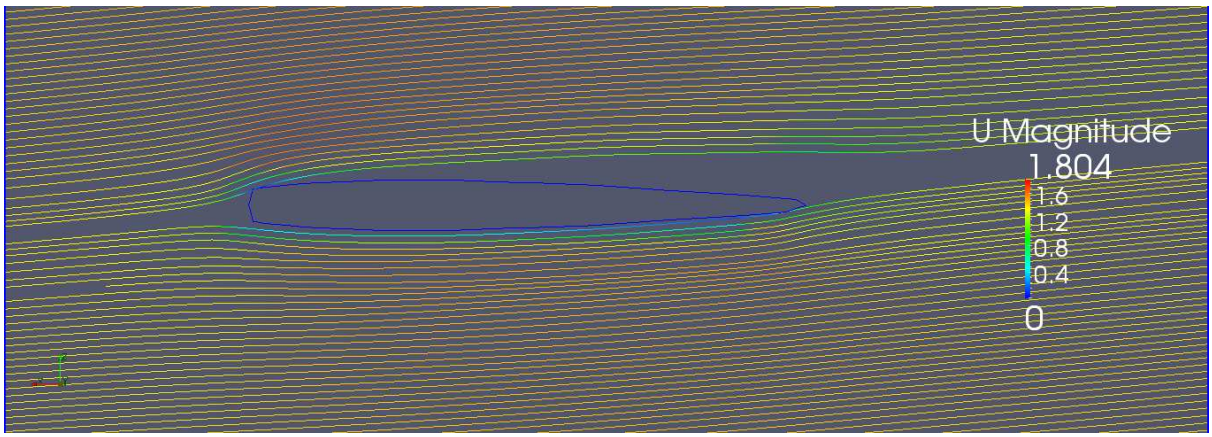

Figure 50: Streamlines showing leading edge separation at cross section hotel for a fin modelled at 10^{o} in water flowing at 1.42 ms^{-1}.

This does not agree with the experimental results, which show separation at 10-50% of the chord length for cross sections bravo and charlie, in addition to the trailing edge of cross section echo, which is shown.

As with the flow at 10^{o} with respect to the foil, the flow at a 12^{o} angle of attack, is attached across y-displacements bravo and charlie, and attached across most of y-displacement echo, with only slight separation occurring near the trailing edge.

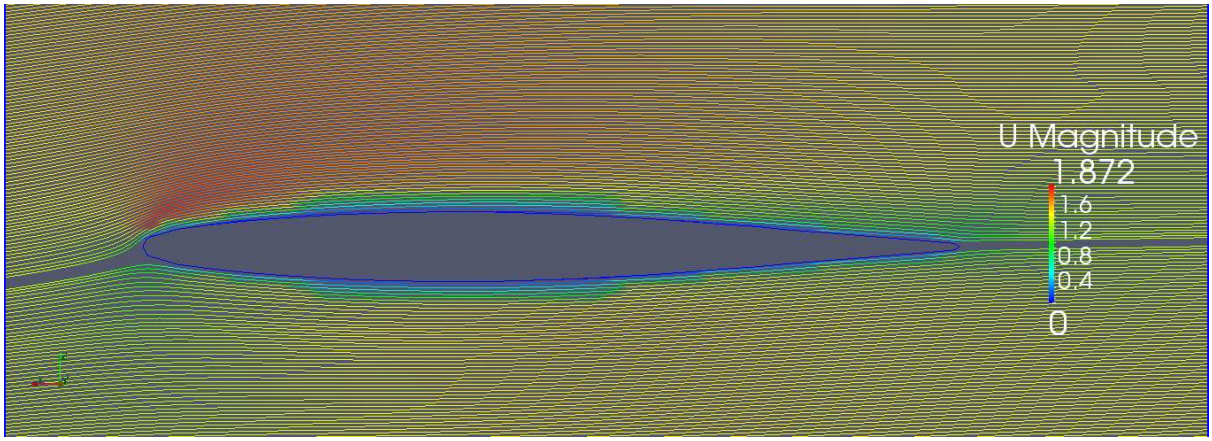

Figure 51: Streamlines showing attached flow around cross section bravo, at a 12^{o} angle of attack in water flowing at 1.42 ms^{-1}.

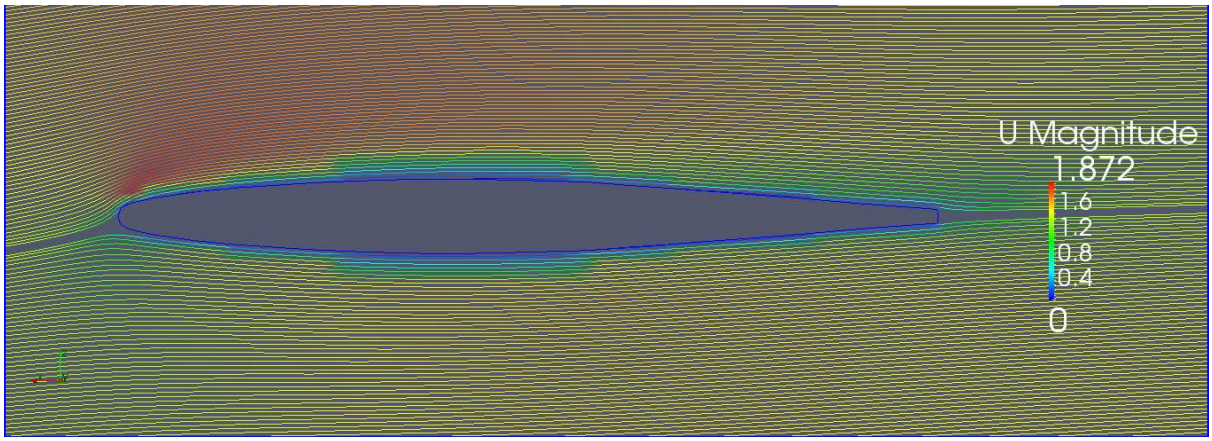

Figure 52: Streamlines showing attached flow around cross section charlie, at a 12^{o} angle of attack in water flowing at 1.42 ms^{-1}.

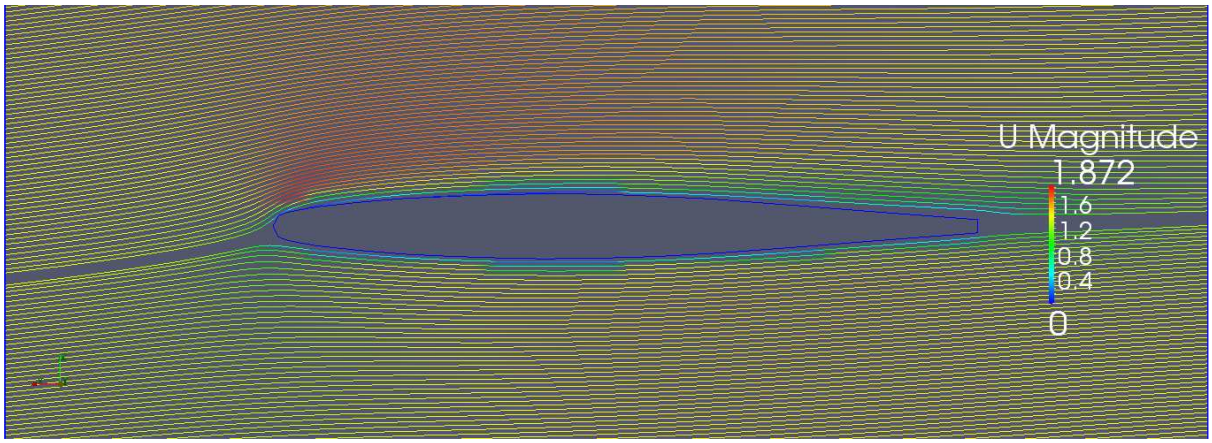

Figure 53: Streamlines showing attached flow around cross section echo, with slight separation towards the trailing edge at 12^{o} in water flowing at 1.42 ms^{-1}.

As with the 10^{o} angle of attack, the experimentally observed separation at the leading edge of cross sections bravo and charlie is not present in the computational analysis of 12^{o}. The separation observed towards the trailing edge of echo concurs with the experimental results, and the separation at hotel is more significant than the separation at the trailing edge of y-displacement golf.

When the angle of attack of the flow relative to the fin is increased to 14°, the flow remains attached around cross sections bravo, and charlie, only shows slight separation from the just prior to the trailing edge of echo, and remains fully separated from the leading edge of cross section hotel.

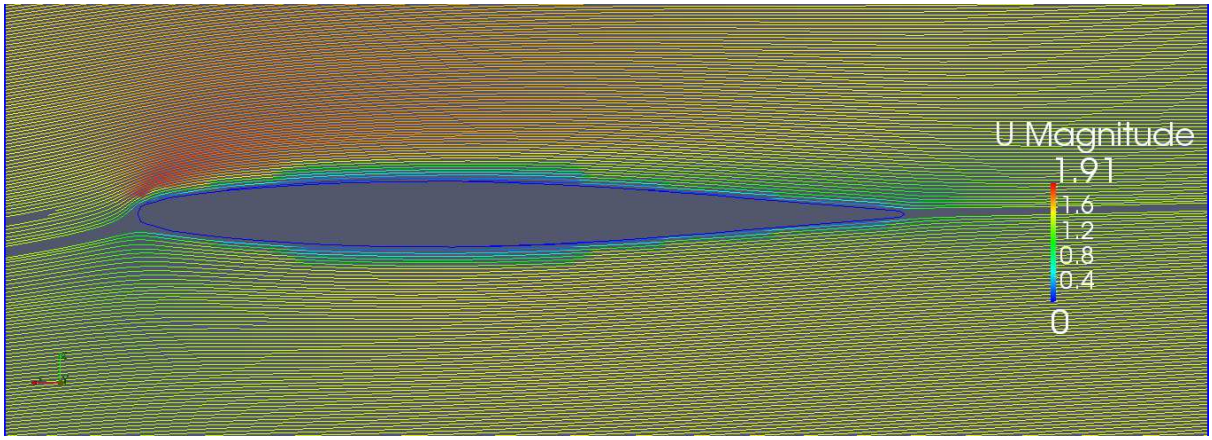

Figure 54: Streamlines showing flow around cross section bravo, at a 14° angle of attack in water flowing at 1.42 ms^{-1}.

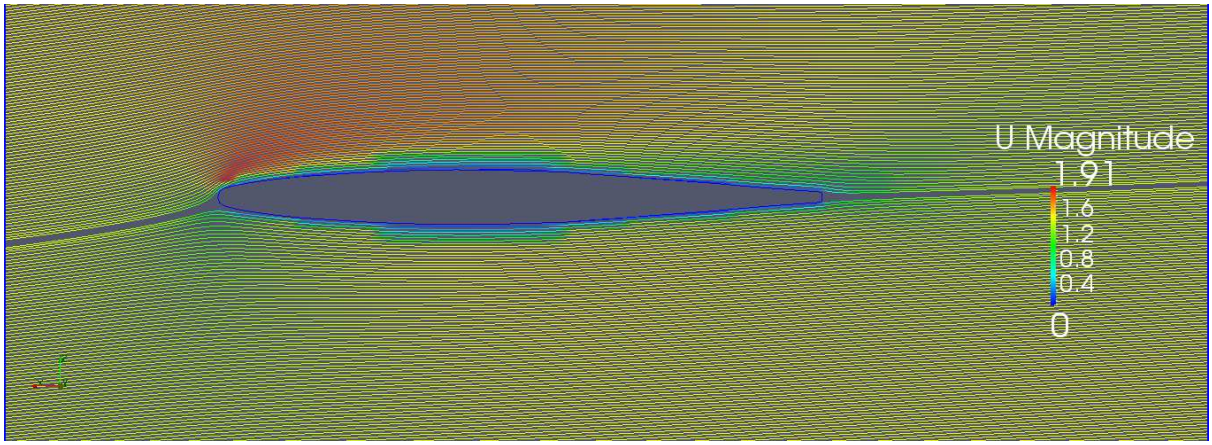

Figure 55: Streamlines showing flow around cross section charlie, at a 14° angle of attack in water flowing at 1.42 ms^{-1}.

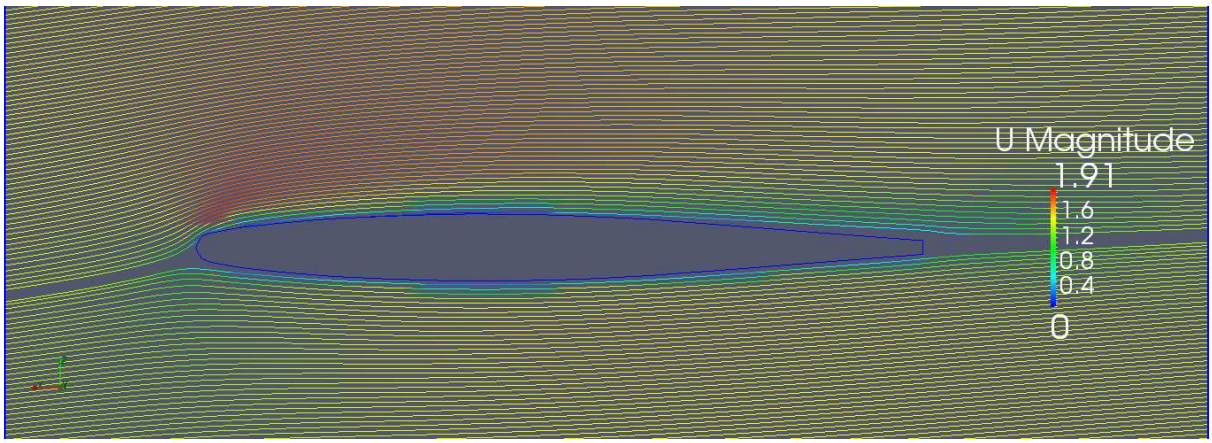

Figure 56: Streamlines showing flow around cross section echo, with slight separation towards the trailing edge at 14° in water flowing at 1.42 ms^{-1}.

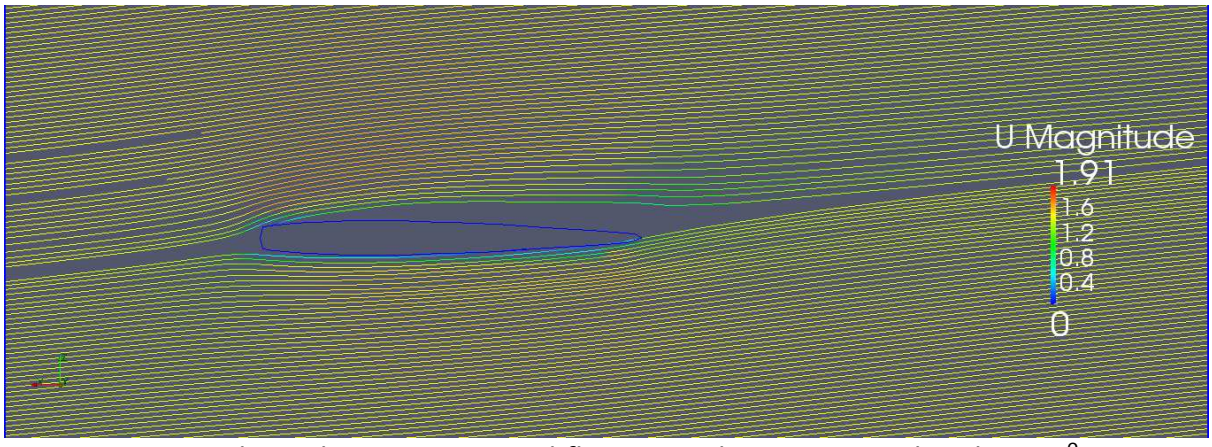

Figure 57: Streamlines showing separated flow around cross section hotel, at 14^{o} in water flowing at 1.42ms^{-1}.

The experimental analysis suggests that the flow should be separating at the leading edges of cross sections bravo and charlie, and again at 10-50% of the chord length of cross sections golf and echo.

There are two main points of contention between the experimental and computational analysis:

The first is the tendency of the flow to remain attached and attached around the foil surface for several degrees after the experimental analysis suggests the flow should have separated, in particular with respect to the leading edge separation noted experimentally at y-displacements bravo and charlie. This suggests a disparity in the conditions set for the turbulence model used to model the flow behaviour, or with the choice of model itself. However, since the Spalart-Allmaras model is typically used with success for external flows involving aerofoils, it is more likely that this error exists in the choice of conditions used to model the fluid turbulence.

The second point of contention is the continual and early leading edge separation at cross section hotel. This is likely caused a leading edge radius which results in a leading edge corner which is too sharp to be successfully navigated by the flow, even at low angles of attack. This corner was likely 'softened' on the physical model by the application of resin, and this has hence caused the disparity.

5.3.2 Computational results for racing speed applications

The behaviour of flow around the foil was analysed used OpenFOAM at 5, 10 and 15ms^{-1}. For each flow speed tested, the angle of attack of the foil relative to the fluid was increased from 10^{o} to 16^{o}, in increments of 2^{o}, and then again to 20^{o}.

For incoming flow at 5ms^{-1} and 10^{o}, the fluid remains attached to the foil along the upper cross sections bravo and charlie, but detaches at cross sections echo and hotel. The flow about cross-section hotel shows separation from the leading edge, whilst the flow about cross-section echo is primarily attached to the foil, but separates towards the trailing edge.

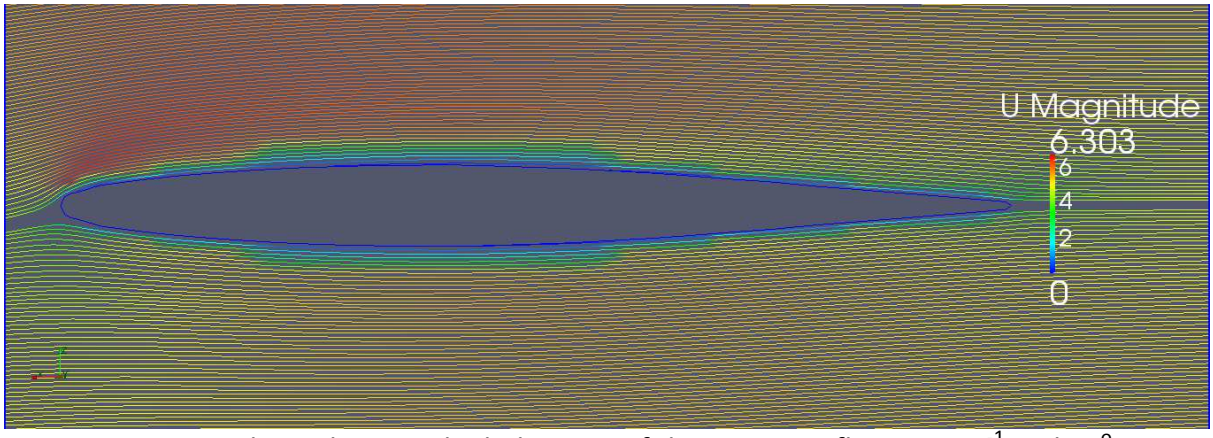

Figure 58: Streamlines showing the behaviour of the incoming flow at 5ms^{-1} and 10^{o} to the fin, across cross-section bravo.

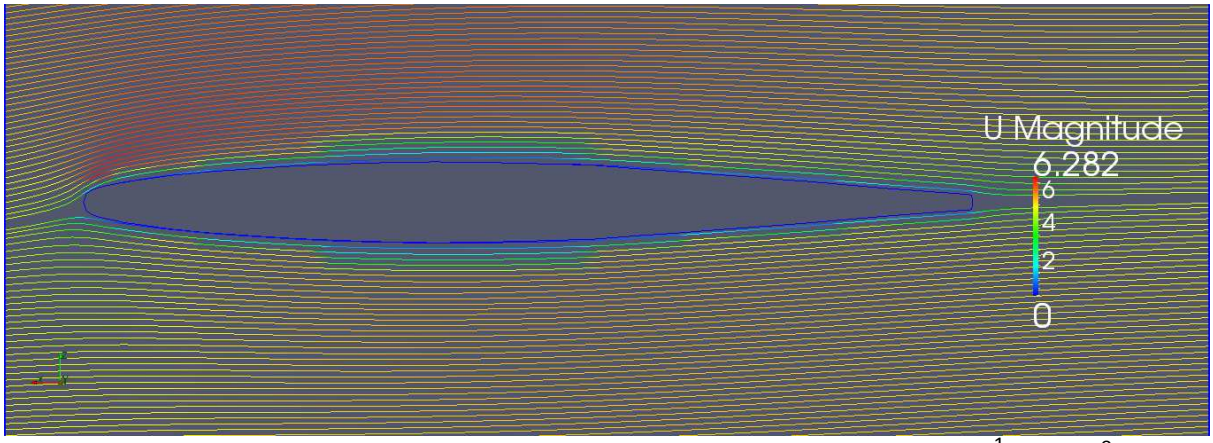

Figure 59: Streamlines showing the behaviour of the incoming flow at 5ms^{-1} and 10^{o} to the fin, across cross-section charlie.

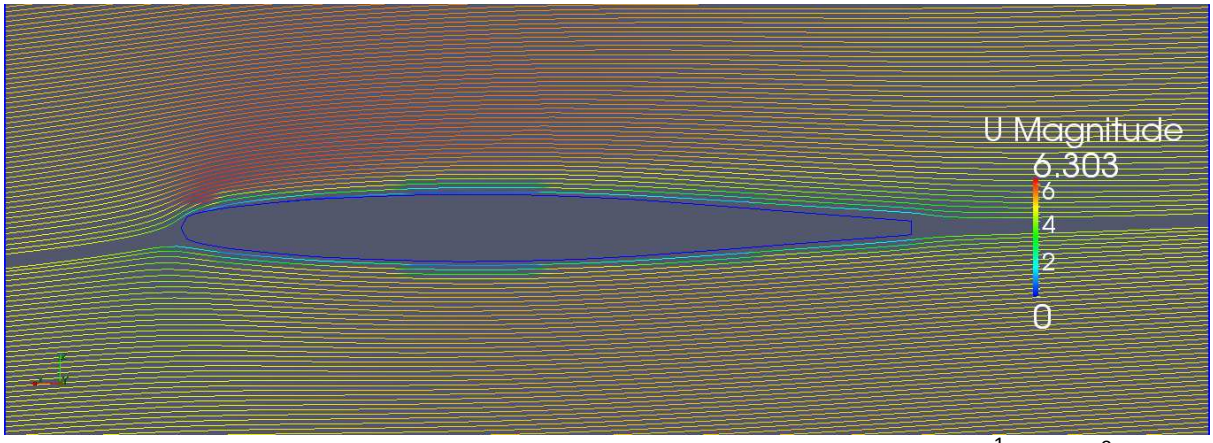

Figure 60: Streamlines showing the behaviour of the incoming flow at $5ms^{-1}$ and 10^{o} to the fin, across cross-section echo.

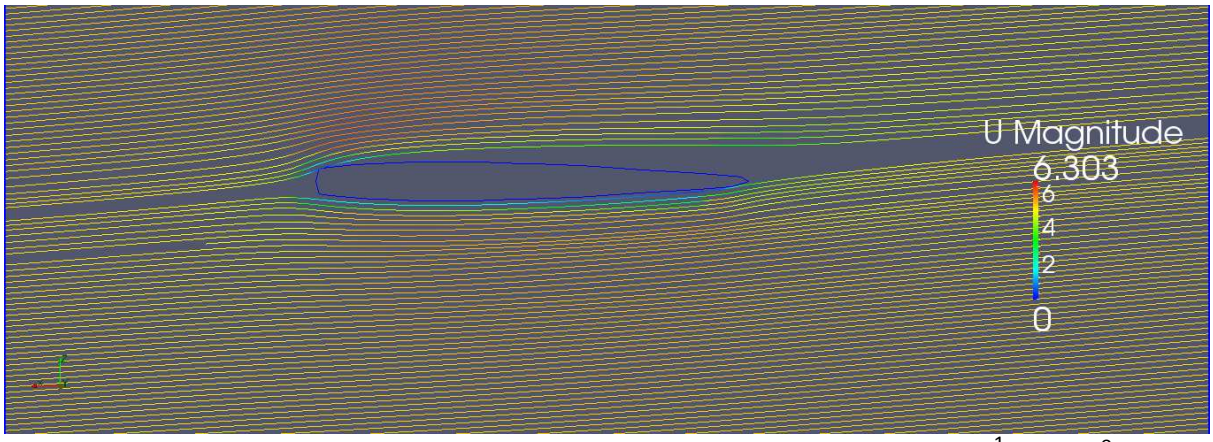

Figure 61: Streamlines showing the behaviour of the incoming flow at $5ms^{-1}$ and 10^{o} to the fin, across cross-section hotel.

The early leading edge separation at y-displacement hotel suggests that the leading edge is too sharp for the fluid to be able to successfully navigate the corner. This is confirmed by the presence of leading edge separation for flow at $5ms^{-1}$ and 5^{o}, shown below.

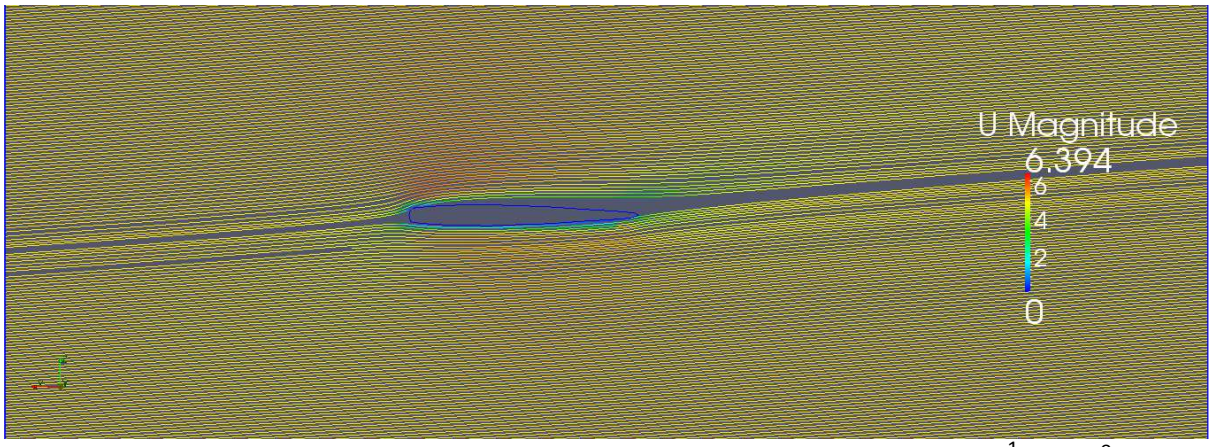

Figure 62: Streamlines showing the behaviour of the incoming flow at $5ms^{-1}$ and 5^{o} to the fin, across cross-section hotel.

This suggests that the calculation of the leading edge radius for this cross-section is not as accurate as previously thought.

This trailing edge separation along cross section echo becomes more defined as the angle of attack between the incoming fluid and the fin is increased.

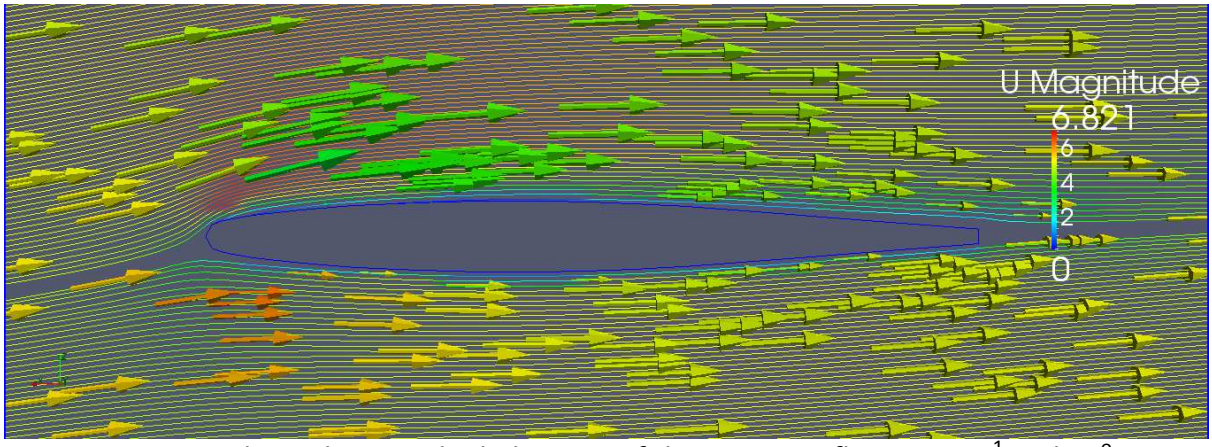

Figure 63: Streamlines showing the behaviour of the incoming flow at $5ms^{-1}$ and 16^{o} to the fin, across cross-section echo, with glyphs (arrows) showing pressure.

At an angle of attack of 20^{o}, the flow remains attached for the entirety of the fin surface, but does not model correctly around the leading edge, as shown below.

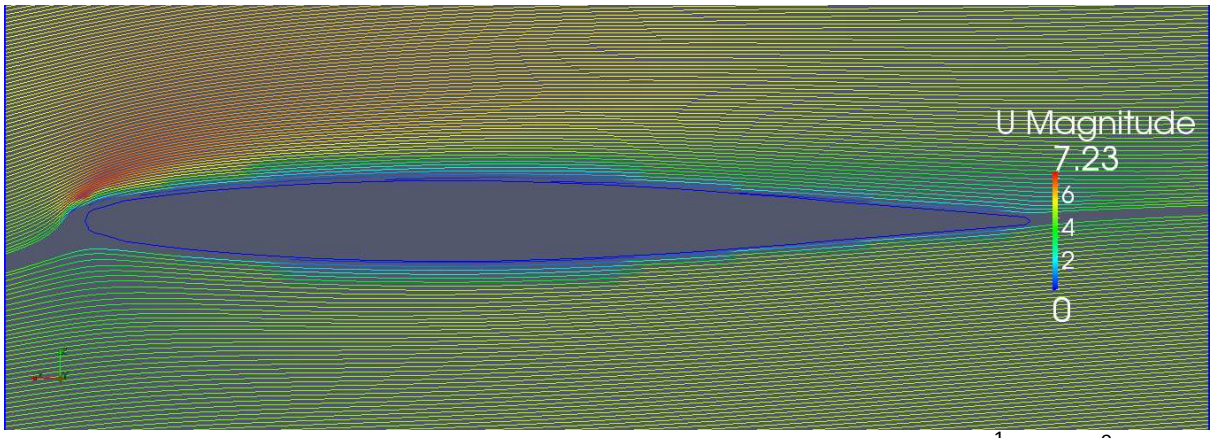

Figure 64: Streamlines showing the behaviour of the incoming flow at $5ms^{-1}$ and 20^{o} to the fin, across cross-section bravo

The angle of attack was then reset to 10^{o}, and the flow velocity increased to $10ms^{-1}$. As with the incoming flow of $5ms^{-1}$, the flow remains attached across y-displacements bravo and charlie, before then separating towards the trailing edge of echo, and completely from the leading edge of hotel.

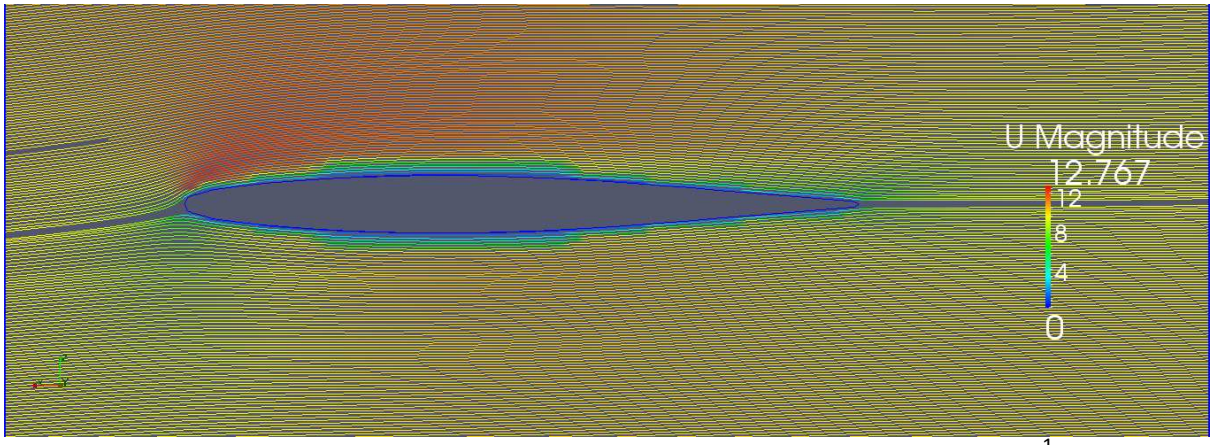

Figure 65: Streamlines showing the behaviour of the incoming flow at $10ms^{-1}$ and 10^{o} to the fin, across cross-section bravo

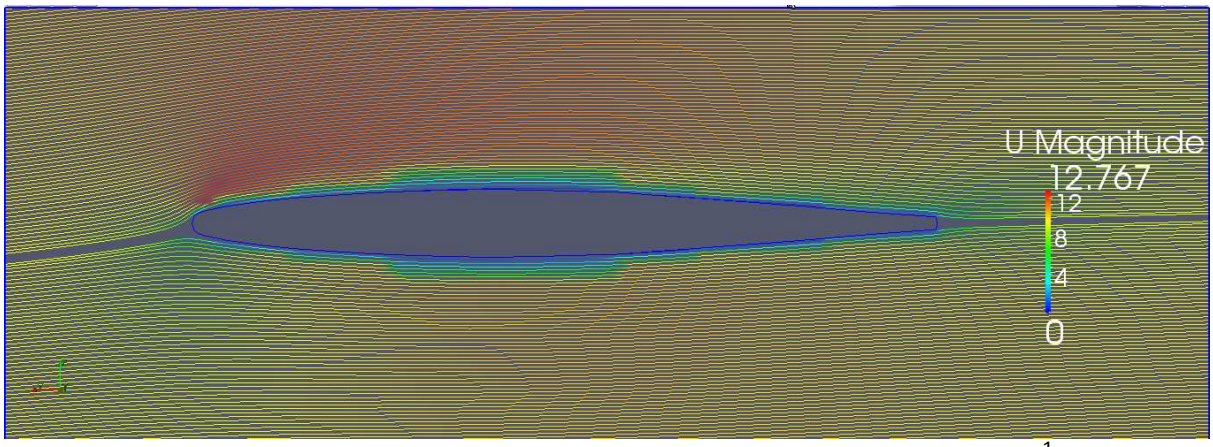

Figure 66: Streamlines showing the behaviour of the incoming flow at $10ms^{-1}$ and 10^{o} to the fin, across cross-section charlie

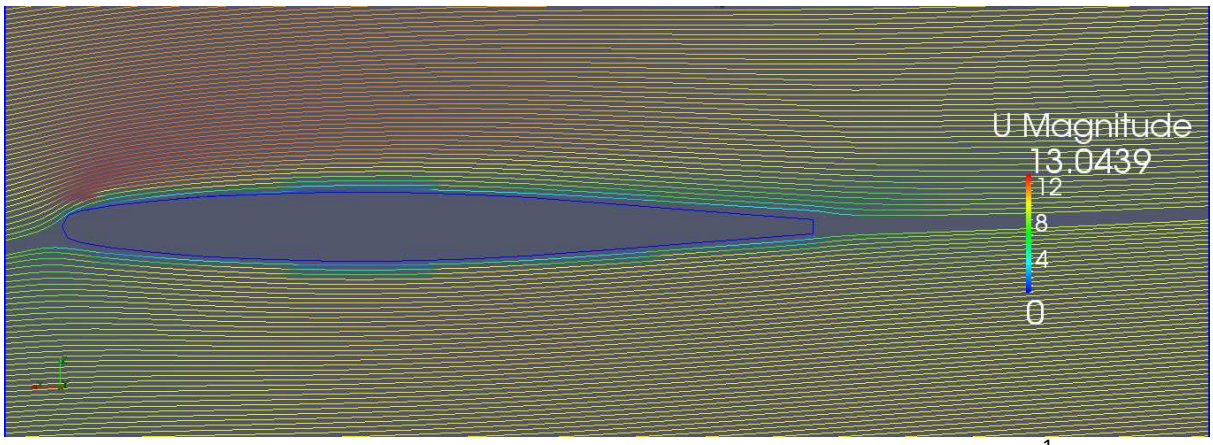

Figure 67: Streamlines showing the behaviour of the incoming flow at $10ms^{-1}$ and 10^{o} to the fin, across cross-section echo

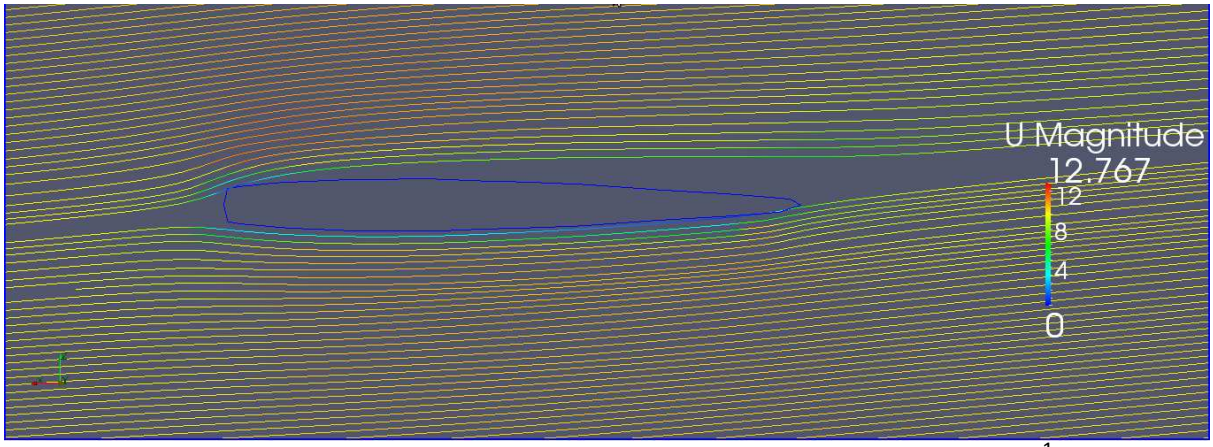

Figure 68: Streamlines showing the behaviour of the incoming flow at $10ms^{-1}$ and 10^{o} to the fin, across cross-section hotel

The separation at cross-sections echo and hotel becomes more significant as the angle of attack increases. At 20^{o}, the fluid is again mis-modelled at the leading edge of the fin, although it reattaches just after.

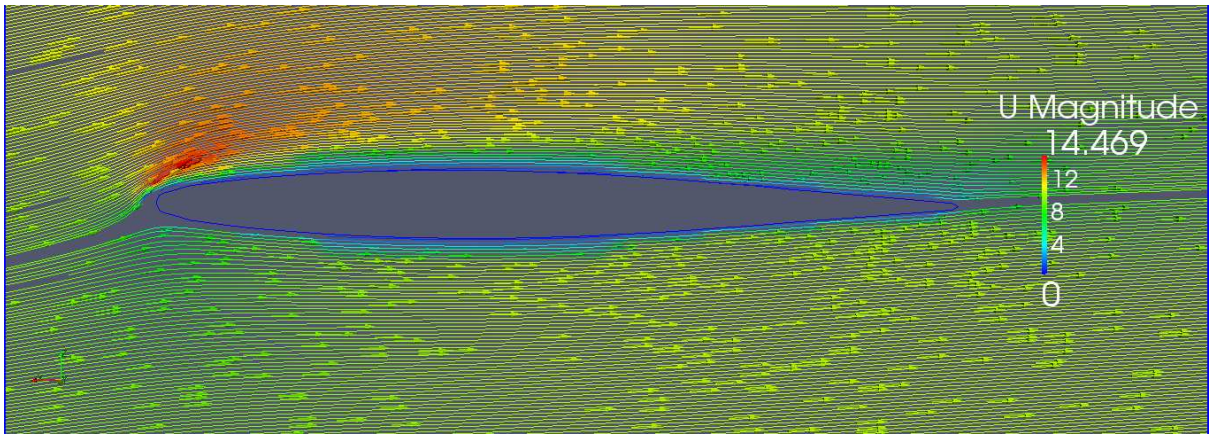

Figure 69: Streamlines showing a region of separation at the leading edge of cross section bravo for the incoming flow at $10ms^{-1}$ and 20^{o} with respect to the fin.

Increasing the fluid speed to $15ms^{-1}$ and again resetting the angle of attack to 10^{o}, gives similar results. The flow is attached across y-displacements bravo and charlie, and separates from the leading edge at cross section hotel. The flow has not yet separated at y-displacement echo.

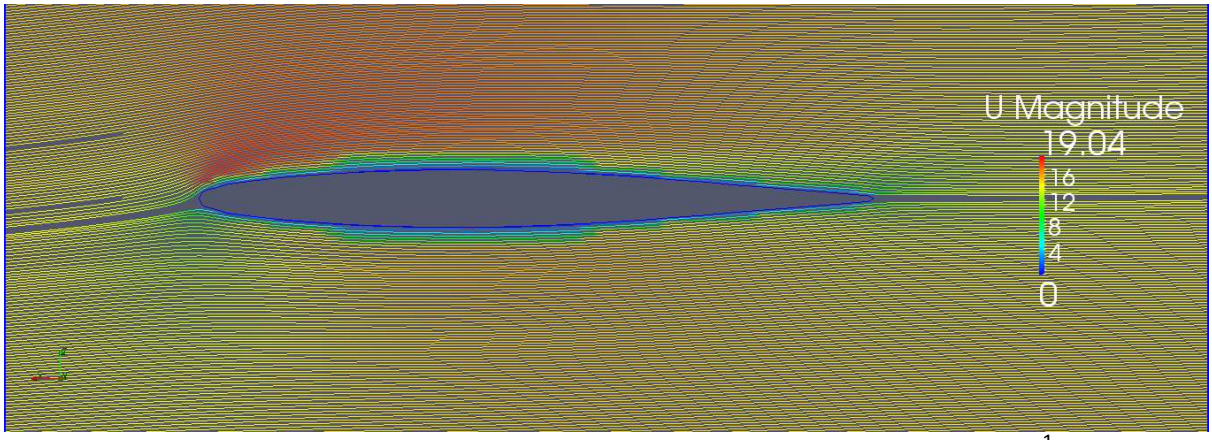

Figure 70: Streamlines showing the behaviour of the incoming flow at 15ms^{-1} and 10^{o} to the fin, across cross-section bravo

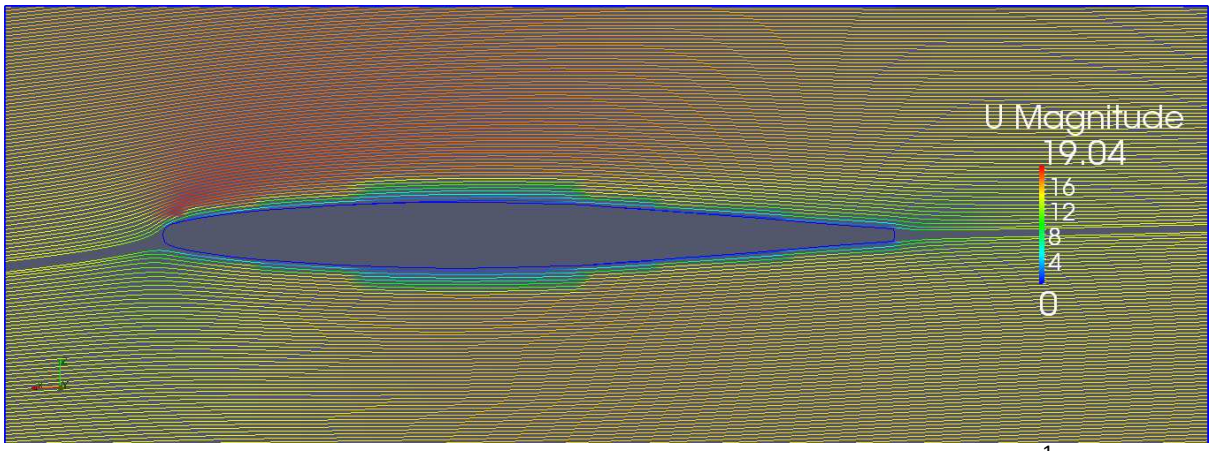

Figure 71: Streamlines showing the behaviour of the incoming flow at 15ms^{-1} and 10^{o} to the fin, across cross-section charlie

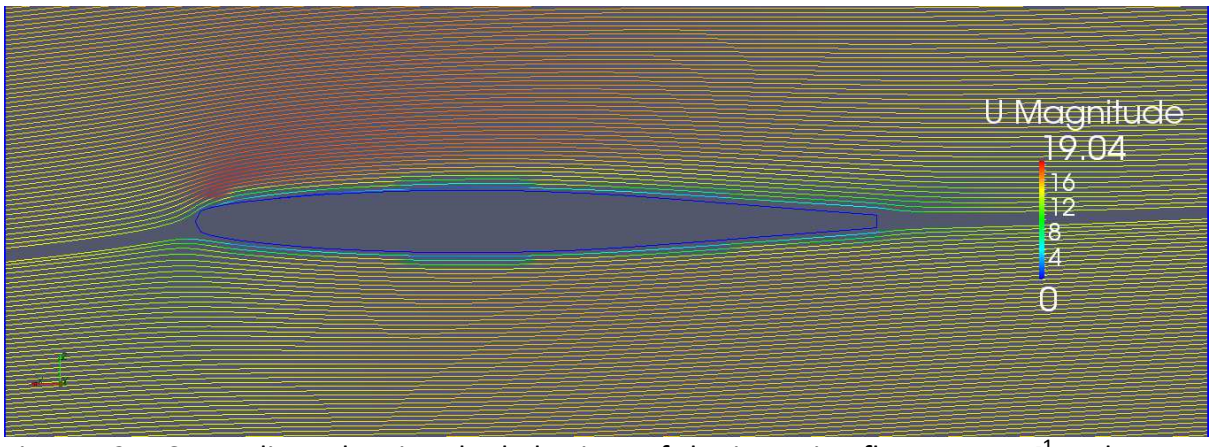

Figure 72: Streamlines showing the behaviour of the incoming flow at 15ms^{-1} and 10^{o} to the fin, across cross-section echo

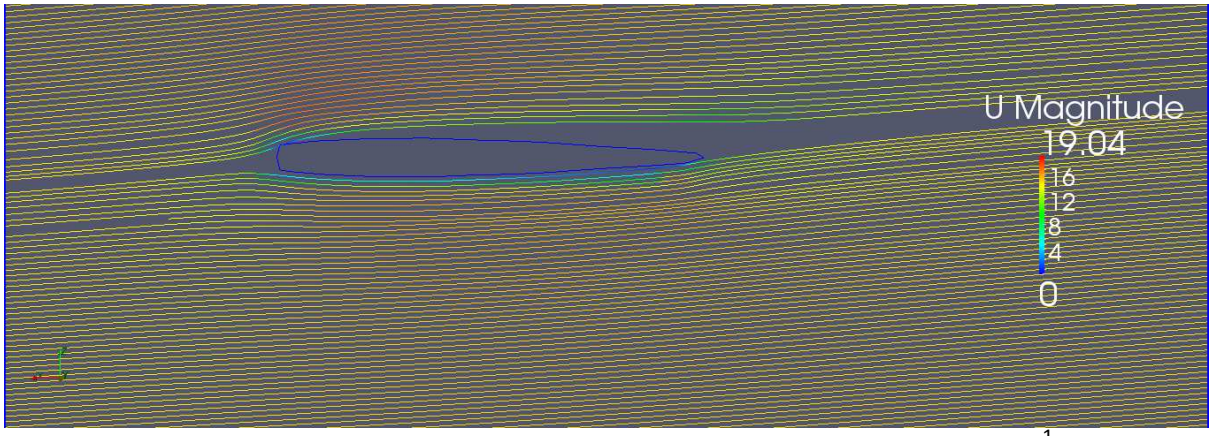

Figure 73: Streamlines showing the behaviour of the incoming flow at 15ms^{-1} and 10^{o} to the fin, across cross-section hotel

The flow separates from y-displacement echo at 20^{o}, but at this angle, the flow has not yet separated from the leading edge of y-displacement echo.

In all cases, it was expected that the flow would separate at an earlier angle of attack, based on the experimental results. This suggests that the settings/variables used with the turbulence model do not approximate the real conditions as well as had been hoped.

It was expected that the overall flow pattern would be influenced by the movement of fluid around the tips of the fin. Movement over the top of the fin (above the root) is prevented by the bottom of the RS:X windsurfing board. Since the movement around the fin tip is unrestricted, a degree of circulation occurs in the direction of the span of the fin. This influences flow behaviour along the span of the fin. (White 2008; Craig 2004; Crawford 2009; PilotFriend 2010)

This occurs since the pressure is higher on the upstream side of the fin than on the downstream side of the fin, as is expected from flow theory. In a three dimensional situation, where the wing has a finite length, air flows around the tip of the fin from the region of high pressure into the region of low pressure.

This flow around the tip of the foil causes a circular motion which is then swept off the trailing edge of the fin and continues to rotate, creating what are known as trailing edge or tip vortices. (White 2008; Craig 2004; Crawford 2009; PilotFriend 2010)

The flow from high to low pressure is evidenced about the trailing edge of the foil, as, for a set of streamlines passing through a single cross section, the flow streamlines of the downstream side of the foil is drawn upwards towards the root, and the streamlines on the upstream side.

This is shown in the figure below, with the close side shown as the upstream side.

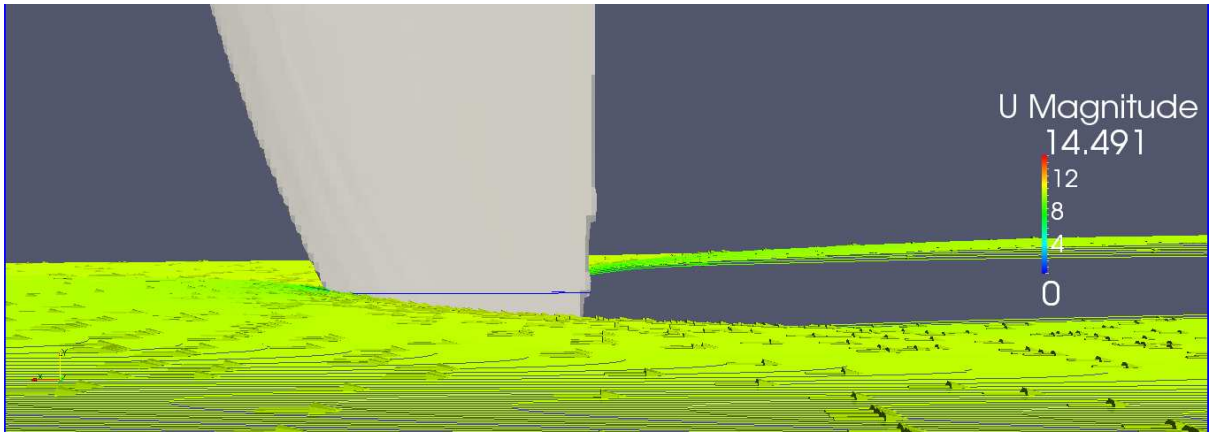

Figure 74: The flow streamlines are affected by the finite length of foil, causing cross flow.

Likewise, the vortices are only formed off the tip of the foil. The cross section shown is 5mm above the absolute tip of the fin, and it can be seen how the flow rotates underneath itself as it peels off of the trailing edge of the tip, causing a vortex to form.

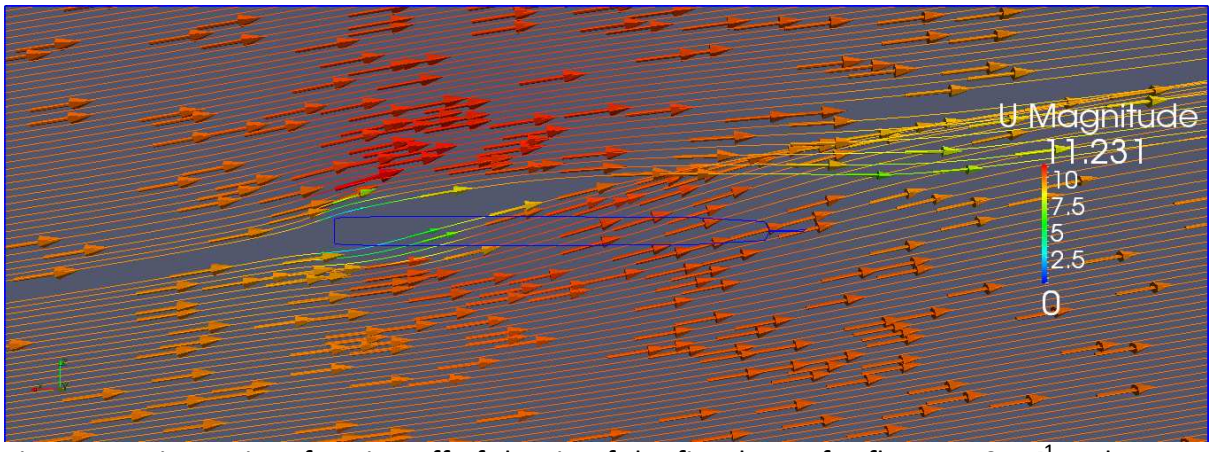

Figure 75: Tip vortices forming off of the tip of the fin, shown for flow at $10ms^{-1}$ and 20^{o}.

5.3.3 Conclusions based on computational results

OpenFOAM was used to determine the pressure and velocity everywhere within the specified flow field, but it is known separation is difficult to model accurately, since so many factors are involved, and the computationally modelled flow behaviour can be very sensitive to the choice of turbulence model. (Sodja 2007)

Since the computational and experimental results differ so greatly, it is likely that the process used to model the flow around the fin is flawed. Since the flow angle and direction are otherwise correct, and that the main disparity occurs with the location and angle of attack at which stall occurs, it is likely that this error arises from a flaw in the modelling of the turbulence which exists inside the wind tunnel.

The leading edge of the foil is not modelled with sufficient accuracy at cross section hotel to prevent persistent leading edge separation. This suggests that the accuracy with which the leading edge radius is modelled contributes greatly to the overall success of a computational analysis of flow around a foil, in agreement with Martellotta (2010).

6. Comparison of results to results expected for a NACA 65-009

The experimental data for a NACA 65-009 was determined experimentally by Abbott and Von Doenhoff (1959, 607). This shows that the lift coefficient is fairly consistent for an angle of attack of 0-12^0, before rapidly dropping by 14^o, for a foil of standard roughness.

These wing section characteristics were determined using a two dimensional low turbulence tunnel, and therefore the effects of finite length have not been taken into account. The tests were conducted at Reynolds numbers ranging from 3 x10^6 to 9x10^6, and for Mach numbers below 0.17. (Abbott and von Doenhoff 1959) The parameters used for the testing of the RS:X men's fin discussed in this report are suitable for comparison, as the Mach number tested is within this range, and the Reynolds numbers had the same order of magnitude, although they were just below the bottom limit for the Reynolds numbers tested.

Experimentally, it was noted that separation, and thus a loss of lift, occurred between 10^o and 16^o. This wider range of angles over which separation occurs, prevent the onset of stall being almost immediate, as would occur for a 65-009. This would be a desirable trait for a windsurfing fin, and is thus a reasonable result.

Computationally, the separation did not begin to occur until 20^o, which is substantially different to both the results determined experimentally, and the known results for a NACA 65-009. This supports the theory that the parameters used for the turbulence model are not suitable.

7. Conclusion

At the time of writing this report, the following conclusions can be drawn:

- The NACA section which the RS: X Racing 66 windsurfing fin bears the closest resemblance to, is the NACA 65-009.

- Flow separation starts at the 'root' of the foil, and progresses along the length of the fin as the angle of attack is increased, or alternatively, flow separation can occur the root and tip of the foil, and then progress inwards towards the centre of the fin. (Experimental conclusion)

- The rounded leading edge radius of the fin causes flow separation to begin at the trailing edge and then move forwards across the fin surface, towards the leading edge. (Experimental conclusion)

- The fin begins to exhibit signs of separation at approximately 10^{o}, and is fully stalled by 16^{o}. (Experimental conclusion)

- A significant level of cross flow exists on the downstream surface, which is directed away from the tip, and towards the root. (Computational conclusion)

- The turbulence model has a significant impact on the ability of a computational analysis to mimic the results of the experimental analysis. It is likely that the turbulence conditions used are the cause of the disparity between the computational and experimental results.

- The accuracy with which the leading edge radius is modelled contributes greatly to the overall success of a computational analysis of flow around a foil. This finding is in agreement with the postulate of Martellotta (2010).

8. Future Work

Future work to be completed on this project includes:

- Cross-analysing the results of the computational and experimental models, and comparing these results with those expected for a NACA 65-009 foil

- Improve the turbulence model to increase the correlation between the experimental and computational results

- Perform additional experimental testing with a wind tunnel capable of a greater range of velocities

- Perform experimental testing in an aquatic environment, or in a wind tunnel with the addition of a smoke machine, to look for the presence and formation of tip vortices

- Perform experimental testing in an aquatic environment, and examine the effects of ventilation of fluid behaviour

9. Acknowledgements

I would like to thank the following people for their assistance with the programming and analysis associated with this report.

- Dr Tim Gourlay (supervisor)
- Dr Andrew King (supervisor)
- Dr Kim Klaka
- Dr Daniel Veen
- Eamonn Colley

10. Nomenclature

Camber

Half way between the upper and lower surfaces of the foil

Chord Length

Length of foil from the leading to trailing edge

Leading edge

Front or nose of the foil

Thickness

Width of the foil at any given point

Trailing edge

Back edge (tail) of the foil

11. References

Abbott, I. H., and A. E. von Doenhoff. 1959. *Theory of wing sections, including a summary of airfoil data*. New York: Dover Publications. Original edition, 1949.

AutoCAD. 2009. *AutoCAD 2010 User Documentation*. http://docs.autodesk.com/ACD/2010/ENU/AutoCAD (accessed April 4th).

Bakker, A. 2005. *Turbulence models*. www.bakker.org/dartmouth06/engs150/10-rans.ppt (accessed October 7).

Bernoulli's Equation. 1997. http://www.princeton.edu/~asmits/Bicycle_web/Bernoulli.html (accessed September 9).

Burgess, F. H. 1974. *A dictionary for yachtsmen*. Newton Abbot, England: David & Charles.

Craig, G. 2004. *Circulation, lift and drag.* http://regenpress.com/circlatn.htm (accessed October 7).

Crawford, B. 2009. *Three dimensional aerodynamics*. http://www.flightlab.net/Flightlab.net/Download_Course_Notes_files/3_Three-DimensionalA%232BA154.pdf (accessed October 7).

Creagh-Osborne, R., and P. A. G. Milne. 1973. *This is sailing : a complete course*. [Lymington]: Nautical.

CSIRO. 2009. *Computational Modelling*. http://www.cmis.csiro.au/cfd/ (accessed June 6th).

Engineering ToolBox. 2011. *Pitot tubes*. http://www.engineeringtoolbox.com/pitot-tubes-d_612.html (accessed September 9).

Engineers Edge. 2011. *STL CAD files for Rapid Prototyping*. http://engineersedge.com/stl_rapid_proto.htm (accessed April 19, 2011).

Formero. 2010. *Rapid prototyping*. http://www.arrk.com.au/browse.asp?ContainerID=rapid_prototyping (accessed May 16th).

Fox, R., A. McDonald, and P. Pritchard. 2004a. *Introduction to fluid mechanics*. 6th ed: John Wiley & Sons, Inc.

--------. 2004b. *Introduction to fluid mechanics.* John Wiley & Sons, Inc. CD-ROM.

Garrett, R. 1987. *The symmetry of sailing : the physics of sailing for yachtsmen*. London: Adlard Coles.

Gentry, A. 1981. *Proceedings of the Eleventh AIAA Symposium on the Aero/Hydronautics of Sailing*, *September 12, 1981: A Review of Modern Sail Theory*. Seattle, Washington. http://www.arvelgentry.com/techs/A%20Review%20of%20Modern%20Sail%20Theory.pdf (accessed January 24, 2011).

--------. 2006. The origins of lift. http://www.arvelgentry.com/techs/origins_of_lift.pdf.

Glenn Research Centre. 2008. *Navier-Stokes Equations*. http://www.grc.nasa.gov/WWW/k-12/airplane/nseqs.html (accessed June 6th).

--------. 2010a. *Lift from flow turning*. http://www.grc.nasa.gov/WWW/K-12/airplane/right2.html (accessed January 12).

--------. 2010b. *Lift of a rotating cylinder*. http://www.grc.nasa.gov/WWW/K-12/airplane/cyl.html (accessed January 12).

--------. 2010c. *Size effects on lift*. http://www.grc.nasa.gov/WWW/k-12/airplane/size.html (accessed September 7).

--------. 2010d. *Wing geometry definitions*. http://www.grc.nasa.gov/WWW/k-12/airplane/geom.html (accessed October 10).

Gourlay, T. P., and J. Martellotta. 2011. Aero-hydrodynamic analysis of an RS:X Olympic racing sailboard. *CMST report 2011-02*.

Hewitt, P. G. 1998. *Conceptual physics*. 8th ed. Reading, Mass.: Addison Wesley.

Javaherchi, Y. 2010. *Review of Spalart-Allmaras Turbulence Model and its Modifications*. Washington: University of Washington. http://courses.washington.edu/mengr543/reports/teymour-report.pdf (accessed October 7, 2011).

Kroo, I. 2007. *Applied Aerodynamics: A digital textbook*. Stanford: Desktop Aeronautics Inc. http://www.desktop.aero/appliedaero/preface/welcome.html (accessed March 21,2011).

Li, X. 2008. *Sail into the wind.* http://www.thepingway.com/newsletter/sail-into-the-wind.htm (accessed October 16).

Marchaj, C. 1979. *Aero-hydrodynamics of sailing.* New York: Dodd, Mead and Company.

Martellotta, J. 2010. Performance analysis of one design sailing dinghies through measurement of rig characteristics, Science and Engineering, Curtin University, Perth

Marzocca, P. 2004. *The NACA airfoil series*. http://people.clarkson.edu/~pmarzocc/AE429/The%20NACA%20airfoil%20series.pdf (accessed September 5).

Munson, B., D. Young, and T. Okiiski. 2006. *Fundamentals of fluid mechanics*. 5th ed. Ames: John Wiley & Sons, Inc.

NeilPryde Racing. 2011a. *RS:X Board*. http://racing.neilpryde.com/rs-x/board.html (accessed March 12th).

--------. 2011b. *RS:X Sail Overview*. http://racing.neilpryde.com/rs-x/overview.html (accessed March 12th).

OpenFOAM. 2011a. *Features of OpenFOAM*. http://www.openfoam.com/features/ (accessed January).

--------. 2011b. *ParaView*. http://www.openfoam.com/features/paraview.php#paraview (accessed January).

--------. 2011c. *Pre-processing Utilities*. http://www.openfoam.com/features/preprocessing.php#preProcessingUtilities (accessed January).

OpenFOAMWiki. 2009. *PotentialFoam*. http://openfoamwiki.net/index.php/PotentialFoam (accessed October 8).

Peter, H. n.d. *Lift: Why can airplanes fly?* http://www3.kis.uni-freiburg.de/~peter/teach/hydro/hydro05.pdf (accessed October 16).

PilotFriend. 2010. *Wing vortices*. http://www.pilotfriend.com/training/flight_training/aero/wng_vort.htm (accessed October 7).

Public Domain Aeronautical Software. 2010. *Tables of profiles*. http://pdas.com/profiles.html (accessed May 17).

Ramsden, R. 2009. *What is the RS:X?* http://www.rsxclass.com/home/about (accessed March 12th).

Rapid Pro. 2011a. *3D Zcorp printing*. http://rapidpro.com.au/index.php/prototyping/prototyping-processes/3d-zcorp-printing/ (accessed May 16th).

--------. 2011b. *Rapid Pro*. http://rapidpro.com.au/ (accessed May 16th).

Serway, R. A., and J. W. Jewett. 2004. *Physics for scientists and engineers, with modern physics*. 6th ed. Belmont, CA: Thomson-Brooks/Cole.

Sodja, J. 2007. Turbulence models in CFD, Department of Theoretical Physics, University of Ljubljana, Ljubljana. http://www-f1.ijs.si/~rudi/sola/Turbulence-models-in-CFD.pdf (accessed October 16, 2011).

White, F. M. 1999. *Fluid Mechanics*. 4th ed. New York: McGraw-Hill.

--------. 2008. *Fluid Mechanics*. 6th ed. New York: McGraw-Hill.

--------. 2011. *Fluid Mechanics*. 8th ed. New York: McGraw-Hill.

Whitton, A. 2011. *Introduction to AutoCAD*. http://www.we-r-here.com/cad/tutorials/level_1/1-1.htm (accessed May 11th).

Z Corporation. 2010. *ZPrinter Product Line*. http://www.zcorp.com/documents/932_9062-ZPrinterSpecSheet.pdf (accessed May 16th).

--------. 2011. *ZPrinter 450*. http://www.zcorp.com/en/Products/3D-Printers/ZPrinter-450/spage.aspx (accessed May 16th).

12. Bibliography

(Sources read but not cited)

Avila, M. 1992. Computational and experimental investigation of the aerodynamic characteristics of a windsurfing sail section, Department of Aeronautics and Astronautics, Naval Postgraduate School, Monterey

Brummer, M. 2010. A look at the finn under the water. http://www.finnclass.org/index.php?option=com_content&view=article&id=204%3Aa-look-at-the-finn-under-the-water&Itemid=220&catid=30%3Afeatures (accessed 2011).

Chiu, T. W., P. G. Kalaugher, and C. A. M. Broers. 1995. The application of the photogrammetry in the study of the effects of sail board fin flexibility

Proceedings of the institution of mechanical engineers, part C, mechanical engineering science. *Mechanical Engineering Publications* 209 (C6): 373 - 381.

Hewitt, P. G. 1998. *Conceptual physics*. 8th ed. Reading, Mass.: Addison Wesley.

Livanos, A. 2006. Computational fluid dynamics investigation of two surfboard fin configurations, Faculty of Engineering, University of Western Australia, Perth. http://members.iinet.com.au/~livanos/CFD_report/Report.doc (accessed 2011, March 17th).

Nitzberg, G. E., and S. M. Crandall. 1952. *A comparative examination of some measurements of airfoil section lift and drag at supercritical speeds*. Moffett Field: Ames Aeronautical Laboratory.2011, March 17th).

Partilda, L. P. 1986. Comparative computational analysis of airfoil sections for use on sailing craft. Masters diss., Department of Aeronautics and Astronautics, Naval Postgraduate School, Monterey (accessed February 23rd, 2011).

Swales, P. D., A. J. Wright, R. C. McGregor, and R. S. Rothblum. 1974. The mechanism of ventilation inception on surface piercing foils. *Journal of Mechanical Engineering Science* 16 (1): 8.

13. Appendix

13.1. Matlab Code

13.1.1 mysolvemissing.m

```
clear
close all

%created 14/4/2011, K. Hansen, to interpolate missing data

%read in excel data
myFile='I:\Honours\hons matlab\AlphaBravoInterpolate.xls';
data=xlsread([myFile]);

%label columns
alphaX=data(:,1);
alphaY=data(:,2);
alphaZ=data(:,3);
bravoX=data(:,4);
bravoY=data(:,5);
bravoZ=data(:,6);

%interpolate
alpha63=interp1(alphaX,alphaZ,63);
alpha68=interp1(alphaX,alphaZ,68);

bravo54=interp1(bravoX,bravoZ,54);
```

13.1.2 interpPoints.m

```
clear
close all

%created 14/4/2011, K.Hansen, to interp missing data

%% read in excel data
%myFile='I:\Honours\hons matlab\interpolateall.xls';
```

```
myFile='F:\Honours\hons matlab\interpolateall2.xls';
data=xlsread([myFile]);

%% label columns
%a
alphaX=data(:,1);
alphaY=data(:,2);
alphaZ=data(:,3);
%b
bravoX=data(1:33,4);
bravoY=data(1:33,5);
bravoZ=data(1:33,6);
%c
charlieX=data(1:30,7);
charlieY=data(1:30,8);
charlieZ=data(1:30,9);
%d
deltaX=data(1:28,10);
deltaY=data(1:28,11);
deltaZ=data(1:28,12);
%e
echoX=data(1:25,13);
echoY=data(1:25,14);
echoZ=data(1:25,15);
%f
foxtrotX=data(1:23,16);
foxtrotY=data(1:23,17);
foxtrotZ=data(1:23,18);
%g
golfX=data(1:22,19);
golfY=data(1:22,20);
golfZ=data(1:22,21);
%h
hotelX=data(1:9,22);
hotelY=data(1:9,23);
hotelZ=data(1:9,24);

%% interpolate
bravo107=interp1(bravoX,bravoZ,107);
bravo102=interp1(bravoX,bravoZ,102);
bmat=[107,bravo107;102,bravo102];

charlie88=interp1(charlieX,charlieZ,88);
charlie86=interp1(charlieX,charlieZ,86);
charlie83=interp1(charlieX,charlieZ,83);
charlie77=interp1(charlieX,charlieZ,77);
charlie3=interp1(charlieX,charlieZ,3);
```

```
cmat=[88,charlie88; 86,charlie86; 83,charlie83; 77,charlie77; 3,charlie3];

delta68=interp1(deltaX,deltaZ,68);
delta67=interp1(deltaX,deltaZ,67);
delta63=interp1(deltaX,deltaZ,63);
delta58=interp1(deltaX,deltaZ,58);
delta54=interp1(deltaX,deltaZ,54);
delta8=interp1(deltaX,deltaZ,8);
delta3=interp1(deltaX,deltaZ,4);
dmat=[68,delta68; 67, delta67; 63, delta63; 58, delta58; 54, delta54; 8, delta8;
3,delta3];

echo52=interp1(echoX,echoZ,52);
echo50=interp1(echoX,echoZ,50);
echo48=interp1(echoX,echoZ,48);
echo46=interp1(echoX,echoZ,46);
echo41=interp1(echoX,echoZ,41);
echo36=interp1(echoX,echoZ,36);
echo1=interp1(echoX,echoZ,1);
echo_3=interp1(echoX,echoZ,-3);
echo_9=interp1(echoX,echoZ,-9);
echo_12=interp1(echoX,echoZ,-12);
emat=[52, echo52; 50, echo50; 48, echo48; 46, echo46; 41, echo41; 36, echo36; 1,
echo1; -3, echo_3; -9, echo_9; -12, echo_12];

foxtrot33=interp1(foxtrotX,foxtrotZ,33);
foxtrot31=interp1(foxtrotX,foxtrotZ,31);
foxtrot28=interp1(foxtrotX,foxtrotZ,28);
foxtrot26=interp1(foxtrotX,foxtrotZ,26);
foxtrot23=interp1(foxtrotX,foxtrotZ,23);
foxtrot3=interp1(foxtrotX,foxtrotZ,3);
foxtrot_3=interp1(foxtrotX,foxtrotZ,-3);
foxtrot_8=interp1(foxtrotX,foxtrotZ,-8);
foxtrot_12=interp1(foxtrotX,foxtrotZ,-12);
foxtrot_18=interp1(foxtrotX,foxtrotZ,-18);
foxtrot_22=interp1(foxtrotX,foxtrotZ,-22);
foxtrot_28=interp1(foxtrotX,foxtrotZ,-28);
fmat=[33, foxtrot33; 31, foxtrot31; 28, foxtrot28; 26, foxtrot26; 23, foxtrot23; 3,
foxtrot3; -3, foxtrot_3; -8, foxtrot_8; -12, foxtrot_12; -18, foxtrot_18; -22,
foxtrot_22; -28, foxtrot_28];

golf23=interp1(golfX,golfZ,23);
golf21=interp1(golfX,golfZ,21);
golf18=interp1(golfX,golfZ,18);
golf16=interp1(golfX,golfZ,16);
golf14=interp1(golfX,golfZ,14);
golf12=interp1(golfX,golfZ,12);
```

```
golf8=interp1(golfX,golfZ,8);
golf6=interp1(golfX,golfZ,6);
golf_7=interp1(golfX,golfZ,-7);
golf_12=interp1(golfX,golfZ,-12);
golf_17=interp1(golfX,golfZ,-17);
golf_24=interp1(golfX,golfZ,-24);
golf_27=interp1(golfX,golfZ,-27);
gmat=[23, golf23; 21, golf21; 18,golf18; 16,golf16; 14,golf14; 12,golf12; 8,golf8;
6,golf6; -7,golf_7; -12,golf_12; -17,golf_17; -24,golf_24; -27,golf_27];

hotel3=interp1(hotelX,hotelZ,3);
hotel2=interp1(hotelX,hotelZ,2);
hotel1=interp1(hotelX,hotelZ,1);
hotel_1=interp1(hotelX,hotelZ,-1);
hotel_3=interp1(hotelX,hotelZ,-3);
hotel_4=interp1(hotelX,hotelZ,-4);
hotel_7=interp1(hotelX,hotelZ,-7);
hotel_9=interp1(hotelX,hotelZ,-9);
hotel_11=interp1(hotelX,hotelZ,-11);
hotel_13=interp1(hotelX,hotelZ,-13);
hotel_17=interp1(hotelX,hotelZ,-17);
hotel_19=interp1(hotelX,hotelZ,-19);
hotel_22=interp1(hotelX,hotelZ,-22);
hotel_24=interp1(hotelX,hotelZ,-24);
hotel_27=interp1(hotelX,hotelZ,-27);
hotel_29=interp1(hotelX,hotelZ,-29);
hotel_31=interp1(hotelX,hotelZ,-31);
hotel_32=interp1(hotelX,hotelZ,-32);
hmat=[3,hotel3; 2,hotel2; 1,hotel1;-1,hotel_1; -3,hotel_3; -4,hotel_4; -7,hotel_7; -
9,hotel_9;  -11,hotel_11; -13,hotel_13; -17,hotel_17;-19,hotel_19; -22,hotel_22; -
24,hotel_24; -27,hotel_27; -29,hotel_29;-31,hotel_31;-32,hotel_32];
```